Étude de la dissociation des hydrocarbures aromatiques polycycliques dans un contexte astrophysique

Sarah Rodriguez Castillo

To cite this version:

Sarah Rodriguez Castillo. Étude de la dissociation des hydrocarbures aromatiques polycycliques dans un contexte astrophysique. Astrophysique [astro-ph]. Université Toulouse 3 – Paul Sabatier, 2018. Français. NNT : . tel-02174638

HAL Id: tel-02174638
https://theses.hal.science/tel-02174638
Submitted on 5 Jul 2019

HAL is a multi-disciplinary open access archive for the deposit and dissemination of scientific research documents, whether they are published or not. The documents may come from teaching and research institutions in France or abroad, or from public or private research centers.

L'archive ouverte pluridisciplinaire **HAL**, est destinée au dépôt et à la diffusion de documents scientifiques de niveau recherche, publiés ou non, émanant des établissements d'enseignement et de recherche français ou étrangers, des laboratoires publics ou privés.

THÈSE

En vue de l’obtention du

DOCTORAT DE L’UNIVERSITÉ DE TOULOUSE

Délivré par l'Université Toulouse 3 - Paul Sabatier

Présentée et soutenue par

Sarah RODRIGUEZ CASTILLO

Le 30 octobre 2018

Etude de la dissociation des hydrocarbures aromatiques polycycliques dans un contexte astrophysique

Ecole doctorale : **SDU2E - Sciences de l'Univers, de l'Environnement et de l'Espace**

Spécialité : **Astrophysique, Sciences de l'Espace, Planétologie**

Unité de recherche :
IRAP - Institut de Recherche en Astrophysique et Planetologie

Thèse dirigée par
Christine JOBLIN et Aude SIMON

Jury
Mme Dahbia TALBI, Rapporteur
M. Thomas PINO, Rapporteur
Mme Emilie HABART, Examinateur
M. José Ángel MARTíN GAGO, Examinateur
M. Adam WALTERS, Examinateur
Mme Christine JOBLIN, Directeur de thèse
Mme Aude SIMON, Co-directeur de thèse

A mi madre y a mi aitite

Acknowledgements

The list of people that have contributed to this thesis one way or another is quite long, so please bear with me. First, and at the risk of sounding cliché, this thesis would have never existed without the help and motivation of Dr. Christine Joblin and Dr. Aude Simon. Their mentorship, enthusiasm and support have accompanied me throughout this journey, even from distance. In particular I must thank Christine for her rigor, her constant - almost motherly - guidance, for always being available (she should probably think about buying Skype stocks), and for pushing me when I needed it, which might have been more times than I would like to admit. And Aude, for her patience, her temper, and her clear explanations of the theoretical methods that made it possible for me to think that I understand quantum chemistry. Following, a special mention and thanks to the people of the école doctorale, in particular Dr. Geneviève Soucail for being so understanding. I would not like to continue without mentioning Prof. Paul Mayer and his family, who welcomed me more warmly than I could ask for. This experience helped me to grow in more ways than just professionally. Also, a special thanks to Brandi for all her help, clear explanations and much appreciated comments!

Following, I would also like to thank everyone involved in the experiments performed at SOLEIL. From the DESIRS team (Laurent Nahon and Alexandre Giuliani) to all the collaborators who shared so many sleepless hours with great humor, it was fun! This work was carried out within two different working groups that deserve all my respect. First, thanks to the team in LCPQ who, despite my absences, always made me feel welcome and integrated. In particular, thanks to Jérôme and Mathias for their kindness, to Fernand for his support and to Bastien for his chats. To all the members of MICMAC in IRAP, I express my warmest gratitude, in particular for tolerating my English-speaking-stubbornness and for making the Journal Club a small success. It was a pleasure to have worked in such a good environment. Marta, Paolo, Agnes, Loïc, Nick, Ludo, Olivier, Isabelle, Karine, Katia, Gabi, Pavol, each of you deserve an explicit mention, and at least a beer, for sparkling up my life in Toulouse. Speaking of sparkles, I will never forget the amazing cakes of Giacomo, to whom I profess my deepest affection and admiration (also as a baker).

Continuing with friends, I would like to dedicate a couple of lines to the ones that have always been there, and to the ones I have made over the years. Superstars, qué os voy a decir que no sepáis ya, que aunque nos hayamos movido más que una peonza seguís siendo uno de mis pilares sin el cual no estaría escribiendo esto. Gracias por star ahí incondicionalmente, y por todos los bodorrios y niños que han tenido lugar en estos 3 años! Pedro thanks for the happy-barris, the pictures of Kelvin, and in general for not giving up on our friendship through time and space. Christelle, Ευχαριστώ πολύ for your energy, your happiness and all your cool plans. Nasia, Benji, I also owe you part of my sanity, for sharing all the PhD experiences and stories, and for all the visits. Much love, such PhD. I would not like to forget everyone in ESA who has put up with me during the writing process. And speaking of tolerating me, I wouldn't be here if it wasn't for the constant, unconditional love and support from Nikos... 'Txikaipo' have a thesis now, let's go to Africa!

Last but obviously not least, my family. Their constant support and, why not, their 'you can do whatever you want in life'-pressure have taken me where I am which, ironically, is far away from them. No words can express how much you mean to me, I hope you are proud. Mom, I'm here thanks to everything that you have taught me. This thesis is for you (and for Brow because she is so cuuuute!)

To all of you, sincerely, thank you.

(And, of course, "I acknowledge support from the European Research Council under the European Union's Seventh Framework Programme ERC-2013-SyG, Grant Agreement n. 610256 NANOCOSMOS". Finally, all the comic strips are used with the permission of Jorge Chan, check out his website 'Piled Higher and Deeper', www.phdcomics.com)

Abstract

Polycyclic Aromatic Hydrocarbons (PAHs) are revealed in astrophysical environments thanks to their characteristic infrared emission after these molecules are subjected to the vacuum ultraviolet (VUV) radiation from nearby massive stars. This interaction regulates their charge state, stability and dissociation mechanisms, which in turn affect the energy balance and the chemistry of the gas in the interstellar medium. In particular, PAHs could contribute to the formation of the most abundant molecule, H_2, in photodissociation regions (PDRs). This work aims at contributing to these topics by quantifying the VUV photoprocessing of specific medium-sized PAH cations through experimental studies complemented by computational investigations.

The experimental results were gathered from two campaigns at synchrotron facilities. On the one hand, we performed action spectroscopy on a quadrupole ion trap under photon incidence in the 8-20 eV range at the DESIRS beamline in SOLEIL. The yields of ionization and fragmentation of several small- to medium-sized PAH cations (10-24 carbon atoms) were obtained, as well as the branching ratio between the different fragments. On the other hand, imaging PhotoElectron PhotoIon Coincidence (iPEPICO) experiments were carried out on several PAHs at the Swiss Light Source at photon energies of 15.5 to 22 eV. As a result, breakdown curves of PAHs energized by VUV photons were obtained. We benefited from the time information provided by this technique to derive dissociation rates by fitting experimental data with a statistical model based on Rice-Ramsperger-Kassel-Marcus (RRKM) theory.

For in-depth considerations on the fragmentation processes, we have focused our study on two isomers of dibenzopyrene cation ($C_{24}H_{14}^{+}$) in order to assess the impact of structure on these processes. In particular, emphasis is given on the competitive channels at low energies, namely the dehydrogenation processes (H, 2H/H_2 loss). Theoretical analyses are performed on the reaction energetics and dissociation mechanisms of these two cations. Density Functional Theory is applied to calculate molecular structures and static dissociation paths. Moreover, a complementary approach based on extensive molecular dynamics simulations is also used, and the first results allow us to

provide a better view on the dissociation pathways that are statistically explored.

From these computational studies, we could rationalize the experimental trends observed for the two isomers of dibenzopyrene cations, confirming H as the lowest-energy dissociation channel and efficient formation of H_2. We propose that the latter is favored by the specific structure of these PAHs involving the presence of bay regions. In addition, the non-planarity of one isomer leads to an opening of the fragmentation channels at lower energies.

This work brings significant new data for models that describe the chemical evolution of PAHs in astrophysical environments. This includes the first measurement of the ionization yield of medium-sized PAH cations as well as several dissociation rates. We also report a new mechanism that would need to be considered while evaluating the contribution of PAHs to the formation of H_2 in PDRs. Finally, this work opens new perspectives for molecular studies involving the interaction of large carbonaceous molecules such as PAHs with VUV photons.

Résumé

Les hydrocarbures polycycliques aromatiques (PAH en anglais) sont mis en évidence dans les milieux astrophysiques par des bandes caractéristiques dans l'infrarouge, bandes qui sont émises suite à l'excitation de ces molécules par les photons ultraviolets (VUV pour ultraviolet du vide) émis par les étoiles massives. Cette interaction avec le rayonnement influe sur la charge et la stabilité de ces PAH ainsi que sur les mécanismes de dissociation mis en jeu. Ceci affecte, en retour, l'énergétique et la chimie du gaz interstellaire. En particulier, les PAH pourraient contribuer à la formation de la molécule la plus abondante, H_2, dans les régions de photodissociation (PDR). Ce travail apporte une contribution à ce sujet en quantifiant l'interaction du rayonnement VUV avec des PAH de taille moyenne grâce à des études expérimentales et des simulations numériques.

Les résultats expérimentaux ont été obtenus lors de deux campagnes utilisant le rayonnement synchrotron. D'une part, nous avons réalisé des mesures de spectroscopie d'action dans un piège à ions quadripolaire dans le domaine d'énergie 8-20 eV sur la ligne DESIRS à SOLEIL. Les rendements d'ionisation et de fragmentation de plusieurs PAH de taille petite à moyenne (10-24 atomes de carbone) ont été obtenus ainsi que les rapports de branchement entre les différents fragments. D'autre part, des expériences d'imagerie de photoélectrons-photoions en coïncidence (iPEPICO) ont été menées sur plusieurs PAH à la *Swiss Light Source (SLS)* dans le domaine d'énergie de 15.5 à 22 eV. Ceci nous a permis d'obtenir des courbes de fragmentation en fonction de l'énergie des photons VUV pour plusieurs PAH avec une information temporelle supplémentaire. Des taux de dissociation ont été obtenus en ajustant les données expérimentales avec un modèle statistique utilisant la théorie de Rice-Ramsperger-Kassel-Marcus (RRKM).

Pour l'étude détaillée des processus de fragmentation, nous nous sommes focalisés sur le cas de deux isomères du cation de dibenzopyrène ($C_{24}H_{14}^+$) afin d'évaluer l'impact de la structure sur ces processus. En particulier, nous nous sommes intéressés aux voies de basse énergie impliquant la déshydrogénation (perte de H et de $2H/H_2$). Des analyses théoriques ont été menées sur l'énergétique des réactions et les mécanismes de dissociation mis en jeu pour ces deux cations. La théorie de la fonctionnelle de la densité a été utilisée pour calculer les structures moléculaires et les chemins de dissociation statiques. De plus, une approche complémentaire reposant sur des simulations extensives de dynamique moléculaire a été mise en œuvre et les premiers résultats ont permis d'obtenir une meilleure représentation de la statistique d'exploration des chemins de dissociation.

De ces simulations, nous avons pu rationaliser les tendances expérimentales observées pour les deux isomères du cation de dibenzopyrène, confirmant que la perte de H est la voie de dissociation de plus basse énergie et révélant un mécanisme efficace de formation pour H_2. Nous proposons que cette formation est favorisée par la structure particulière de ces PAH impliquant la présence de régions de type « baie ». De plus, la non-planéité de d'un des isomères induit l'ouverture de voies de fragmentation à plus basses énergies.

Ce travail apporte des données moléculaires significatives pour décrire l'évolution chimique des PAH dans les modèles astrophysiques. Ceci inclut la première mesure du rendement d'ionisation pour des PAH cations de taille moyenne ainsi que la détermination de plusieurs taux de dissociation de ces espèces en fonction de l'énergie interne. Nous présentons aussi un nouveau mécanisme qui pourra être considéré dans l'évaluation de la contribution des PAH à la formation de H_2 dans les PDR. Enfin, ce travail ouvre de nouvelles perspectives pour les études moléculaires impliquant l'interaction de molécules carbonées de grande taille comme les PAH avec des photons VUV.

Contents

Description [Fr] 1

CHAPTER 1: ASTROPHYSICAL CONTEXT 5

1.1 The Interstellar Medium (ISM) 6

1.2 Interstellar dust emission 8

1.3 PAH diversity 10

1.4 PAHs and the Aromatic Infrared Bands (AIBs) 11

1.5 The photoprocessing of PAHs in the ISM 15

1.5.1 UV-Photoprocessing conditions 15

1.5.2 Photophysics of PAHs 16

1.6 Laboratory studies on astro-PAHs 18

1.7 Theoretical studies on astro-PAHs 19

1.8 Objectives of this work 21

CHAPTER 2: LABORATORY EXPERIMENTAL TECHNIQUES 23

2.1 Introduction 24

2.2 Synchrotron radiation 25

2.3 Production of gas-phase PAH neutrals and cations 27

2.4 Mass spectrometry (MS) 29

2.5 Time-Of-Flight (TOF) mass analyzers 30

2.6 Principles of ion trapping 31

2.6.1 Penning trap 32

2.6.2 The PIRENEA setup 34

2.6.3 Paul Trap 35

2.7 The LTQ trap at SOLEIL synchrotron facility 39

2.7.1 The DESIRS beamline at SOLEIL 39

2.7.2 The LTQ trap 40

2.8 Imaging PhotoElectron PhotoIon Coincidence (iPEPICO) setup at SLS 42

2.8.1 The VUV beamline at SLS 42

2.8.2 iPEPICO technique and experimental setup 43

2.8.3 Principles of data modelling 45

CHAPTER 3: THEORETICAL MODELLING ____ 47

3.1 Introduction 48
3.2 Electronic structure 48
3.2.1 The Schrödinger equation ____ 48
3.2.2 Density Functional Theory (DFT) ____ 52
3.2.3 Density Functional Tight Binding (DFTB) ____ 55
3.3 Exploration of potential energy surface (PES) 56
3.3.1 Structural optimization ____ 56
3.3.2 Molecular Dynamics (MD) ____ 57
3.4 Statistical calculations: RRKM 58

CHAPTER 4: STABILITY OF TWO DIBENZOPYRENE ISOMERS UNDER VUV RADIATION: LINEAR ION TRAP EXPERIMENTS____ 61

4.1 Introduction 62
4.2 Experimental campaign........ 63
4.3 Evolution of action spectra with VUV photon energy 65
4.4 Ionization and fragmentation 70
4.5 Fragmentation pathways 71
4.6 Discussion 76

CHAPTER 5: ENERGETICALLY FAVORABLE DISSOCIATION PATHS OF DIBENZOPYRENE ISOMERS ____ 77

5.1 Introduction 78
5.2 DFT calculations 78
5.2.1 Direct loss of H____ 79
5.2.2 H+H loss ____ 81
5.2.3 H_2 loss ____ 82
5.3 Discussion: comparison with experimental data........ 86

CHAPTER 6: DYNAMICS OF DISSOCIATION OF DIBENZOPYRENE ISOMERS: IPEPICO EXPERIMENTS, RRKM MODELLING AND MD ____ 89

6.1 Introduction 90
6.2 iPEPICO Experimental details 90

6.3 Breakdown curves and activation parameters 91
6.4 Exploration of dissociation through molecular dynamics . 97
6.5 Comparison of results from different techniques.............. 104
6.5.1 Comparison of activation energies with DFT results ________104
6.5.2 Comparison of threshold energies with ion trap results _____106
6.5.3 Comparison of dissociation rates __________________________107
6.6 Summary and discussion... 108
CHAPTER 7: GENERALIZATION TO MEDIUM-SIZED PAHS, ASTROPHYSICAL IMPLICATIONS _______________________________ 111
7.1 Introduction 112
7.2 Ionization *versus* fragmentation of medium-sized PAHs .. 112
7.3 Activation energies of small and medium-sized PAHs 116
7.4 A new possible route for H_2 formation 120
Conclusions [En] ____123
Conclusions [Fr] ____127

Description [Fr]

L'évolution de l'Univers et des galaxies qui le peuplent est gouvernée par le bilan entre formation et destruction des étoiles constituant chaque galaxie, bilan intimement lié au cycle du matière galactique (gaz et poussière). Dans ce travail de thèse nous nous intéressons aux régions de photodissociation (PDR) qui sont en particulier associées aux régions de formation d'étoiles massives, dans lesquelles la poussière interagit fortement avec les photons ultraviolets (UV) de ces étoiles, donnant lieu à des nombreux processus physiques et chimiques. L'observation astronomique de ces régions avec des télescopes spatiaux comme *ISO*, *Herschel* ou *Spitzer* (et prochainement le *JWST*) a permis d'obtenir des informations spatiales et spectrales sur l'émission de la poussière dans plusieurs environnements galactiques. Ces spectres d'émission ont été modélisés en prenant en compte les différentes populations de grains de poussière, incluant des grains carbonés et des silicates (Figure 1-2). Dans l'infrarouge moyen, des bandes caractéristiques sont observées à des longueurs d'onde autour de 3.3, 6.2, 7.7, 8.6 et 11.3 µm. Elles ont été attribuées à des molécules polycycliques aromatiques hydrogénées (PAH) dans les années 1980. En effet, ces molécules de grande taille (contenant des dizaines d'atomes de carbone) sont isolées dans les PDR et atteignent de hautes températures après l'absorption d'un photon VUV (VUV pour ultraviolet du vide), avant de se refroidir par émission infrarouge. L'interaction des PAH avec le rayonnement VUV peut modifier la nature chimique de ces PAH en les ionisant et/ou en les dissociant. Cela va dépendre de l'environnement dans lequel ces PAH évoluent, en particulier de l'énergie du photon incident (< 13.6 eV dans les régions HI et ~20-30 eV dans les régions HII), mais aussi des propriétés moléculaires de ces PAH (comme leur charge, taille et structure). En retour, l'interaction des PAH avec les photons VUV affecte l'énergétique et la chimie du gaz dans les PDR via en particulier l'effet photoélectrique et une participation à la formation de la molécule H_2. Il est donc important de pouvoir décrire dans les modèles de PDR cette interaction entre PAH et photons VUV.

Afin de mieux comprendre et quantifier les processus liés à cette interaction, il est nécessaire de mener des expériences en laboratoire impliquant des PAH qui sont le plus possible isolés de leur environnement afin de s'approcher des conditions astrophysiques. Lorsque l'objectif est d'étudier l'évolution photophysique et photo-chimique des PAH sur une large gamme de rayonnement VUV, l'accès au rayonnement synchrotron est fondamental. Dans ces conditions, deux types d'expériences sont disponibles qui sont toutes les deux utilisées dans ce travail. En premier lieu, les expériences d'imagerie de photoélectrons-photoions en coïncidence (iPEPICO) nous permettent d'obtenir des « énergies d'apparition » du parent précurseur et des fragments ionisés et d'analyser les courbes de fragmentation avec un modèle statistique pour obtenir des taux de dissociation (West et al. (2018) comme discuté dans ce travail). En deuxième lieu, des expériences en pièges à ions permettent d'atteindre des échelles de temps plus grandes et d'étudier les rapports de branchement entre les voies de fragmentation en fonction de l'énergie interne. Des rendements d'ionisation et de fragmentation en fonction de l'énergie du photon incident peuvent également être obtenus (Zhen et al. (2016b) comme discuté dans ce travail).

La question de la stabilité des PAH en fonction de l'énergie interne peut aussi être abordée par des simulations numériques. Une étude des chemins de fragmentation statiques peut être faite en utilisant la théorie de la fonctionnelle de la densité (DFT). Néanmoins ces chemins peuvent devenir très complexes impliquant de multiples étapes d'isomérisation. Une autre approche possible est celle des simulations de dynamique moléculaire (MD). Les simulations MD utilisant la fonctionnelle de la densité pour des liaisons fortes (DFTB, une approximation de la DFT) permettent d'envisager une exploration extensive des surfaces d'énergie potentielle pour des grandes molécules comme les PAH (Simon et al. 2017). Cette technique DFTB/MD permet d'obtenir une meilleure représentation de la statistique d'exploration des chemins de dissociation.

L'objectif de ce travail de thèse est de tirer profit des techniques expérimentales mentionnées ci-dessus afin d'étudier l'interaction de PAH avec du rayonnement VUV. Il met en jeu deux campagnes expérimentales utilisant le rayonnement synchrotron (SOLEIL et SLS). Plus spécifiquement, il s'agira d'évaluer les rendements d'ionisation et de dissociation, ainsi que la compétition entre les différentes voies de fragmentation en fonction de l'énergie du photon absorbé. Si une très grande diversité de PAH peut être étudiée, ce travail se focalise sur l'étude détaillée de deux isomères du cation du dibenzopyrène $C_{24}H_{14}^+$. Cela permet d'étudier l'effet de la structure avec une comparaison possible avec le cas du cation du coronène, le PAH prototype compact de taille équivalente. La fragmentation des cations dibenzopyrène est étudiée en détail, en particulier les voies à basse énergie qui concernent la déshydrogénation (perte de H, 2H/H_2) (Rodriguez Castillo et al. (2018)). L'analyse des données de laboratoire est approfondie par une modélisation basée sur des calculs de chimie quantique et des simulations MD.

Ce manuscrit de thèse est organisé de la manière suivante : le chapitre 1 présente le contexte astrophysique dans lequel cette thèse est réalisée. Les chapitres 2 et 3 introduisent les méthodes expérimentales et théoriques utilisées. Dans le chapitre 4, je présente des résultats sur les rendements d'ionisation et de dissociation des deux isomères étudiés du dibenzopyrène. Des résultats sur les voies de fragmentation et leur énergétique sont également détaillés. Le chapitre 5 présente les résultats des simulations numériques concernant l'investigation des mécanismes mis en jeu dans les chemins de déshydrogénation. Dans le chapitre 6 les résultats des expériences iPEPICO sont analysés avec un modèle utilisant la théorie de Rice-Ramsperger-Kassel-Marcus (RRKM) afin d'en déduire les taux de dissociation pour la perte d'hydrogène des deux isomères. Cette vue cinétique est complétée par des simulations MD. Le chapitre 7 apporte des éléments de généralisation de notre étude en résumant les résultats expérimentaux obtenus sur un échantillon plus large de PAH de taille petite à moyenne (10-24 atomes de carbone). Ceci est l'occasion de considérations sur l'effet de la taille du PAH et leur structure, avec en particulier la comparaison du dibenzopyrène avec le coronène. Les implications astrophysiques sont discutées. Enfin je finis par les conclusions et quelques perspectives de ce travail.

Chapter 1: ***ASTROPHYSICAL CONTEXT***

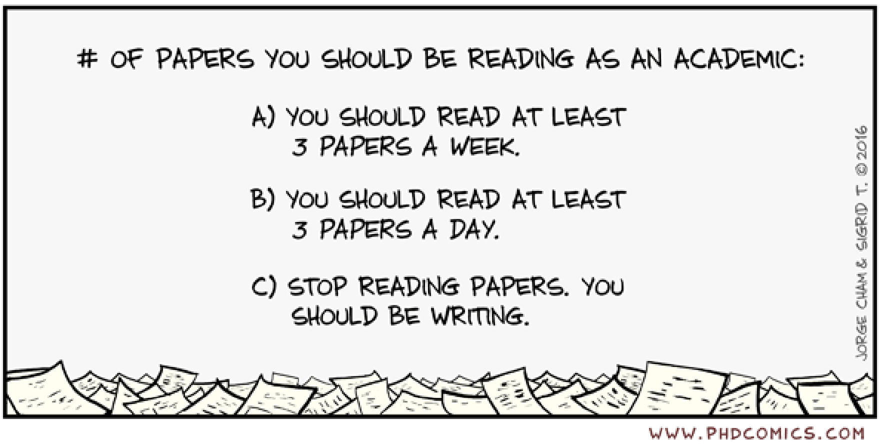
# OF PAPERS YOU SHOULD BE READING AS AN ACADEMIC:
A) YOU SHOULD READ AT LEAST 3 PAPERS A WEEK.
B) YOU SHOULD READ AT LEAST 3 PAPERS A DAY.
C) STOP READING PAPERS. YOU SHOULD BE WRITING.
JORGE CHAM & SIGRID T. ©2016
WWW.PHDCOMICS.COM

1.1 The Interstellar Medium (ISM) 6
1.2 Interstellar dust emission 8
1.3 PAH diversity 10
1.4 PAHs and the Aromatic Infrared Bands (AIBs)..................... 11
1.5 The photoprocessing of PAHs in the ISM 15
  1.5.1 UV-Photoprocessing conditions ______________________________15
  1.5.2 Photophysics of PAHs____16
1.6 Laboratory studies on astro-PAHs 18
1.7 Theoretical studies on astro-PAHs.. 19
1.8 Objectives of this work 21

1.1 The Interstellar Medium (ISM)

Understanding the formation and evolution of our universe and the galaxies within is one of the main objectives in astrophysics. The current theories assume that this evolution is mainly governed by the balance between the formation and the death of the stars within each galaxy (Buonomo et al. (2000)).

As for their formation, all stars are born from collapsing clouds of gas and dust – often called nebulae or molecular clouds – but, depending on their mass, they might undergo different evolutionary paths. For example, the life of a massive star ends with an explosion called supernova, during which the heavy elements that had been formed inside the star by fusion are violently ejected into the interstellar space. In the case of less massive stars, the stellar winds carry away molecules and dust from their circumstellar environments into the interstellar medium (ISM). All these processes enrich the interstellar matter that will then eventually collapse, forming the aforementioned molecular clouds. The cycle of star evolution in a galaxy is intimately coupled to the cycle of matter made of gas and dust (see Figure 1-1). Its study involves a multi-wavelength approach in which observations from several telescopes are gathered.

Focusing on our Galaxy, approximately 10-15% of the total mass of the Galactic disk is found in the interstellar matter: gas (comprising 90% hydrogen and ~10% helium with a small fraction of other elements such as carbon, oxygen, nitrogen…) and small – sub-micronic – dust particles made of oxides, in particular silicates and carbon dust. In the densest regions of the ISM, called dense molecular clouds, the temperatures are as low as 10 K because the radiation field from nearby stars cannot penetrate. With high densities ranging from 10^4 to 10^6 particles cm^{-3}, these clouds are the place where star formation occurs. Because of these conditions, species are found in molecular form, such as H_2 or CO, a stable compound commonly used to trace the interstellar molecular gas.

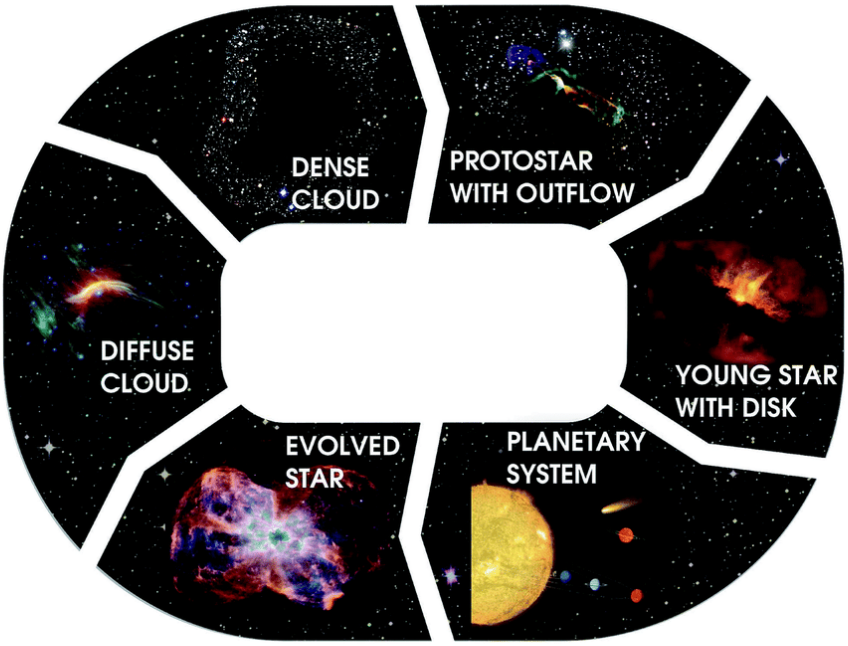

Figure 1-1 Lifecycle of gas and dust in interstellar and circumstellar media. ***Credit: M. Persson, NASA/ESA/ESO/ALMA***

In the external layers of dense clouds, as well as in the diffuse ISM, the stellar UV radiation field is strong enough to dissociate such molecules and ionize carbon, forming C^+. This process rises the gas temperatures up to ~500 K, and the typical density ranges from 10 to ~500 particles cm^{-3}. Finally, translucent clouds contain both molecular and atomic gases and have intermediate characteristics, *i.e.*, a density range of ~500 – 5000 particles cm^{-3} and temperatures of about 15 – 50 K. As explained in detail by Ferrière (2001), the diffuse ISM comprises also other phases, including warm atomic ($T \sim 10^4$ K), warm ionized and hot ionized ($T \sim 10^6$ K) media.

The present work will focus on regions where far-ultraviolet (FUV) photons, with energies between 6 and 13.6 eV, play an important role on the chemical and physical evolution of matter. These photon-dominated regions, also called photodissociation regions (PDRs) (Hollenbach & Tielens (1999)), are present in young bright star forming regions, in planetary nebulae and protoplanetary disks.

1.2 Interstellar dust emission

Dust is an ubiquitous constituent in all the different gas phases mentioned above. Many of the heavy elements in the ISM (Mg, Fe, Si) are primarily present in solid particles, less than 1 µm in size, which are formed in the late stages of star evolution. The composition of these circumstellar dust grains varies from star to star. In particular, it depends on the composition of the ejected gas, which is controlled by the nucleosynthesis process. Depending on the carbon to oxygen ratio of the star, the dust grains will be dominated by carbon atoms ($C/O > 1$) or silicates ($C/O <1$) (Lodders et al. (2009)).

Despite having an insignificant overall mass in comparison to the atomic hydrogen gas mass (around 1%), interstellar dust is determinant in the physics and chemistry of the ISM. It is thought to be a catalyst for the formation of the most abundant molecule, H_2, (Habart et al. (2004); Le Page et al. (2009); Boschman et al. (2015)) as well as for complex organic chemistry (Ehrenfreund & Charnley (2000)). Moreover, it acts as the main heating mechanism of the molecular gas through the photo-electric effect, where the excess energy from the electron emitted from a solid particle after a photon absorption is transferred to the medium (Bakes & Tielens (1994); Weingartner & Draine (2001)).

Observations in the infrared (IR) obtained from space missions outside earth's atmosphere, like the recent *Herschel* or *Spitzer* missions, have allowed us to obtain spectral and spatial information on dust emission for many astrophysical environments in our Galaxy, as well as in nearby galaxies (see for instance Bernard et al. (2008); Compiègne et al. (2010); Ciesla et al. (2014); Kim et al. (2014); Sloan et al. (2014)). The wavelength-dependence of extinction, emission and in some cases polarization of light has been reported in dust models, in which different dust components are included to account for the observations (Zubko et al. (2004); Draine & Li (2007); Compiègne et al. (2011); Siebenmorgen et al. (2014); Galliano (2018)).

An example of fitting the dust spectral energy distribution in the diffuse ISM can be seen in Figure 1-2 from Compiègne et al. (2011). The different dust populations that are proposed are mainly made of carbonaceous and silicate grains with different sizes, from molecular (case of the polycyclic aromatic hydrocarbons) to ~micron size. At low wavelengths, some characteristic features at around 3.3, 6.2, 7.7, 8.6 and 11.3 μm can be distinguished.

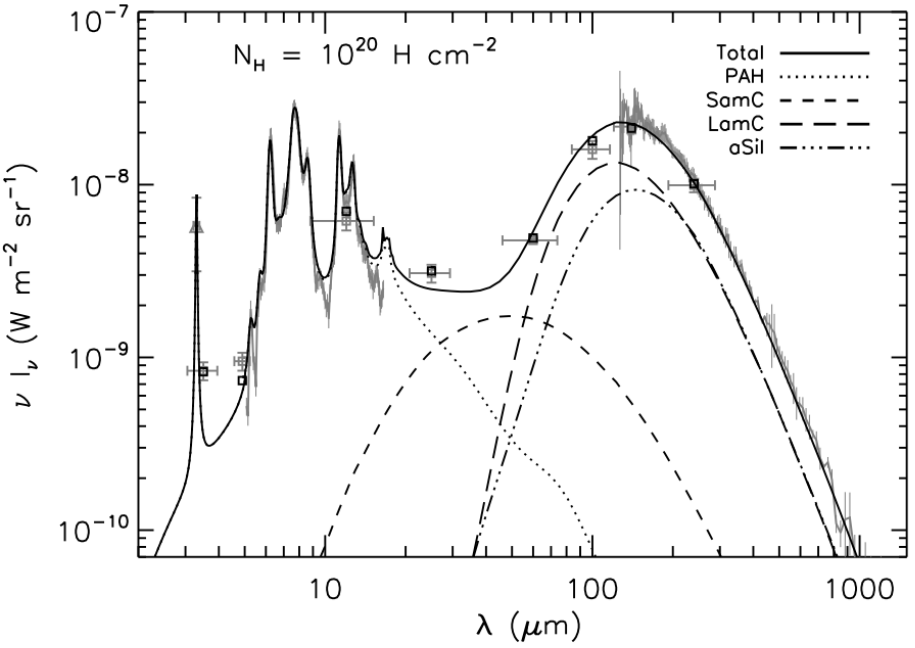

Figure 1-2 Dust emission diagram obtained from an overlap of spectra from *ISO* and *COBE* satellites and *AROME* balloon experiment. Black lines correspond to the model output and black squares represent the photometric measurements from *COBE* after corrections. *Taken from* Compiègne et al. (2011).

These bands, initially referred to as the Unidentified Infrared Bands (UIBs), were initially attributed to very small grains (radius ~10Å) by Sellgren (1984). It was Léger & Puget (1984) and Allamandola et al. (1985) who, after comparison with laboratory data on a family of molecules called polycyclic aromatic hydrocarbons (PAHs), suggested the PAH model. In it, the authors proposed that isolated PAH molecules reach high temperatures after the absorption of a single ultraviolet (UV) photon, and then cool down by (slow) infrared emission, which can be correlated with the observed spectral features. Indeed, PAHs have a small heat capacity (Omont (1986)), so they are able to be heated to the high temperatures associated with the UIB emission, and in particular with the 3.3 μm band, which would require a temperature of ~1000 K. Other molecules in the ISM are destructed after the interaction with a UV photon, but the PAHs are remarkably stable due to the presence of a π resonant system along the carbon rings, which provides them with characteristic properties. This work will focus on this family of aromatic molecules.

1.3 PAH diversity

PAHs are a family of organic molecules composed by two or more aromatic carbon rings containing peripheral hydrogens. These rings are a result of the presence of sp^2 bonds between the carbon atoms, which grant the aromatic behavior to these hydrocarbon molecules. A sample of different PAH molecules is presented in Figure 1-3. When the carbon atoms are shared between more than two rings, PAHs are referred to as pericondensed, while the term catacondensed is used for molecules with a linear-like ring arrangement. In the case in Figure 1-3 examples of the latter would be phenanthrene, chrysene, and pentacene. In this work we study PAHs from an astrophysical perspective, so we will refer to astro-PAHs when discussing PAHs that have been studied under astrophysically-relevant conditions in the laboratory.

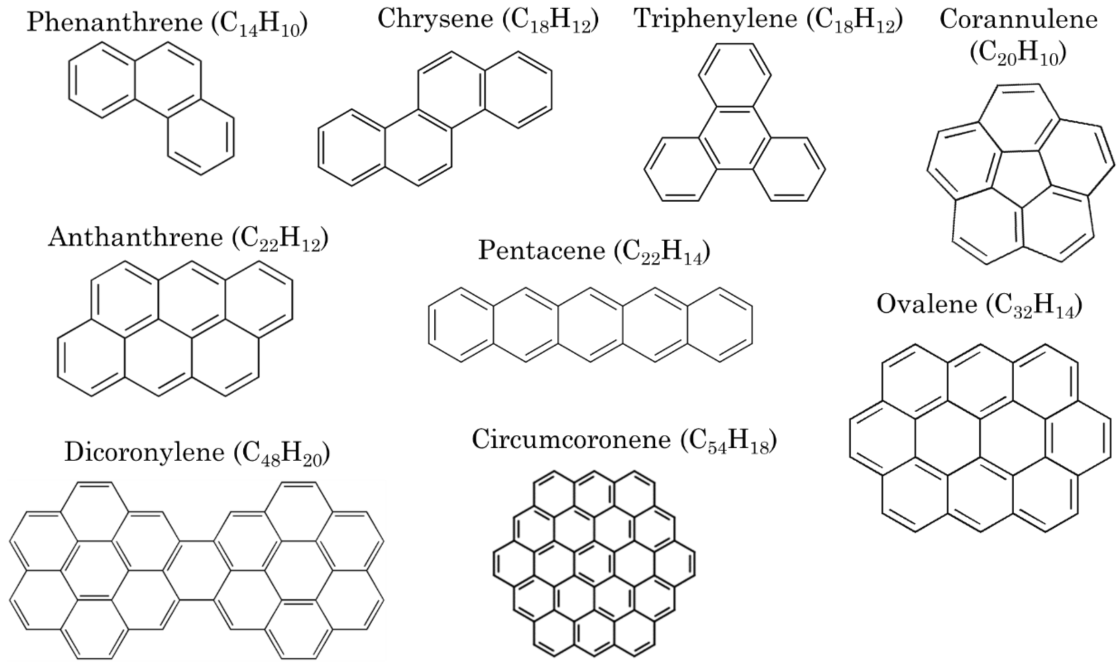
Phenanthrene ($C_{14}H_{10}$)
Chrysene ($C_{18}H_{12}$)
Triphenylene ($C_{18}H_{12}$)
Corannulene ($C_{20}H_{10}$)
Anthanthrene ($C_{22}H_{12}$)
Pentacene ($C_{22}H_{14}$)
Ovalene ($C_{32}H_{14}$)
Dicoronylene ($C_{48}H_{20}$)
Circumcoronene ($C_{54}H_{18}$)

Figure 1-3 Example of PAH molecules. From left to right and top to bottom: penanthrene ($C_{14}H_{10}$), chrysene ($C_{18}H_{12}$), triphenylene ($C_{18}H_{12}$), corannulene ($C_{20}H_{10}$), anthanthrene ($C_{22}H_{12}$), pentacene ($C_{22}H_{14}$), pentacene ($C_{22}H_{14}$), ovalene ($C_{32}H_{14}$), dicoronylene ($C_{48}H_{20}$), circumcoronene ($C_{54}H_{18}$).

1.4 PAHs and the Aromatic Infrared Bands (AIBs)

As mentioned previously, the UIBs, currently better known as the Aromatic Infrared Bands (AIBs), are observed in many astrophysical environments in which UV photons are present to excite their emission. They are especially bright in massive star forming regions leading to bright nebulae (*c.f.* for instance the case of NGC 7023 in Figure 1-5). The diversity of the AIBs is the focus of observational studies in order to get better insights into the composition of the interstellar PAH population and its evolution within different types of astrophysical environments. For further reading on this topic, see for example Tielens (2008) or the proceedings of the symposium organized to celebrate the 25th anniversary of the PAH hypothesis (Joblin & Tielens (2011)).

The main AIBs are located at 3.3, 6.2, 7.7, 8.6, 11.3 and 12.7 µm, and can be attributed to C-H and C-C vibrational modes in PAHs (see Figure 1-4). There are also many weaker bands, which can be used to study the chemical diversity of the PAH population and related species (Allamandola et al. (1989); Peeters (2011)). These include bands at 3.4, 3.5, 5.25, 5.75, 6.0, 6.6, 6.9, 7.2-7.4, 8.2, 10.5, 10.8, 11.0, 12.0, 13.5, 14.2, 15.8, 16.4, 16.6, 17.0, 17.4 and, 17.8 µm (see Peeters (2011) and Figure 1-4). In particular, some of these bands, such as the 3.4 µm band (Joblin et al. (1996)), have been attributed to aliphatic (*i.e.*, non-aromatic) hydrocarbon groups of PAH molecules.

Surprisingly, the shape of the AIBs does not vary significantly depending of different environments (Peeters et al. (2002)). This leads to an open debate on whether their origin resides on a limited number of large and compact PAHs (Andrews et al. (2015)) or is a random combination of a large variety of PAHs, whose spectral statistical product coincides with the observations (Rosenberg et al. (2014)). A bijective correlation of an AIB spectrum to a single PAH molecule or family has not been obtained yet.

The study of the AIB diversity can be approached in different ways. A popular method, used largely by Peeters *et al.*, is to classify the bands in relation with the type of environments (Peeters et al. (2002); van Diedenhoven et al. (2004)). The authors claim that the profiles of the IR emission features vary as a function of the type of source; Type A profiles are obtained from interstellar material illuminated by a star, type B sources are associated with circumstellar material and class C features are detected from extreme carbon-rich post-AGB objects (Sloan et al. (2007)). Class C is assumed to contain unprocessed hydrocarbons, and, as such, higher aliphatic content. On the other hand, classes A and B correspond to environments with more energetic photons and are expected to contain more processed PAHs. This is because the aliphatic bonds are more fragile than the aromatic rings, and would be the first to break under UV processing. The evolution of the aliphatic to aromatic content can be traced by the shift in the position of specific bands, such as the 6.2-6.3 μm band, as demonstrated experimentally by Pino et al. (2008).

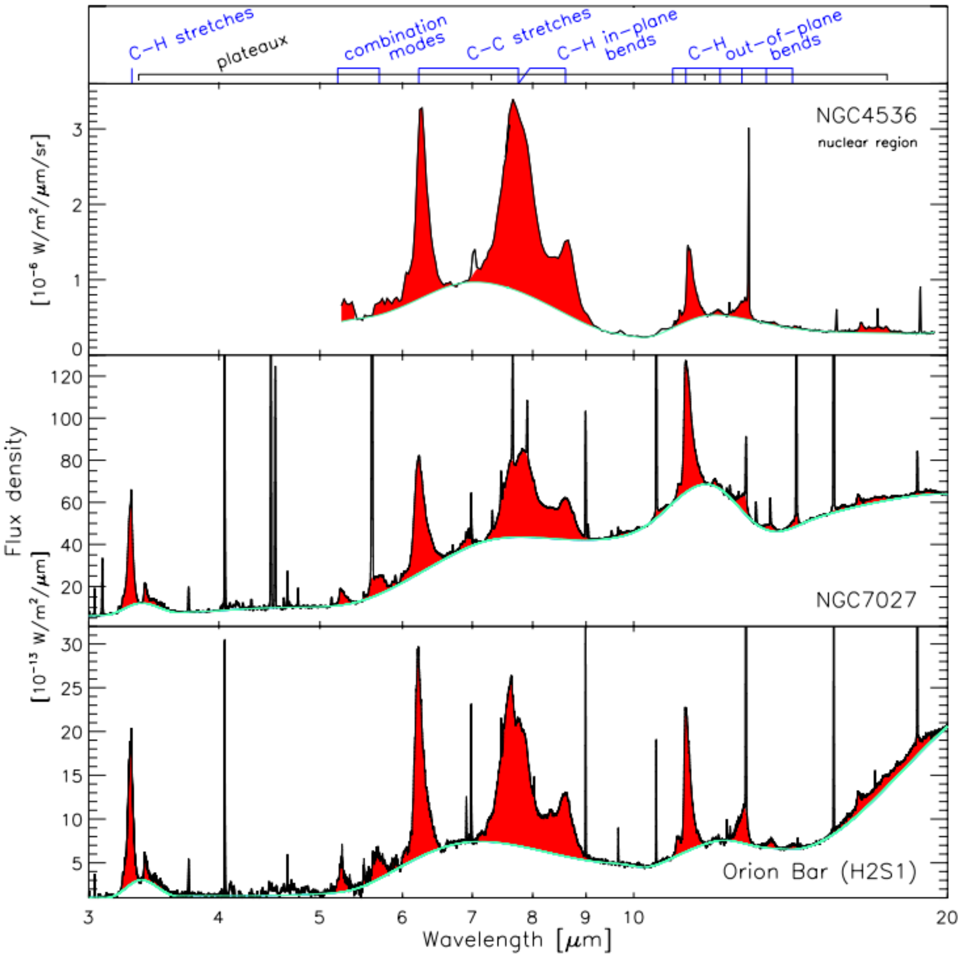

Figure 1-4 Illustration of the PAH spectrum in the ISO-SWS spectra of planetary nebula NGC 4536, planetary nebula NGC 7027 and the PDR at the Orion bar. On the top axis the aromatic mode identifications of the major PAH bands are indicated. *Taken from* Peeters (2011)*)*.

Another approach, used by my PhD group at IRAP, is to apply blind signal separation methods. This decomposition method does not look with detail into all the small bands, but on the global evolution of the main features. Figure 1-5 a) shows an image of a reflection nebula called NGC 7023 NW, where a young star sits inside a cavity created in the molecular cloud by the outbursting winds (Fuente et al. (1999)). Analysis of the spatial variation of the AIBs by Rapacioli et al. (2005), Berné et al. (2007) and Pilleri et al. (2012) suggests that PAHs are produced in these regions by the destruction of very small grains (VSGs) under the interaction with UV photons. The latter study suggested that these VGS contain aliphatic bonds.

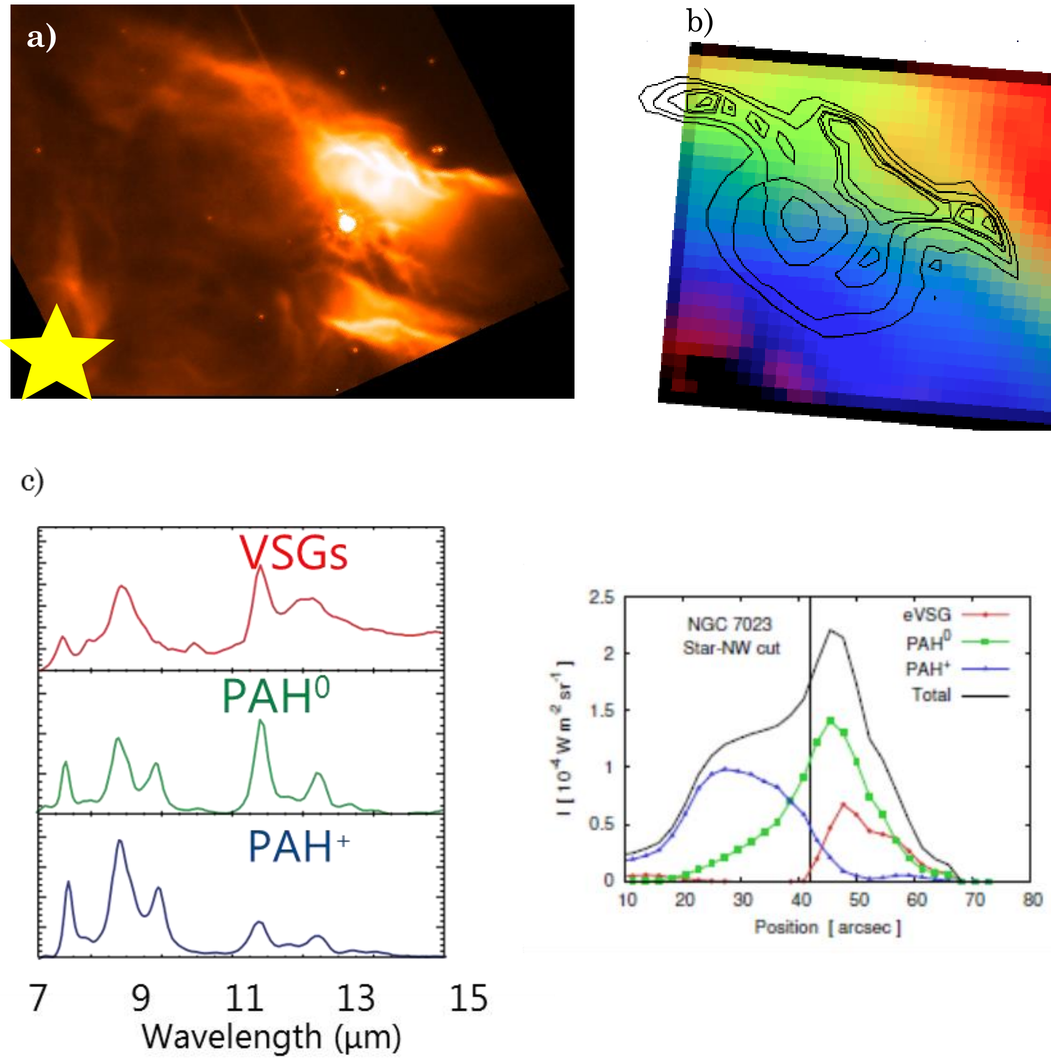

Figure 1-5 Image of a reflection nebula called NGC 7023 NW depicting the young star on the bottom left (Fuente et al 1998). (b) Analysis of the spatial variation of the AIBs by Berné et al., 2007. Signals corresponding to ionized and neutral PAHs are depicted in blue and green respectively, while red corresponds to very small grains (VSGs). The contours are the IR emission at 8 μm showing the

filamentary structure of this PDR (c) *Left:* Simplified blind signal separation spectra and their attribution to different carriers. *Right:* Analysis of the AIB emission in NGC 7023 along the Star-NW cut, using the PAHTAT tool (Pilleri et al. (2012); Montillaud et al. (2013)).

In addition, as one approaches the star, the charge state of the PAH population evolves from neutrals to cations (Figure 1-5 c)) because of the increasing flux of UV photons and decreasing density of electrons that can recombine with cationic PAHs. Analysis of the AIB spectra in different environments has allowed the authors to generalize this photochemical scenario in which PAHs are produced from the evaporation of VSGs (Pilleri et al. (2012)) and their charge state evolve with the physical conditions (Berné et al. (2007), (2009); Joblin et al. (2008)). In the latter two studies, a population of largely ionized PAHs (called PAH^X) was identified in more UV-processed environments such as planetary nebulae and proto-planetary disks. All this shows the role of UV photons, not only in triggering the AIB emission, but also in processing PAHs and their precursors. However, the main drawback of the PAH hypothesis is the fact that no PAH has been individually identified for the moment, despite having been estimated that these molecules account for approximately 10-20% of the total carbon in our Galaxy (Joblin et al. (1992)). This raises many questions on how these molecules are formed and how they are processed by UV irradiation.

Concerning their formation, a common idea is that it involves hot-phase chemistry and possibly subsequent UV processing, which can be found in the envelopes of dying stars. Models of the chemistry in envelopes of asymptotic giant branch (AGB) stars involve a reaction network based on the formation of PAHs and soot in combustion studies (Frenklach & Feigelson (1989); Cherchneff et al. (1992)). However, these models are difficult to test since PAHs have not been observed in AGB stars, most likely because there is not enough UV photons in these environments to observe their IR emission. Another explanation would be that gas-phase photochemistry is necessary to form PAHs. This was suggested by Cernicharo et al. (2001) after the detection of benzene C_6H_6 in the protoplanetary nebula CRL 2688, which corresponds to the next evolutionary stage of the AGB in which the central object contracts, gets hotter and starts to emit significantly in the UV. More recently, the discovery of the benzonitrile molecule (c-C_6H_5CN) in the ISM by Mcguire et al. (2018) has also suggested that small aromatic molecules could act as precursors to form PAHs. The possibility to form PAHs from grain destruction (Cesarsky et al. (2000); Pilleri et al. (2012))

is also invoked and new mechanisms are investigated in the laboratory (Merino et al. (2014) is a recent example). The question of the formation of carbonaceous dust, including PAHs, in astrophysical environments is clearly not solved. This is the focus of the Nanocosmos ERC Synergy project[1] to which I have contributed during my PhD work.

1.5 The photoprocessing of PAHs in the ISM

1.5.1 UV-Photoprocessing conditions

The UV-photoprocessing of PAHs will depend on the amount of energy deposited in the molecule, *i.e.*, on the astrophysical environment. In the so-called HI regions – where hydrogen is found in a neutral form – PAHs are submitted to UV photons of energy up to 13.6 eV, while possibly higher energies (20-30 eV) are involved in HII regions close to massive stars, where hydrogen is ionized and these energetic photons can penetrate. Interaction of PAHs with these UV photons is expected to affect PAHs by ionization and dissociation, as we will discuss in the next section. Chemical models have been developed to describe the evolution of the ionization and hydrogenation states of PAHs in PDRs (Allain et al. (1996); Le Page et al. (2003); Montillaud et al. (2013)). These models suggest that PAHs larger than ~50 carbon atoms can survive UV-photoprocessing whereas smaller ones are processed into carbon clusters. The critical size for PAHs depends on the model, in particular on the reaction rates that have been used to describe all the processes involved: ionization in competition with electron recombination, and photodissociation in competition with reactivity (with hydrogen in particular). It is therefore important to refine these models by providing new molecular data. The interaction of PAHs with UV photons also has an effect on the physics and chemistry of the environment since PAHs are major actors in the photoelectric effect (Bakes & Tielens (1994)) and could significantly contribute to the formation of H_2 (Habart et al. (2004); Boschman et al. (2015)). A recent review on this topic has been prepared by Wakelam et al. (2017).

---

[1] https://nanocosmos.iff.csic.es/

1.5.2 Photophysics of PAHs

To describe the interaction of a PAH with a UV photon one has to understand the photophysics of an isolated molecule including all the possible de-excitation mechanisms that follow the absorption of such a photon. For these large molecules the number of vibrational degrees of freedom increases rapidly with the number of atoms (3N-6), and the density of vibrational states increases steeply with internal energy (see for instance Mulas et al. (2006)). The density of vibrational levels is such that there is a quasi-continuum of states that can couple non-radiatively. Thus, after the absorption of a photon, assuming that no fast ionization takes place (~ few of fs (Marciniak et al. (2015)), the molecule is promoted to an excited electronic state that will decay through fast internal conversion (IC) to lower electronic states of the same multiplicity. Higher multiplicity states are also reachable through inter-system crossing (ISC), although it is a slower process. Then the energy will be redistributed over all the vibrational modes in the electronic state via a radiationless process called intramolecular vibrational redistribution (IVR). We will then have a vibrationally-excited PAH in its electronic ground state that can undergo dissociation processes, or IR-photon emission cooling (k_{IR}~10^2 s^{-1}, Jochims et al. (1994), k_{IR}~10 s^{-1}, Montillaud et al. (2013)). Note that radiative cooling from electronic transitions can also happen in some cases. For neutral PAHs, this is related to direct fluorescence and phosphorescence from low excited states during IC and ISC. For ionized PAHs, the most likely process is referred as recurrent (or Poincaré) fluorescence (Léger et al. (1988)). These steps are represented in Figure 1-6.

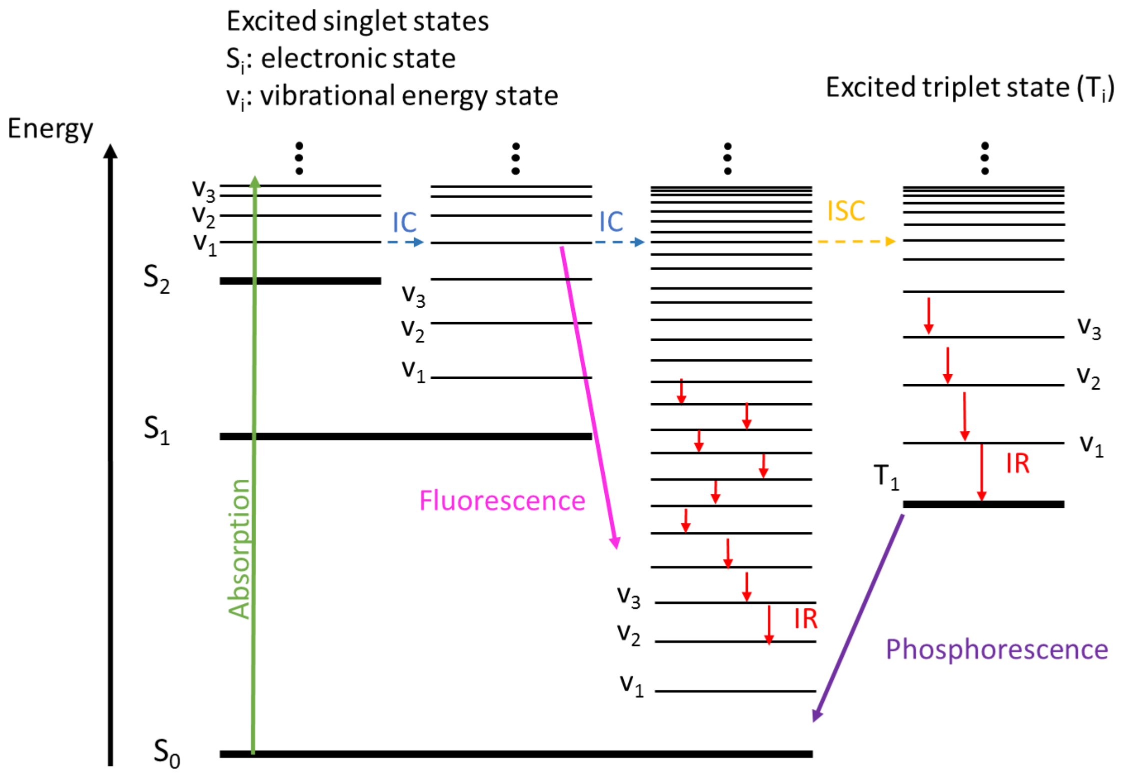
Excited singlet states
S_i: electronic state
v_i: vibrational energy state
Excited triplet state (T_i)
Energy
v_3
v_2
v_1
S_2
S_1
S_0
T_1
IC
IC
ISC
Absorption
Fluorescence
Phosphorescence
IR
IR

Figure 1-6 Jablonski diagram representing the relaxation mechanisms after UV absorption. Non radiative processes are presented in dotted lines: internal conversion (IC) and inter-system crossing (ISC), Radiative processes, such as infrared emission (IR), fluorescence or phosphorescence are presented in full lines.

The balance between all these internal energy relaxation mechanisms will determine the survival of the molecule in a highly isolated environment such as space. This is sketched in Figure 1-7, where the three main processes can be distinguished. In this work, we will study the ionization and photodissociation mechanisms, as well as the individual photofragmentation paths.

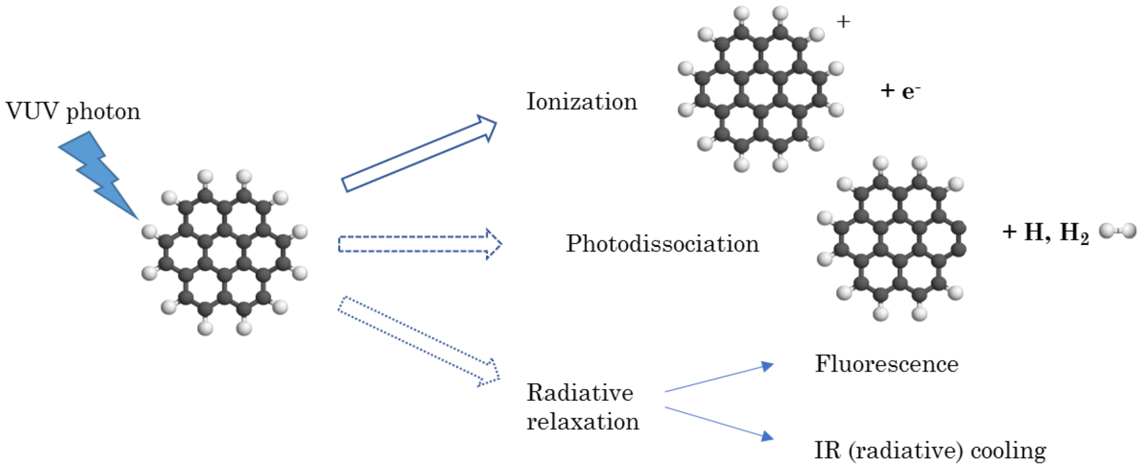

Figure 1-7 Scheme of the possible evolution of a characteristic PAH (coronene, $C_{24}H_{12}^{+}$)) after the absorption of a UV photon, showcasing the main channels at play (ionization, photodissociation and relaxation).

1.6 Laboratory studies on astro-PAHs

In order to better understand which PAHs are more likely to survive the UV processing in interstellar environments, one would like to study their stability in the laboratory under similar conditions, *i.e.*, following their interaction with UV photons in an isolated environment. The energy of these UV photons should be tunable over a large range, as mentioned previously (up to 13.6 eV in HI regions and ~20-30 eV in HII regions). These experiments therefore require access to synchrotron radiation. There are two large classes of such experiments, in both of which I have been involved during my thesis.

The first class relates to photoion mass spectrometry. The idea is to record appearance energies for the parent ion and ionized fragments by interacting gaseous neutral PAH molecules with synchrotron radiation. The energy of the absorbed UV photon is used first to ionize the PAH; the remaining energy will be stored as internal energy in the parent cation, eventually leading to dissociation. In the '90s, such experiments were carried at the Bessy synchrotron in Germany (Jochims et al. (1994), (1999)). From these measurements the authors derived for a set of ~30 PAHs (up to the size of coronene, $C_{24}H_{12}$), the critical energy above which these PAHs would be dissociated in astrophysical environments, in a situation in which dissociation is in competition with IR cooling. For instance, a critical energy of 8.0 and 10.6 eV was derived for pyrene ($C_{16}H_{10}$) and coronene, respectively.

Later, the more precise photoelectron photoion coincidence (PEPICO) technique was introduced with the advantage of measuring the kinetic energy of the electron ejected in coincidence and deriving an accurate value for the internal energy of the dissociating ion. This technique, which will be further described in the next chapter, has been used in particular by the group of Prof. Paul Mayer at the University of Ottawa (Canada) to study the stability of PAHs (West et al. (2012), (2014b)). Analysis of the recorded breakdown curves using density functional theory (DFT) calculations and RRKM modeling allowed them to derive dissociation rates. In a recent publication (West et al. (2018)), to which I have contributed, such rates were obtained for 10 PAHs up to 24 carbon-number species (coronene and 2 isomers of dibenzopyrene, $C_{24}H_{14}$, which are the main focus of this work).

The second class of experiments involves ion trapping. In this case, long time scales can be achieved and the internal energy of the ion is that of the absorbed UV photon, with a small contribution of initial thermal energy stored in the ion. Time-resolved experiments, in which the loss of energized trapped PAH cations is observed, were performed by the group of Lifshitz on 20 μs to 5 ms timescales (see Lifshitz (1997) for a review). Combined with RRKM modelling, these studies provided dissociation rates for a few small PAH cations (up to pyrene). Other ion trap experiments are performed on much longer timescales – typically seconds – and cannot be used to derive directly the dissociation rate (Ekern et al. (1998); Zhen et al. (2015)). However, these experiments are very useful to derive branching ratios between ionization and dissociation, as we described in Zhen et al. (2016b) and briefly summarized in Chapter 7. They are also useful to derive the branching ratios between the different channels, as we will further discuss in Chapter 4.

1.7 Theoretical studies on astro-PAHs

Following the PAH hypothesis, there was a need to obtain a large set of IR spectra for a variety of PAHs of different sizes, shapes, charge-states, including heteroatoms (N, O) or PAHs complexed to atoms of astrophysical relevance (Si, Fe) in order to contrast them with the observationally-detected AIBs. Obtaining experimental IR data is challenging in a number of cases, so theoretical simulations can be regarded as a very attractive alternative. Hartree-Fock methods were first developed and used for describing very small astrophysically-relevant molecules (DeFrees & McLean (1985); Yamaguchi et al. (1986)), and for the smallest PAH, naphthalene ($C_{10}H_8$) (Pauzat et al. (1992)). With the arrival of the efficient Density Functional Theory in the mid-60s and its developments in the exchange-correlation terms in the mid-80s, the theoretical studies of the harmonic IR spectra of astro-PAHs and their derivatives became very popular (Bauschlicher et al. (1999); Bauschlicher & Bakes (2000); Malloci et al. (2004)) leading to the creation of widely used databases by Malloci, et al. (2007)[2] and Boersma et al. (2014)[3]. As an example of the importance of these calculations, we can mention the successful explanation of the 3.3 μm band difference between neutral and ionized PAHs: Quantum studies for several sizes of molecules (Pauzat et al. (1992), (1997); Langhoff (1996)) demonstrated that the collapse of this band observed in astrophysical environments is indeed due to ionization of the PAH, rather than any other process such as dehydrogenation. Another noticeable result is the calculation of the spectra of very large PAHs up to 384 carbons (Ricca et al. (2012)).

The drawback of such approaches is that the DFT-computed IR spectrum is a harmonic absorption spectrum at 0K, although the IR spectra of the ISM are emission spectra from hot (photoexcited) species. Some theoretical efforts have been made to compute IR spectra at high temperatures taking into account anhamonicity effects (Joalland et al. (2010); Calvo et al. (2011); Simon et al. (2011)).

Moreover, theoretical approaches have also been used to describe the dissociation of astro-PAHs (see Simon & Rapacioli (2018) for a review on these theoretical approaches). Fragmentation pathways have been subject to multiple studies with statistical DFT theory (see for instance Jolibois et al. (2005); Thrower et al. (2011); West et al. (2012); Cazaux et al. (2016)). Due to isomerization – especially as the size of the PAH increases – these pathways are often quite complicated (Trinquier et al. (2017a), (2017b)). Accurately describing all of them becomes impossible, and molecular dynamics (MD) simulations are an alternative approach. In particular, MD/DFTB (DFTB stands for Density Functional Tight Binding) allows for exhaustive exploration of the potential energy surfaces of medium to large PAHs, where normal MD/DFT simulations are computationally costly. With this technique, quantitative statistical dissociation results have been obtained for PAH radical cations from naphthalene $C_{10}H_8^+$ to coronene $C_{24}H_{12}^+$ (Simon et al. (2017)). However, this approach presents some limitations, such as the large amount of internal energy required to observe fragmentation on the timescale of the calculations (typically ps) for a reasonable simulation time, or the neglect of electronic excited states. Nevertheless, it still gives us a good insight into the dynamics and evolution of hot PAHs. I have used both DFT static exploration of PES and MD/DFTB simulations in this work; they will be described in Chapter 3.

---

[2] http://astrochemistry.oa-cagliari.inaf.it/database

[3] http://www.astrochem.org/pahdb

1.8 Objectives of this work

The scope of my PhD work is to benefit from the experimental techniques described above to study the fate of PAH cations under UV synchrotron light. More specifically, we aim at evaluating the relative yields between ionization and dissociation as well as the competition between the different dissociation channels as a function of the absorbed UV photon.

A large number of PAHs can be studied; in this work, we will focus on two isomers of dibenzopyrene cation in order to assess the impact of the structure on these processes. Fragmentation is studied in detail with emphasis on the competitive channels at low energies, namely dehydrogenation processes (H, $2H/H_2$ loss), providing information on the energetics of the mechanisms of dissociation. The analysis of the laboratory experiments is largely supported by theoretical modelling based on quantum chemical calculations and molecular dynamics simulations. These include in particular computational studies based on the DFT method, which provides insight into molecular structures and dissociation paths. Furthermore, RRKM modeling is carried out in order to extract dissociation rates. A complementary approach based on extensive MD simulations is also used, and the first results allow to provide a better view on the dissociation pathways that are statistically explored.

This work is organized as follows: Chapter 1 has presented the astrophysical context in which this thesis is carried out. Chapter 2 and Chapter 3 are then dedicated to the introduction of the experimental and theoretical techniques respectively used throughout my PhD. In Chapter 4, we present experimental results on the yields of ionization and fragmentation of the two PAH isomers on which this thesis is focused. Results on the fragmentation mechanisms and energetics are also detailed. Chapter 5 focuses on the computational investigations of the fragmentation mechanisms of these two isomers, especially on the dehydrogenation mechanisms. In Chapter 6, the results of iPEPICO experiments are interpreted by means of RRKM modelling in order to derive dissociation rates for the dehydrogenation paths of these two isomers. This kinetic view is complemented with MD simulations. The final chapter aims at generalizing our study by summarizing the results that have been obtained in our experimental campaigns on medium-sized PAHs (10-24 carbon atoms). We discuss the effects of size and structure on the stability of PAH cations and their astrophysical implications. In particular, the results on dibenzopyrene are compared to those of coronene in order to rationalize the formation of H_2. Finally, the conclusions of this work and some possible perspectives are summarized.

Chapter 2: LABORATORY EXPERIMENTAL TECHNIQUES

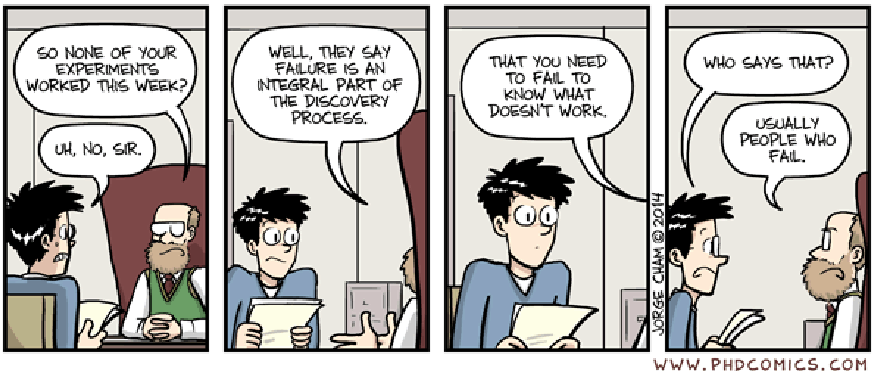
SO NONE OF YOUR EXPERIMENTS WORKED THIS WEEK?
UH, NO, SIR.
WELL, THEY SAY FAILURE IS AN INTEGRAL PART OF THE DISCOVERY PROCESS.
THAT YOU NEED TO FAIL TO KNOW WHAT DOESN'T WORK.
JORGE CHAM © 2014
WHO SAYS THAT?
USUALLY PEOPLE WHO FAIL.
WWW.PHDCOMICS.COM

2.1 Introduction 24
2.2 Synchrotron radiation 25
2.3 Production of gas-phase PAH neutrals and cations............. 27
2.4 Mass spectrometry (MS) 29
2.5 Time-Of-Flight (TOF) mass analyzers..................................... 30
2.6 Principles of ion trapping 31
2.6.1 Penning trap ________________________________ 32
2.6.2 The PIRENEA setup __________________________ 34
2.6.3 Paul Trap ___________________________________ 35
2.7 The LTQ trap at SOLEIL synchrotron facility 39
2.7.1 The DESIRS beamline at SOLEIL ________________ 39
2.7.2 The LTQ trap ________________________________ 40
2.8 Imaging PhotoElectron PhotoIon Coincidence (iPEPICO) setup at SLS.. 42
2.8.1 The VUV beamline at SLS ______________________ 42
2.8.2 iPEPICO technique and experimental setup ________ 43
2.8.3 Principles of data modelling _____________________ 45

2.1 Introduction

In the last couple of decades, the field of laboratory astrophysics has grown considerably, mainly due to the increasing number of techniques available to study the properties of molecules and solids in conditions that approach those found in astrophysical environments (ultra-high vacuum below 10^{-9} and very low temperatures). Which technique to use will depend mainly on the properties under study and on the conditions to be approached. In the case of astroPAHs, isolation from the environment is key in order to avoid relaxation of the internal energy through collisions with background gas, since this process does not occur in interstellar conditions. In addition, PAHs are expected to exist at low temperatures most of the time, typically between the absorption of two UV photons. The previous conditions have justified the extensive use of rare-gas matrix isolation spectroscopy (MIS) to record their electronic spectra (see for example Szczepanski & Vala (1993); Joblin et al. (1994); Salama et al. (1994), Salama et al. (1995)). However, the spectra remain perturbed by interaction with the matrix, which motivated the use of cavity-ring-down spectroscopy to record the spectra of jet-cooled gas-phase PAHs (Tan & Salama (2005), Tan & Salama (2006)). Additionally, ion traps are also used to obtain spectroscopic data on PAH cations. However, in this case, only action spectra can be obtained because the low column density of trapped ions prevents the use of direct spectroscopy. In most cases, a multiple photon absorption scheme is used, leading to the dissociation of the trapped ion, which can be observed in the mass spectrum. A multiple photon dissociation (MPD) spectrum is obtained by scanning the wavelength. It reveals the position of the absorption bands, either in the electronic spectrum (see *e.g.,* Useli-Bacchitta et al. (2010); Zhen et al. (2016a)), or in the vibrational spectrum, the so-called IRMPD technique (see Oomens et al. (2006) for a review). However, in these MPD experiments, the dissociating ion is hot, which affects the recorded spectrum. The development of the cryogenic traps allowed us to use a one-photon absorption scheme on the dissociation of the complex formed by a PAH and a rare gas atom. A noticeable recent result on the electronic spectrum of the fullerene cation, C_{60}^{+}, under this configuration has led to the detection of this ion in the diffuse interstellar medium (Campbell et al. (2015)).

Gas-phase mass spectrometry is also widely used if the interest resides on the ionization and fragmentation pathways of isolated PAHs, where the excitation source is a parameter to be taken into account. For example, internal energy can be deposited into the molecule by collisions with atoms using a multiple collision scheme, or a single, more energetic collision (Mayer & Poon (2009)). These experiments generally use rare gas atoms but collisions with energetic ions are also studied (Postma et al. (2009); Gatchell & Zettergren (2016)). Another example is the use of radiation in order to energize the molecule, as done by West et al. (2014) and Zhen et al. (2014), where a multiple photon absorption scheme was used. All the aforementioned options translate into multiple possible configurations. In the scope of the work presented in this thesis, ion-trap experiments and iPEPICO techniques were used under the incidence of VUV synchrotron radiation. In such cases, absorption of a single UV photon will take place. In the current chapter, these two set-ups will be explained in order to provide the framer under which the following results were obtained.

2.2 Synchrotron radiation

Synchrotron radiation, discovered in the mid-1940s, is emitted by charged, highly energetic particles when they are accelerated in a curved orbit (*i.e.*, acceleration perpendicular to their velocity). In this case, the energy emitted is proportional to the particle speed and inversely proportional to the radius of the path. Based on this principle, several synchrotron facilities have been built over the years in order to provide to the scientific community with a reliable, tunable and high flux source of radiation, as compared with that from lasers (low tuneability) and discharge lamps (low photon flux).

Up to three generation of synchrotron facilities exist, depending on their configuration. This work is carried out on third generation synchrotron facilities, with a typical layout as follows (Figure 2-1): First, electrons are pre-accelerated in a linear accelerator to an intermediate energy of 100 MeV, right before entering the booster. In this circular accelerator, the energy of the electrons is brought up to their final relativistic energy. The exact value depends on the facility (2.4 GeV are reached in the case of the Swiss Light Source and

2.75 GeV in the case of SOLEIL). Then, the electrons are injected into the storage ring, where they follow a straight path until they reach the magnetic dipoles. In these devices their path is bent, and consequently synchrotron radiation is emitted in the direction tangent to the electron trajectory. The energy lost by the electrons is compensated for by radiofrequency cavities along the ring. Additionally, a succession of alternating magnets called undulators is installed on the straight sections of the storage ring. When the electrons pass through this dipole array they are accelerated multiple times, and their trajectory oscillates. With each oscillation, very weak radiation is emitted, due to the weak magnetic field produced by these wigglers. These undulators are built in such a way that these weak radiations overlap and interfere with each other in a constructive way, resulting in very narrow peaks. The synchrotron radiation obtained from an undulator is many orders of magnitude higher as the one generated by bending magnets, but it is composed of harmonics that should be filtered out in order to obtain a peak with very narrow bandwidth.

The spectrum from a synchrotron source ranges from microwaves to hard X-rays, which allows for a fine-tuning and a selection of the desired photon wavelength. Moreover, and thanks to the high flux generated and the possibility for a high collimation, the photon-molecule interaction probabilities are increased. The experiments presented in this manuscript were carried out at the Swiss Light Source (SLS) located in Villigen (Switzerland) and the SOLEIL (acronym for '**S**ource **O**ptimisée de **L**umière d'**E**nergie **I**ntermédiaire du ***LURE***') facility located in Saint-Aubin (France). The specificities of the branch used in each facility will be described in the following sections.

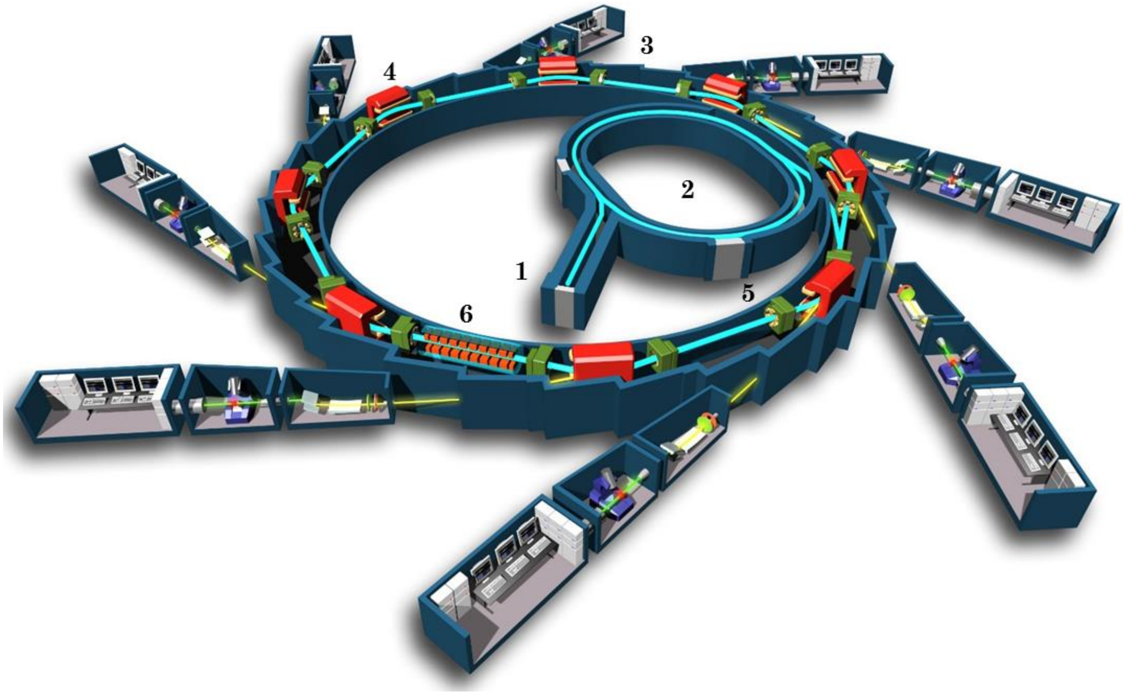

Figure 2-1 Scheme of the synchrotron facility SOLEIL. 1) linear accelerator region, 2) booster, 3) storage ring with several beamlines depicted, 4) bending magnet, 5) RF cavities, 6) undolator. ***Source*: *https://www.synchrotron-soleil.fr***

2.3 Production of gas-phase PAH neutrals and cations

The experiments reported in this work require the production of gas-phase PAH species, either neutrals (for iPEPICO experiments) or cations (ion trap experiments). PAH molecules, found in solid powder form at room temperature, can be brought into the gas phase by different techniques: evaporation from an oven, laser desorption, or by nebulization of a solution. Additionally, gas-phase PAHs can be ionized by several mechanisms; electron impact ionization – in which an energetic electron (~70 eV) collides with the sample molecule – is the harder one and induces significant fragmentation. Another technique consists on irradiating the gas-phase neutral PAHs with UV photons, often in a multiple photon dissociation scheme (*e.g.*, use of the 266 nm Ng:YAG irradiation). Soft ionization techniques have also been developed in particular to study fragile molecules of biochemical interest. These include chemical ionization, field ionization, or atmospheric pressure photo-ionization (APPI), all producing ions with relative small internal energy distributions, and very few fragments (Arlandini et al. (1988)).

In the context of this thesis, APPI was used in the ion trap setup available on the DESIRS beamline (Giuliani et al. (2012)): The PAH sample powder (analyte) is mixed with a solvent, in this case toluene, and this liquid solution is vaporized with the help of a nebulizing gas such as nitrogen. It then enters an ionization chamber at atmospheric pressure where the mixture is exposed to ultraviolet light from a krypton lamp. The photons emitted from this lamp have an energy of 10.6 eV, which is high enough to ionize the target molecules (the ionization potential of PAHs is typically around 7 eV, decreasing with increasing size), but not high enough to ionize air and other unwanted molecules. So only the analyte molecules ($M^{+\cdot}$) proceed to the mass spectrometer to be measured.

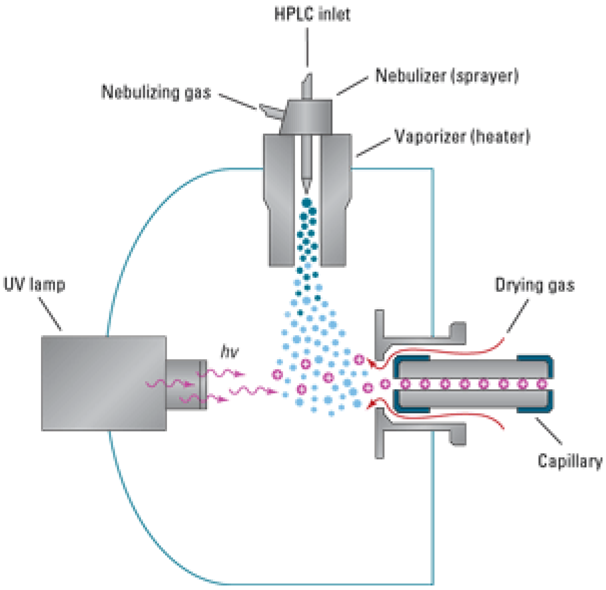

Figure 2-2 Design of the APPI setup. The photons coming from the UV lamp interact with the nebulized gas, ionizing it before it passes through the capillary to the instrument. ***Source:*** ***https://www.agilent.com***

2.4 Mass spectrometry (MS)

After their production, ions must be separated based on their mass-to-charge ratio (m/z) for further analysis. Since they are charged particles, different combinations of static and/or dynamic electric and/or magnetic fields are used in order to achieve this separation. A summary of different families of mass analyzers and the physical principle of separation is shown in Table 2-1.

Table 2-1 Types of mass analyzers and their separation principle. Adapted from de Hoffmann & Stroobant (2007.)

Analyzer type	Symbol	Principle of separation
Electric sector	E or ESA	Kinetic energy
Magnetic sector	B	Momentum
Quadrupole	Q	m/z (trajectory stability)
Ion Trap	IT	m/z (resonance frequency)
Time-of-flight	TOF	Velocity (time of flight)
Fourier transform ion cyclotron resonance	FTICR	m/z (resonance frequency)
Fourier transform orbitrap	FT-OT	m/z (resonance frequency)

Each of these mass analyzers is suitable for a certain application. In this work, both linear quadrupole ion trap and time-of-flight mass analyzers are used to study the target ions. Their physical principles of operation are summarized in the following sections.

2.5 Time-Of-Flight (TOF) mass analyzers

In a TOF mass analyzer, the ions with mass m, and charge $q = ze$, are separated according to the velocities that they have gained after being accelerated in a constant electric field. The schematic principle of a linear TOF instrument is presented in Figure 2-3.

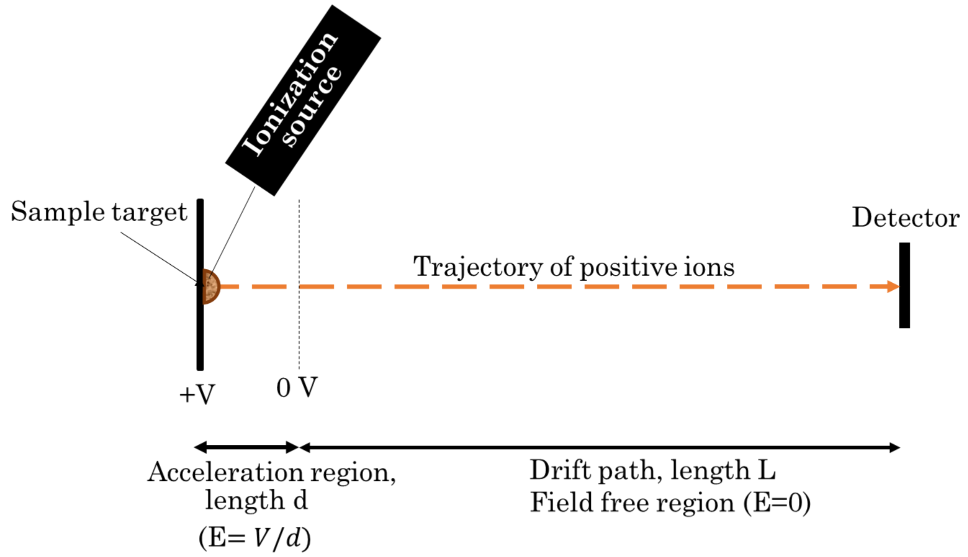
Ionization source
Sample target
Detector
Trajectory of positive ions
+V
0 V
Acceleration region, length d
(E= V/d)
Drift path, length L
Field free region (E=0)

Figure 2-3 Schematic operation principle of a TOF. The sample target is irradiated by an ionization source, and the formed ions are subject to the applied electric field. They are accelerated before drifting into the free-field region, where the travel with a velocity proportional to their m/z ratio before being detected in the detector as a function of their arrival time.

Right after their production, they are accelerated towards the flight tube by a difference of potential (V) applied in the acceleration region. This electric potential energy ($E_{el} = qV = zeV$) is then converted into kinetic energy ($E_k = \frac{mv^2}{2}$). The velocity of the ions right after leaving the acceleration region is thus:

Equation 2-1

$$v = \sqrt{\frac{2zeV}{m}}$$

After this acceleration, the ion drifts into the free-field region where it will travel at a constant velocity before reaching the detector. This velocity is function of the size of the drift tube, L, and the time that the ions need to cover this distance, t ($v = L/t$). By replacing this value of v in Equation 2-1, we obtain:

Equation 2-2

$$t^2 = \frac{m}{z}\left(\frac{L^2}{2eV_s}\right)$$

Mass-to-charge ratios are then determined only by measuring the time that ions take to move through the field-free region between the source and the detector, located at the other extremity of the flight tube.

TOF spectra can be obtained in microseconds, but most of the times they lack the required precision due to the weak number of ions detected in each individual spectrum. For this reason, recorded spectra are generally the addition of a number of individual spectra. The most important drawback of the first TOF analyzers was their poor mass resolution, which is a function of the flight time and flight path. A compromise in tube lengths and acceleration voltage is needed in order to have high resolution and sensitivities.

2.6 Principles of ion trapping

Confining particles in a region of space for a long period of time in order to study processes at long timescales is a very interesting opportunity brought by ion traps. The Earnshaw's theorem states that one cannot construct a stable ion trap using only electrostatic fields. Therefore traps using either dynamic electric fields (Paul trap) or electromagnetic fields (Penning trap) are used to trap ions. These techniques are commonly used in chemical mass analyzers, for determining the molecular weights of complex compounds with high precision. During my PhD, I mainly used a Paul trap, but I also participated to test experiments using the PIRENEA setup at IRAP, which is based on a Penning trap. For this reason, I will briefly describe the principle of both types of traps.

2.6.1 Penning trap

The Penning trap stores charged particles in the radial direction by means of a strong homogeneous axial magnetic field, and in the axial direction using a quadrupole electric field with a set of three electrodes- a ring and two endcaps (other geometries are possible; for instance in PIRENEA, the trapping electrodes are open cylinders). In order to trap positive ions, the endcaps can be kept at a positive potential relative to the ring, producing a saddle point in the center of the trap and confining the ion oscillating motion to the axial direction. The perpendicular magnetic field **B** forces the ions to move in phase in the radial plane. A scheme of this mechanism is shown in Figure 2-4.

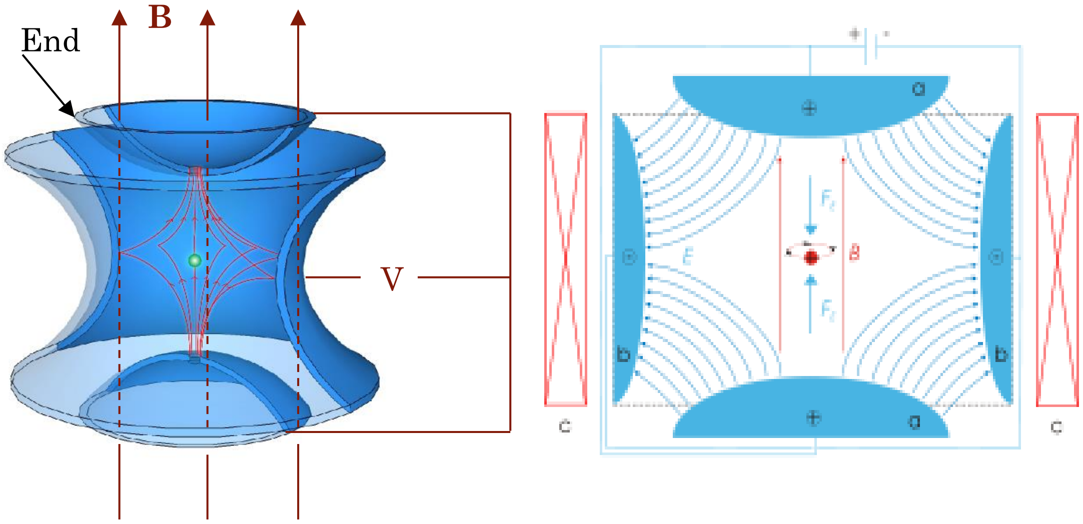

Figure 2-4. Schematic design of a Penning trap (left). The right image shows the trapping of the cation in the center, due to the electric field produced between the (a) and (b) electrodes and the magnet field (B) produced by a toroidal electromagnet. *Figures by Arian Kriesch.*

This orbital motion of the ions in the radial plane depends only on the mass to charge ratio and on the strength of the magnetic field. Its expression, derived from the equality between centripetal force and magnetic Lorentz force, gives the so-called cyclotron frequency:

Equation 2-3

$$\frac{m\boldsymbol{v}^2}{\boldsymbol{r}} = q\boldsymbol{B}\boldsymbol{v}$$

Where m is the mass of the ion, v its velocity, r is the cyclotron radius, q is the charge of the particle and B is the intensity of the magnetic field. As we know, the frequency can be expressed as a function of the velocity as $f = v/2\pi r$. Then, $f = \frac{qB}{2\pi m}$ or, as a function of the angular frequency:

Equation 2-4

$$\omega = 2\pi f = \frac{qB}{m}$$

This cyclotron frequency is independent of the particle's kinetic energy. A modified version of this cyclotron frequency is, together with the magnetron frequency, an eigenvalue of the equations of motion in the radial direction. In the axial direction the movement of the ion package corresponds to a harmonic oscillation and the axial frequency is proportional to the charge and to the applied electric field and indirectly proportional to the mass and to the radius. The total motion of a charged particle inside a Penning trap is shown in Figure 2-5.

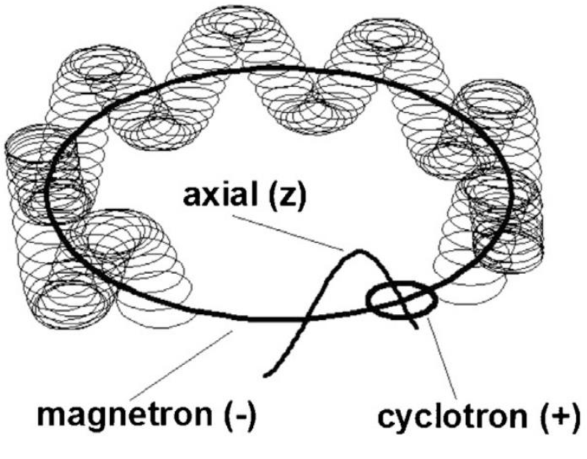

Figure 2-5 Motion of a charged particle inside a Penning trap. It is the superposition of the axial, magnetron, and cyclotron motions. ***Taken from Kluge (2013).***

Penning traps constitute the core of Fourier Transform Ion Cyclotron Resonance (FT-ICR) mass spectrometry, used for determining the mass-to-charge ratio (m/q) of the trapped ions at very high resolution (Marshall et al. (1998)). A radio frequency sinusoidal voltage is applied to the excitation plates and only ions that have their cyclotron frequency in resonance with the applied electric field are driven into a coherent motion. The remaining ions, off resonance, do not absorb energy and remain at the center of the cell, as shown in Figure 2-6. The signal is obtained through the image current that the coherently orbiting ion packet induces in the plates. This time-domain signal, amplified and digitalized, is finally Fourier-transformed to retrieve a frequency domain mass spectrum.

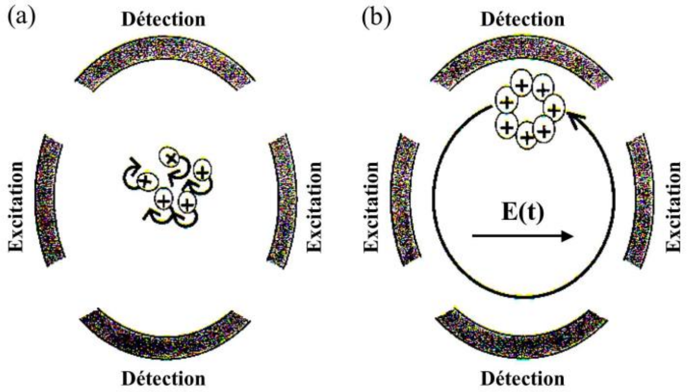

Figure 2-6 Motion of the ions inside a FT-IRC. a) No electrical field applied. b) Motion of the ions with cyclotron frequencies in sync with the excitation field. ***Adopted from Useli-Bacchitta (2010).***

2.6.2 The PIRENEA setup

PIRENEA (Piège à Ions pour la Recherche et l'Etude de Nouvelles Espèces Astrochimiques) is an in-house built experimental set-up located in the Institute of Astrophysical Research (IRAP) in Toulouse, France. This setup is dedicated to laboratory astrophysics activities. One of its specificities is that the FT-ICR trap is held at cryogenic temperature (~ 30 K). At these temperatures, the residual pressure inside the vacuum chamber is found to be less than 10^{-10} mbar, and thus the trapped ions are isolated on long timescales from the background (collisions and thermal radiation). Gas-phase PAHs are produced by laser desorption from a solid target, and ~10^6 ions are stored in the trap. The ions of interest can be selected and isolated by selective ejection of other species. Their photostability can be studied using a MPD scheme by irradiation with a xenon lamp (UV-visible range). Some results are reported in Simon & Joblin (2009) and Montillaud et al. (2013). A description of the setup, including Figure 2-7, can be found in Useli-Bacchitta (2010).

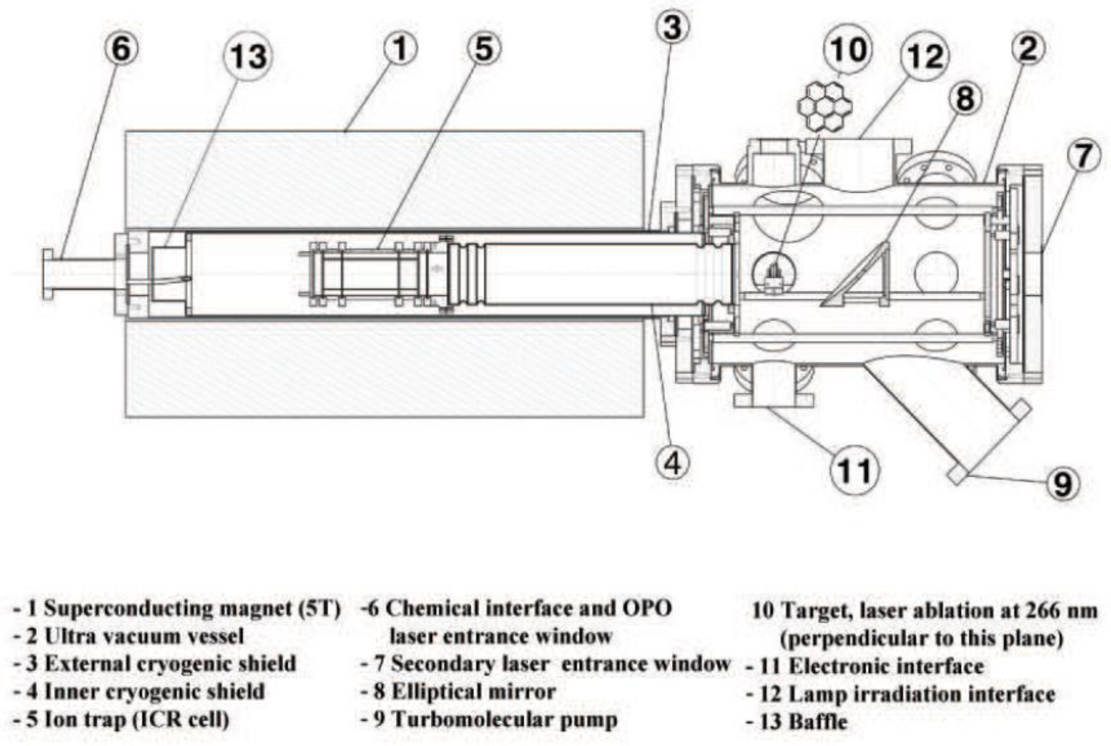
6
13
1
5
3
10
12
2
8
7
4
11
9
- 1 Superconducting magnet (5T)
- 2 Ultra vacuum vessel
- 3 External cryogenic shield
- 4 Inner cryogenic shield
- 5 Ion trap (ICR cell)
-6 Chemical interface and OPO laser entrance window
- 7 Secondary laser entrance window
- 8 Elliptical mirror
- 9 Turbomolecular pump
10 Target, laser ablation at 266 nm (perpendicular to this plane)
- 11 Electronic interface
- 12 Lamp irradiation interface
- 13 Baffle

Figure 2-7. Scheme of the PIRENEA setup, (Useli-Bacchitta (2010)).

2.6.3 Paul Trap

Electrodynamic ion traps, or radiofrequency traps, are widely used setups that use a combination of static and dynamic electric fields to store ionized species. They are also known as Paul traps, in honor of Wolfgang Paul and Hans Dehmelt who received the Nobel Prize for Physics in 1989 for their development. A full theoretical description of the technique can be found, for example, in March (1997).

Typically, the particles are confined by cylindrical electrodes that create a quadrupole electric field geometry as depicted in Figure 2-8. Roughly, a confining potential with a saddle point is achieved by optimizing the geometry of the trap and applying a voltage to its electrodes that oscillates with time (typically at RF frequencies). At any given time, the field is uniform between the electrodes and the average position of the ions remains constant.

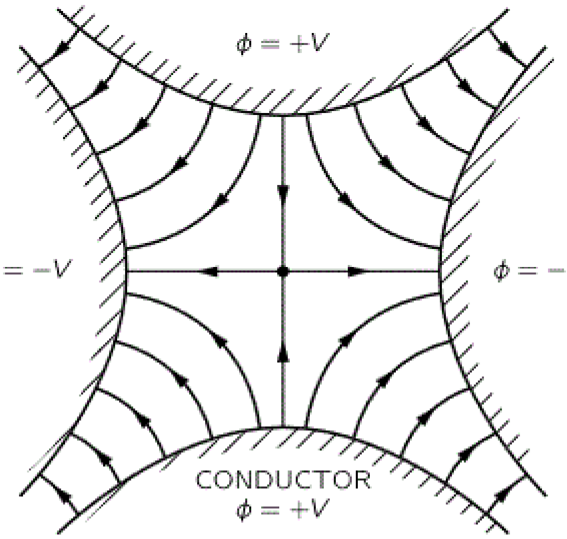

Figure 2-8 Quadrupole electric field created by hyperbolic conductors.

Two main configurations of the Paul trap are typically used: the 3-dimension Paul trap, also known as quadrupole ion trap (QIT), and the linear ion trap (LIT) made of four parallel electrodes and end electrodes to which stopping potentials are applied. The latter have higher injection efficiencies and higher ion storage capacities than 3D Paul traps. For an electric quadrupole field, the parabolic potential expressed in Cartesian coordinates, has the general form (Equation 2-5):

Equation 2-5

$$\Phi = \frac{\Phi_0}{2r_0^2}\,(\lambda x^2 + \sigma y^2 + \gamma z^2)$$

Where λ, σ, γ are weighting constants and Φ_0 is the time-dependent voltage applied to the pairs of electrodes. This voltage has the form: $\Phi_0(t) = 2(U + V\cos(\omega t))$, where U is direct current (DC) voltage and V is the amplitude of the RF voltage with an angular frequency ω.

Upon applying the Laplace condition ($\Delta\Phi = 0$), one obtains that the sum of the weighing constants must be 0: $\lambda + \sigma + \gamma = 0$. Typically, two cases are presented in which this condition is met:

i) $\lambda = -\sigma = 1$ and $\gamma = 0$, in LIT
ii) $\lambda = \sigma = 1$ and $\gamma = -2$, in QIT

The LTQ XL setup from Thermo Scientific used in this work is a Linear Triple Quadrupole ion trap. For this reason, the principles of linear ion trapping will be further explained. A schematic design of a LIT can be seen in Figure 2-9.

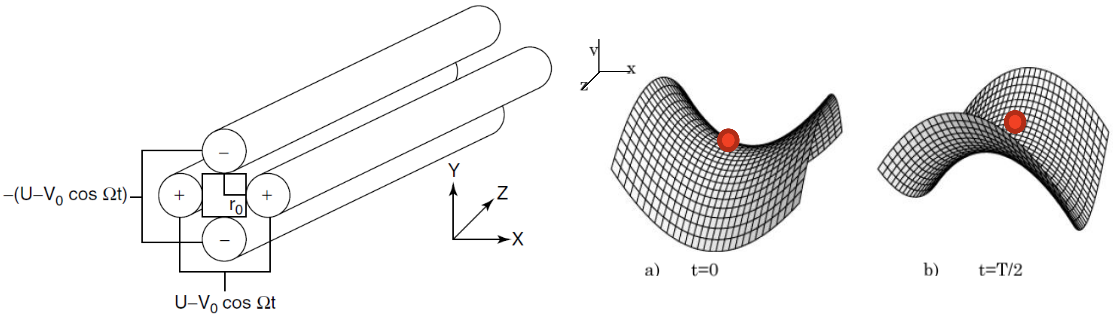

Figure 2-9 Left: Scheme of a linear 4-rod geometry of a Paul trap. The oscillation is controlled by the DC (U) and RF (V) potentials applied to each pair of the rods (*taken from March & Todd (2005)*). Right: Scheme of the potential surface created in a Paul trap. a) At t=0 the particle is confined in the left-right direction. b) In the second half of the period the particle becomes confined in the perpendicular direction.

The ions accelerated along the Z axis maintain their velocity along this axis ($\ddot{z} = 0$), while the equations of motion along the XY plane are derived from Newton's second law:

Equation 2-6

$$\begin{tikzcd} & \ddot{x} + \frac{2e}{m\,r_0^2}\,(U + V\cos\omega t)\,x = 0 \\ m\frac{d^2\boldsymbol{r}}{dt^2} = -e\,\nabla\Phi \arrow[ur] \arrow[dr] & \\ & \ddot{y} - \frac{2e}{m\,r_0^2}\,(U + V\cos\omega t)y\; = 0 \end{tikzcd}$$

These equations have the form of the second-order Mathieu differential equation, which in general terms is:

Equation 2-7

$$\frac{d^2u}{d\,\xi^2} + (a_u - 2q_u\cos 2\xi)\,u = 0$$

By correlating terms, one obtains the expression of the parameters a_u, q_u and ξ for u=x and u=y:

Equation 2-8

$$\xi = \frac{\omega t}{2}$$

$$a_x = -a_y = \frac{8eU}{mr_0^2\,\omega^2}$$

$$q_x = -q_y = -\frac{4eV}{mr_0^2}\omega^2$$

The solutions of the Mathieu equation can be characterized either as stable or unstable based on how their coordinates evolve over time. For any given ion with a mass m and a charge e, only certain combinations of a_u and q_u (defined by the voltages U and V applied on the quadrupole) provide stable solutions. Plotting these parameters we obtain the stability diagram, showing the areas in which the ion motion will be stable in the X and Y directions (shadowed areas in Figure 2-10 a), and in the XY plane (areas I, II and III of the same figure). The area I is the one most commonly used in mass spectrometers, and is enlarged in Figure 2-10 b).

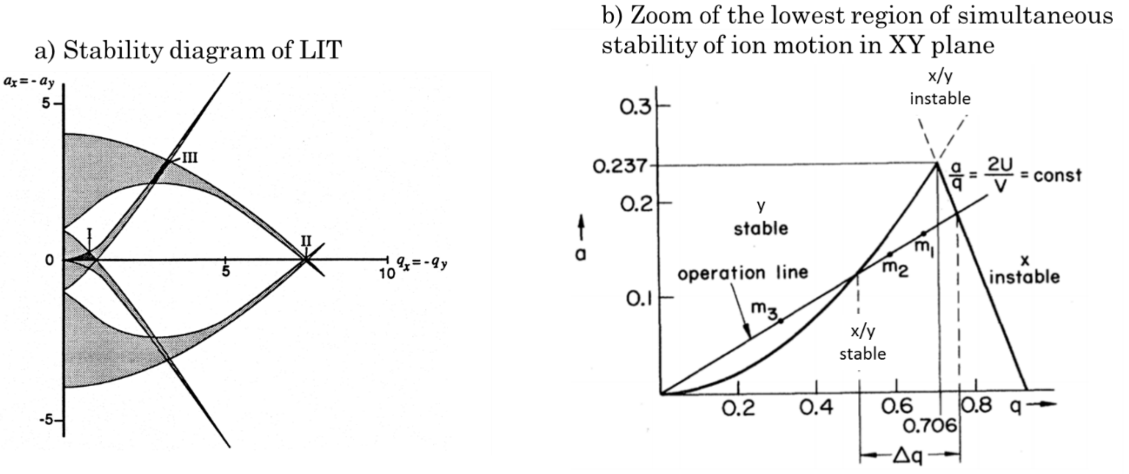

a) Stability diagram of LIT

b) Zoom of the lowest region of simultaneous stability of ion motion in XY plane

Figure 2-10 a) Stability regions in the X and Y axes of the LIT are indicated by the shaded areas. Roman numbers indicate the stability areas along the XY plane. *Taken from Du & Douglas (1999).* b) Zoom on the most commonly used overlapping region near the origin of the quadrupole. Ions which fall into this region for a given set of trapping conditions will remain in the trap (*adapted from Paul (1990)).*

In the previous figure, the operation line indicates the values for which the ratio a/q is constant ($\frac{a}{q} = 2U/V$) and independent on the ion masses and charges. If voltages U and V are simultaneously scanned in a way that their ratio stays constant, then only the ions with successive m/z ratio will have the stable trajectories inside the quadrupole. This procedure allows us to scan the mass spectrum; therefore, the quadrupole will work as a mass spectrometer. By adding axially two more sections (with the same electrode profile) with different electrostatic potential before and after the quadrupole mass filter, ion trapping can be achieved and the linear quadrupole ion trap can be constructed.

2.7 The LTQ trap at SOLEIL synchrotron facility

2.7.1 The DESIRS beamline at SOLEIL

The DESIRS (Dichroïsme Et Spectroscopie par Interaction avec le Rayonnement Synchrotron) beamline is a VUV beamline located in the SOLEIL synchrotron facility in France, featuring a high photon flux and an energy range from 5 to 40 eV. A detailed description of this beamline can be found in Nahon et al. (2012). Briefly, the electrons that have circulated for several hours in the 113m-diameter storage ring pass through dipoles and undulators that make them oscillate and emit energy in the form of synchrotron radiation with an adjustable polarization. Any present high harmonics are filtered out by a gas filter (Krypton up to 14 eV and Argon up to 16 eV), after which the pink beam falls on a 6.65 mm normal incidence monochromator to provide energy selection (monochromatic beam). Using the first order grating in this configuration allows us to obtain an average flux in the $10^{12} – 10^{13}$ photons s^{-1} range. The synchrotron light can be considered as continuous in our experimental conditions.

Three branches, A, B and C, are available in DESIRS and can be seen schematically in Figure 2-11. Branches A and B share a normal incidence monochromator (NIM) and are suited to perform photodynamics, spectroscopy and dichroism experiments with an optimized resolution/flux compromise and variable polarization (Nahon et al. (2012)). In particular, branch A comprises the multipurpose molecular beam chamber, SAPHIRS, consisting of a source chamber and an ionization chamber separated by a skimmer. The latter is connected to a PEPICO setup that has been used for the study of PAHs and PAH clusters for example in Bréchignac et al. (2014); Rouillé et al. (2015); Joblin et al. (2017). Branch B is open for users. The LTQ ion trap setup is coupled to this branch, and will be described further in detail. Branch C contains a permanent experimental setup for ultra-high resolution Furrier transform absorption spectroscopy (FTS) in the 5-30 eV range.

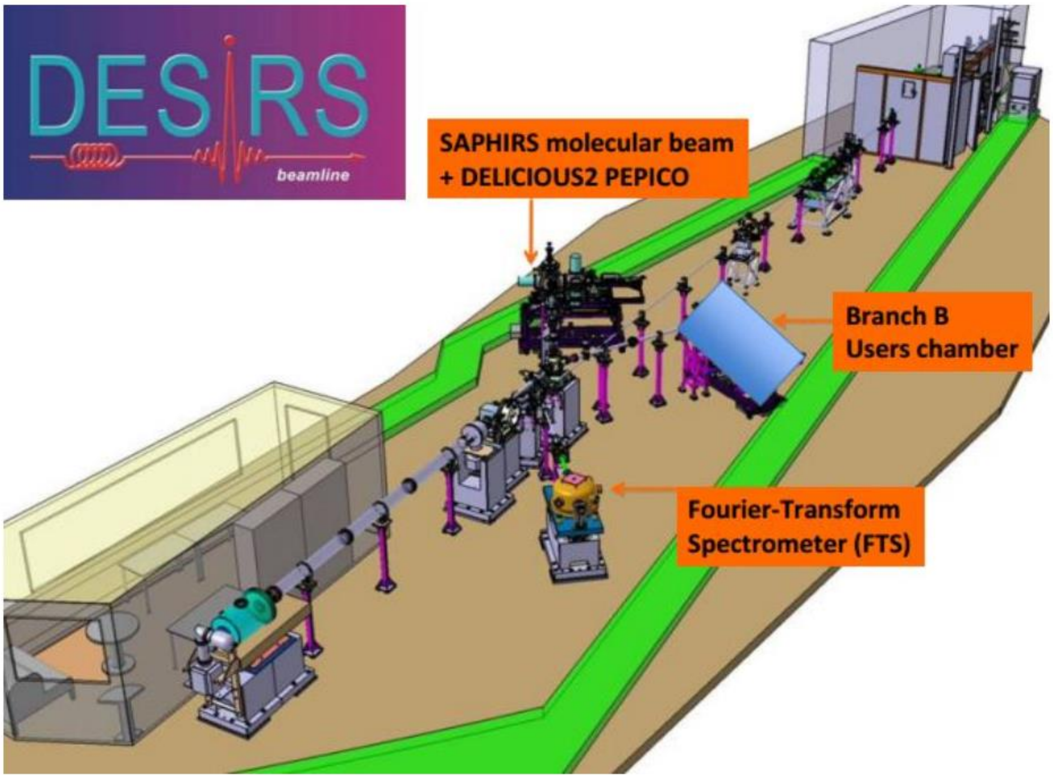
DESIRS
beamline
SAPHIRS molecular beam + DELICIOUS2 PEPICO
Branch B Users chamber
Fourier-Transform Spectrometer (FTS)

Figure 2-11 Schematic representation of the DESIRS beamline at SOLEIL. ***Taken from https://www.synchrotron-soleil.fr/en/beamlines/desirs***

2.7.2 The LTQ trap

The experimental setup (Figure 2-12) consists in the coupling of a commercial LTQ (Thermo Scientific LTQ XL) with the DESIRS beamline at the SOLEIL facility (Milosavljevic et al. (2012)). The complete setup is equipped with an APPI source that ionizes the PAHs prior to entering an octopole, where they are focused before reaching the LTQ. This configuration provides multiple functionalities. On the one hand, only the species of interest are selected; other ions including isotopic species, and fragments, if they are present, are ejected.

On the other hand, the ions of interest are stored and thermalized at room temperature (293 K) by collisions with helium atoms before photoprocessing. Synchrotron photons reach the ion trap during a certain irradiation time, controlled by a beam shutter in the vacuum chamber and selected to obtain the best signal. The VUV beam is sent directly into the linear ion trap, with a spot size of ~0.3 mm^2 in the center position. The shutter is closed 50 ms before the end of the actual mass analysis in order to stop the interaction of photons with ions before the detection of the ion fragments. Photo-products are recorded as a function of the incident photon energy.

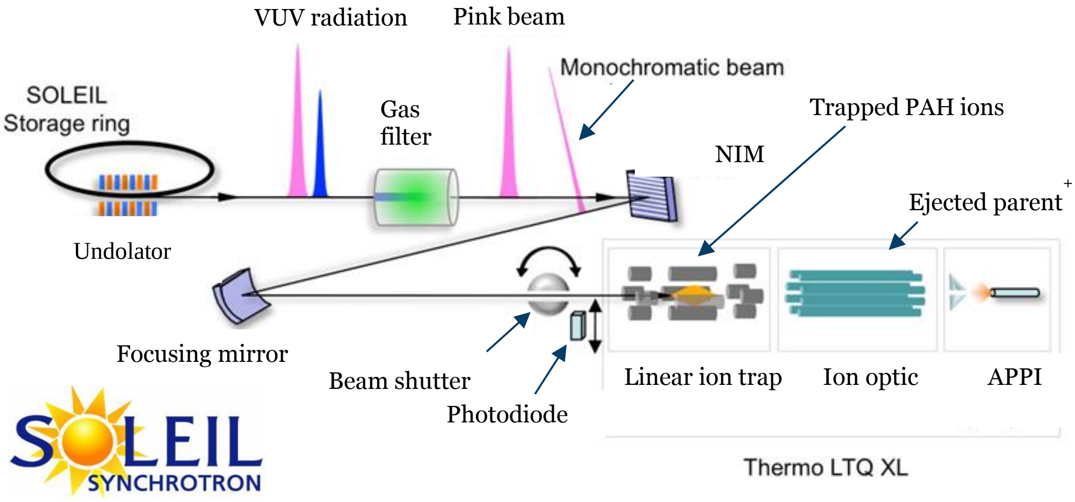
VUV radiation
Pink beam
Monochromatic beam
SOLEIL
Storage ring
Gas
filter
Trapped PAH ions
NIM
Ejected parent +
Undolator
Focusing mirror
Beam shutter
Photodiode
Linear ion trap
Ion optic
APPI
SOLEIL
SYNCHROTRON
Thermo LTQ XL

Figure 2-12 Scheme of DESIRS beamline ***(Adapted from Milosavljevic et al. (2012)).***

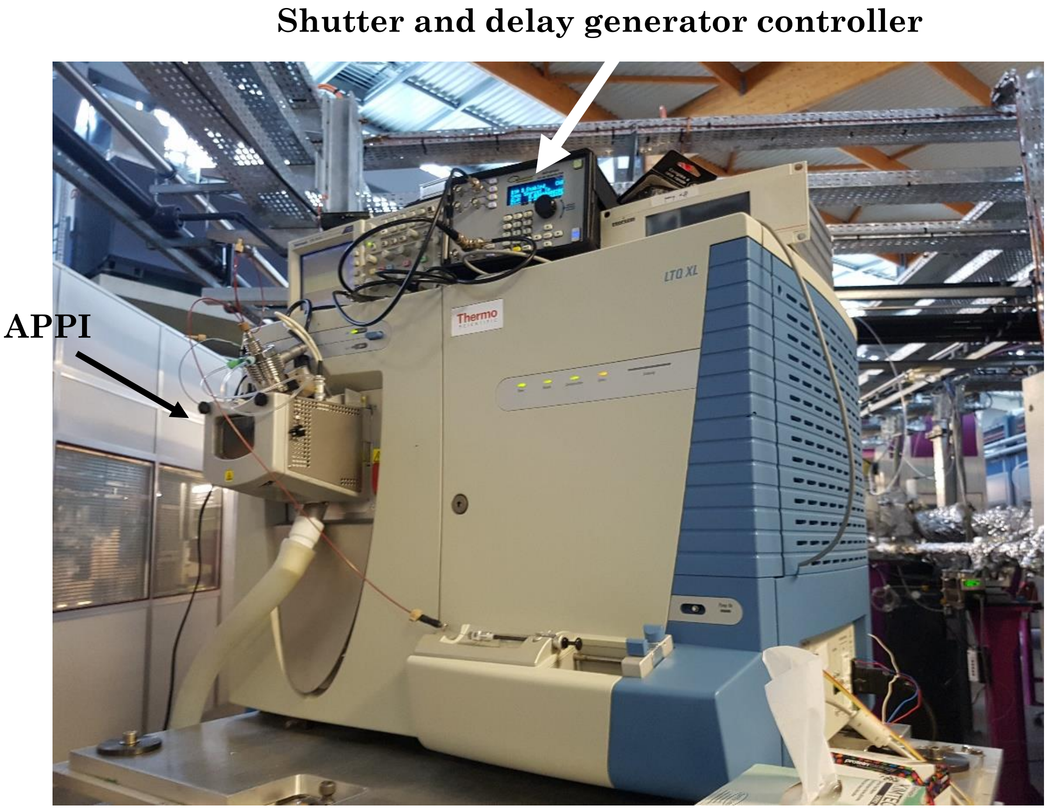

Figure 2-13 Photograph of the LTQ ion trap setup at DESIRS/SOLEIL. The PAH solution is injected from the needle (bottom right) towards the APPI source. The shutter controller can be seen on top of the instrument.

2.8 Imaging PhotoElectron PhotoIon Coincidence (iPEPICO) setup at SLS

2.8.1 The VUV beamline at SLS

The SLS synchrotron facility has a 288 meter circumference storage ring in which electrons are accelerated up to 2.4 GeV, providing radiation to 14 beamlines. For the experimental results presented in this manuscript the VUV beamline was used. The bending magnet radiation is focused into a gas filter after passing by two collimating mirrors and a grazing incidence monochromator (600 mm^{-1} line density is used to access 5 – 15 eV and 1200 mm^{-1} to access 15 – 30 eV energies (Johnson et al. (2009))). The available flux is 10^{11}–10^{12} photons s^{-1} in the 5–20 eV energy range. The horizontal exit slit (100 µm/mm) is located at the focus in the gas filter, 26 m away from the source. Depending on the photon energy, a MgF_2 window (5–10 eV), 10 mbar of Ne (11–21 eV) or a Ne/Ar/Kr mixture (7–14 eV) is used to suppress higher harmonic radiation. A schematic design can be found in Figure 2-14. One of the endstations corresponds to the iPEPICO instrument, explained in the following section, used in the experiments presented in this thesis.

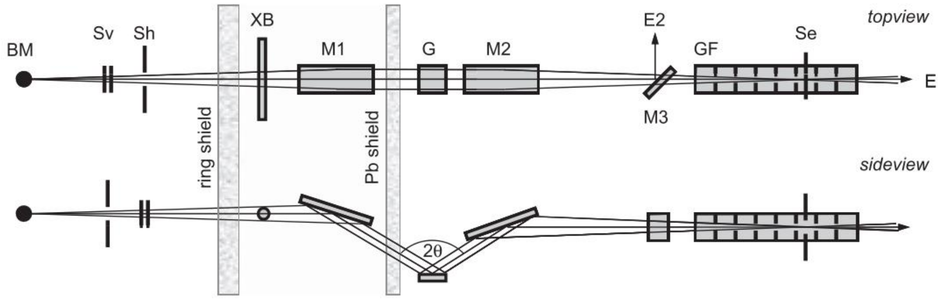

Figure 2-14 VUV beamline layout at SLS (not to scale). BM: beam magnet, (Sv, Sh): vertical and horizontal slits, XB: X-ray blocker, M1: collimating mirror, G: grating, M2: refocusing mirror, M3: flip mirror, GF: gas filter, Se: exit slit, E1, E2: endstations 1 and 2. ***Taken from Johnson et al. (2009).***

2.8.2 iPEPICO technique and experimental setup

IPEPICO uses a combination of photoionization mass spectrometry and photoelectron spectroscopy in order to study unimolecular dissociation dynamics of ions as a function of their internal energy (Bodi et al. (2009); Johnson et al. (2009); Osborn et al. (2016)).

First, a gas sample of neutral molecules is injected into the source chamber where it is exposed to vacuum ultraviolet photons (VUV) from a synchrotron source. These photons are selected to have enough energy to ionize the molecules, so for each molecule a photoion and a photoelectron will be formed. These resultant charged particles are accelerated in opposite directions under a continuous electric field. The final positions and arrival times in each detector are stamped.

When the incident photon has a higher energy than that strictly needed to ionize the molecule, this excess will be split between the kinetic energy of the electron, the kinetic energy of the ion, and the internal energy that the ion has acquired, as described in Equation 2-9.

Equation 2-9

$$E_{neutral}^{internal} + h\nu \rightarrow E_{ion}^{internal} + E_{ionization} + K_{ion} + K_{e^-}$$

where hv is the ionizing photon energy, $E_{ion}^{internal}$ is the internal energy of the ion, $E_{ionization}$ is the adiabatic ionization energy, K_{ion} is the kinetic energy of the ion and K_{e^-} is that of the electron. Because of the conservation of momentum, the kinetic energy of the ion can be neglected. Knowing the photon energy and the adiabatic ionization energy, the only way to estimate accurately the internal energy of the ion is by selecting threshold electrons, *i.e.*, ejected electrons having zero kinetic energy. These electrons will collide with the center of the detector, making them easily distinguishable. Thus, the energy that remains after the ionization corresponds to the internal energy.

Electron times-of-flight are three orders of magnitude faster than ion ones due to their lower mass. This means that the electron detection can be used as a timestamp for the ionization event, starting the clock for the ion time-of-flight analysis. As each fragment ion arrives at the detector, their arrival time is recorded, acting as the ‘stop’ signal. The time delay between the arrival of the electron at the imaging target and the detection of the fragment gives the flight time for the fragment. Only fragments measured in coincidence with the threshold electrons are analyzed; the remaining signals are discarded.

The results reported in this thesis (Chapter 6) were obtained with the iPEPICO experimental setup available in SLS (Figure 2-15). A detailed description can be found in Bodi et al. (2009); Johnson et al. (2009); Sztáray et al. (2010). Briefly, after introducing the neutral samples into the chamber, the ions are produced following the absorption of synchrotron VUV radiation. They are accelerated by an electric field of strength, U, controlled by the user and their mass to charge ratio is obtained ($\frac{m}{z} = \frac{2U}{v^2}$). On the other hand, ejected photoelectrons are detected by an imaging multichannel plate (MCP) in the opposite direction. This MCP focuses ions with the same velocity to a single spot on the detector, so the obtained image presents a radial spatial distribution as a function of their kinetic energy of the photoelectrons. This means that threshold electrons will be focused onto the center of the MCP, as mentioned before. From the recorded TOF distribution we will subtract the mass spectrum corresponding to the hot electron background, *i.e.,* the non-zero kinetic energy electrons that are detected in a small ring region around the center, in order to obtain the threshold ionization mass spectra (Sztáray & Baer (2003)).

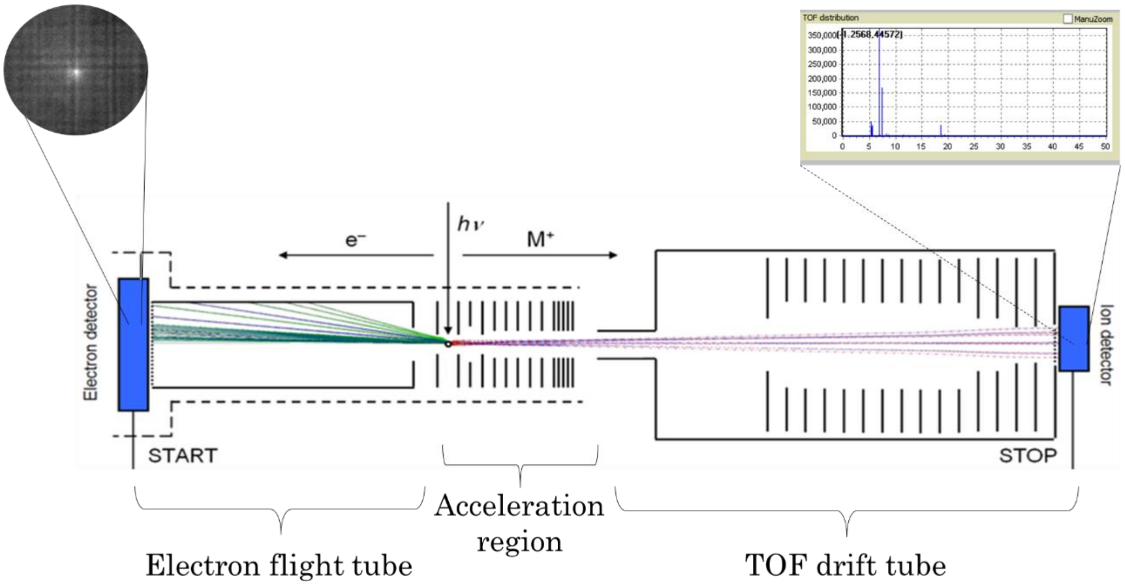
TOF distribution
ManuZoom
(-1.2568,44572)
350,000
300,000
250,000
200,000
150,000
100,000
50,000
0
0
5
10
15
20
25
30
35
40
45
50
hν
e⁻
M⁺
Electron detector
Ion detector
START
STOP
Acceleration region
Electron flight tube
TOF drift tube

Figure 2-15 Scheme of iPEPICO setup, where the electrons are accelerated through the electron flight tube before being detected, and the ions are accelerated in the opposite direction and reach the TOF detector at a time t, measured.

2.8.3 Principles of data modelling

The TOF distribution of the fragment ion peaks carries the unimolecular rate information which can be extracted thanks to a computer program developed by Sztáray et al. (2010). In a few words, it calculates the thermal energy distribution of the neutral molecule at a specific temperature (293 K typically) following a Boltzmann distribution: $P(E) = \frac{\rho(E)\, e^{-E/k_B T}}{\int_0^\infty \rho(E) e^{-E/k_B T}}$. Assuming that the internal energy distribution of the neutral molecule is directly transposed onto the ground electronic state of the ion upon threshold dissociation, we can obtain the internal energy distribution of the molecular ion as a function of the photon energy (from the density of states using the microcanonical formalism). Photon energies are converted into ion internal energies after subtraction of the ionization energy of each molecule. As an input to the program, we must provide the vibrational frequencies of the neutral molecule, the ion, and their rotational degrees of freedom. These values can be externally computed through DFT, for example. Additionally, the vibrational states of the transition states must be included, which are approximated by eliminating the appropriate mode of the expected reaction coordinate from the vibrational frequencies of the precursor ion. Moreover, the lowest frequencies are modified in order to adjust the entropy of activation, which translates in a more accurate fitting. The inputs include also the geometry of the setup and the applied potential, needed to determine the TOF.

For example, for the loss of a single hydrogen from the precursor ion, a frequency corresponding to a C-H bond stretch is removed, and five modes with the lowest frequencies are scaled up (or down). Once the density and number of states are calculated, RRKM theory (explained in detail in Chapter 3) is applied to calculate dissociation rates. One of the advantages of this program is that parallel or consecutive dissociation paths can be unraveled in order to reproduce the experimental TOF distributions. These dissociation rates, together with the energy distributions, will allow us to calculate the breakdown diagrams. We then compare these calculated breakdown diagrams with the experimental ones, and modify specific model parameters until the best fit is obtained and convergence is reached. An example of a unimolecular breakdown diagram obtained in SLS by West et al. (2014c) can be seen in Figure 2-16.

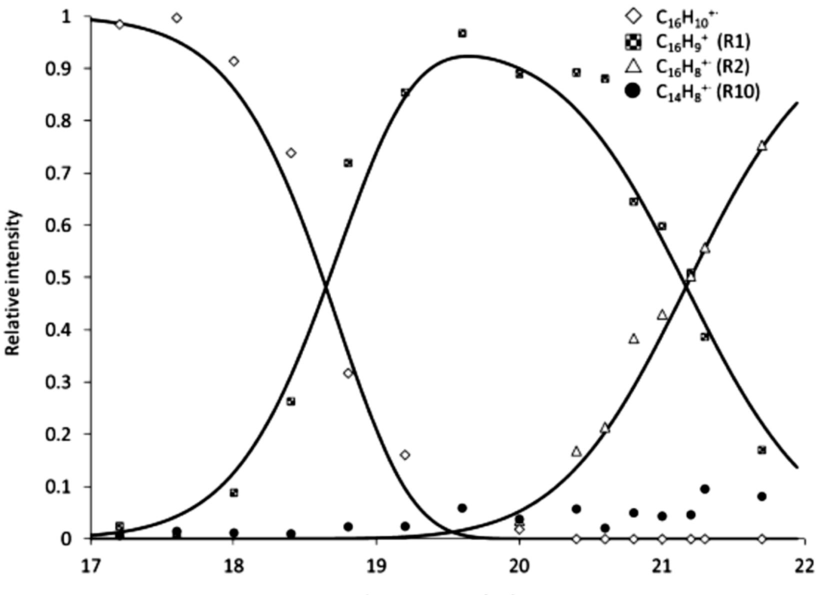

Figure 2-16 Example of unimolecular breakdown diagram for pyrene radical cation ($C_{16}H_{10}^+$). The curves correspond to the parent and to the dehydrogenated daughter ions ($C_{16}H_9^+$ anc $C_{16}H_8^+$). ***Figure taken from West et al. (2014c).***

Chapter 3: THEORETICAL MODELLING

I'M DONE WITH
~~EXPERIMENTS.~~
CALCULATIONS
WELL, THERE'S ONE MORE.
BUT THEN I'LL BE DONE.
THE LAST THREE YEARS OF YOUR PH.D.
JORGE CHAM © 2016
PHDCOMICS.COM

3.1 Introduction 48

3.2 Electronic structure 48

3.2.1 The Schrödinger equation ________ 48

3.2.2 Density Functional Theory (DFT) ________ 52

3.2.3 Density Functional Tight Binding (DFTB) ________ 55

3.3 Exploration of potential energy surface (PES) 56

3.3.1 Structural optimization ________ 56

3.3.2 Molecular Dynamics (MD) ________ 57

3.4 Statistical calculations: RRKM 58

3.1 Introduction

Experiments by themselves are hardly ever enough to fully understand and predict the physical chemistry of molecular ions, and here is where theoretical modelling proves to be useful. In this thesis, we used quantum chemistry and molecular dynamics to rationalize the experimental results and obtain complementary information. The synergy between experiments and theory also allows for cross benchmarking of the two approaches.

In this chapter, I will present the theoretical methods I used for my thesis, that is to say:

- Electronic structure calculation, focusing on Density Functional Theory (DFT) methods, adapted to treat the systems studied in this thesis.
- Methods to explore potential energy surfaces (PES)
- Molecular Dynamics (MD)
- Rice–Ramsperger–Kassel–Marcus (RRKM) theory

Due to the size and nature of the molecules explored in this thesis, we have used DFT methods to investigate some of the most relevant dissociation pathways that we observed in the experiments. These static studies were complemented with MD simulations using an approximate DFT scheme, the Density Functional based Tight Binding (DFTB) potential. Finally, RRKM modeling was used to obtain dissociation rates of unimolecular reactions studied in the iPEPICO experiments.

3.2 Electronic structure

3.2.1 The Schrödinger equation

The knowledge of a quantum system is based on solving the Schrödinger equation, which describes the physical evolution of the wavefunction of the all the particles within a system. Its most general form, the time-dependent equation (Equation 3-1) is written as follows (assuming a system with N electrons and M nuclei):

Equation 3-1 Time-dependent Schrödinger equation

$$i\,\hbar\,\frac{\partial}{\partial t}\Psi(\boldsymbol{r_1}\,\dots,\boldsymbol{r_n},\boldsymbol{R_1},\dots,\boldsymbol{R_M},\,t) = \hat{H}\,\Psi(\boldsymbol{r_1}\,\dots,\boldsymbol{r_n},\boldsymbol{R_1},\dots,\boldsymbol{R_M},\,t)$$

where

- Ψ is the wave function of the quantum system, which is related with the probability of finding a specific particle at a certain position
- $\boldsymbol{r_i}$ and $\boldsymbol{R_J}$ are vectors representing the positions of each electron and nuclei respectively
- $\hat{H}$ is the Hamiltonian operator, accounting for the total energy of the system
- $\hbar$ is the Plank constant ($\hbar = h/2\pi$) and t is the time

Solving this equation implies finding the allowed energy levels of the mechanical system, and obtaining the associated wavefunction. An exact solution for the Schrödinger equation has only been obtained so far for the hydrogen atom. For atoms with more than one electron, approximations must be made. The degree of approximation depends on the complexity and the size of the system.

Briefly, the Hamiltonian includes the kinetic and all potential energy contributions to the particle. Assuming that the Hamiltonian does not depend explicitly on time, atomic or molecular orbitals can be described as the stationary states of the time-independent Schrödinger equation. For non-relativistic particles in the absence of a magnetic field, this equation is written as:

Equation 3-2 Time independent Schrödinger equation

$$\hat{H}\,\Psi(\boldsymbol{r_i},\,\boldsymbol{R_J}) = E_{tot}\Psi(\boldsymbol{r_i},\,\boldsymbol{R_J})$$

where $\hat{H}$ includes all the contributions to the total energy: Kinetic energies of the N electrons (T_e), kinetic energies of the M nuclei (T_N), electrostatic – attractive – interaction between nuclei and electrons (V_{Ne}), and repulsive potential due to electron-electron (Vee) and nucleus-nucleus (V_{NN}) interactions. These terms can be represented as:

Equation 3-3

$$\hat{H} = -\frac{1}{2}\sum_{i=1}^{N}\nabla_i^2 - \frac{1}{2}\sum_{J=1}^{M}\frac{1}{M_J}\nabla_J^2 - \frac{1}{2}\sum_{i=1}^{N}\sum_{J=1}^{M}\frac{Z_J}{r_{iJ}} + \sum_{i=1}^{N}\sum_{j>i}^{N}\frac{1}{r_{ij}} + \sum_{J=1}^{M}\sum_{K>J}^{M}\frac{Z_J Z_K}{R_{JK}}$$

$$= \hat{T_e} + \widehat{T_N} + \widehat{V_{Ne}} + \widehat{V_{ee}} + \widehat{V_{NN}}$$

The Born-Oppenheimer approximation (Born & Oppenheimer (1927)) assumes that that the motion of the nuclei is negligible compared to that of the electrons, because the first are three orders of magnitude heavier than the latter. Most electronic structure calculations of molecular systems are carried out within this approximation. This allows us to consider that the electrons are moving in the field of the frozen nuclei that have zero velocity and constant nucleus-nucleus potential repulsion energy (R_{JK} constant). Under this approximation, we can separate the nuclear (T_N and V_{NN}) and the electronic contributions to the Hamiltonian, and treat them independently. The expression of the electronic Hamiltonian is (Equation 3-4):

Equation 3-4

$$\hat{H}_{elec} = -\frac{1}{2}\sum_{i=1}^{N}\nabla_i^2 - \frac{1}{2}\sum_{i=1}^{N}\sum_{J=1}^{M}\frac{Z_J}{r_{iJ}} + \sum_{i=1}^{N}\sum_{j>i}^{N}\frac{1}{r_{ij}} = \hat{T_e} + \widehat{V_{Ne}} + \widehat{V_{ee}}$$

Solving the electronic problem amounts, then, to solving the electronic Schrödinger equation:

Equation 3-5

$$\hat{H}_{elec}\,\Psi_{\mathrm{elec}}(\boldsymbol{r_i}) = E_{elec}\,\Psi_{\mathrm{elec}}(r_i)$$

The solution will be the electronic wavefunction (Ψ_{elec}) – which depends on the electron coordinates and spin – and the electronic energy (E_{elec}) which, added to the constant nuclear repulsion term we had obviated, gives us the total energy ($E_{Tot} = E_{elec} + E_{nucl}$). The electronic wavefunction depends on 3N coordinates and N spin functions (N being the number of electrons).

The most widely known family of wavefunction methods are based on the Hartree-Fock (HF) approximation, which considers that the total wavefunction is a product of N one-electron independent wavefunctions presented in the form of a Slater determinant. However, this method, which considers that one electron is in the mean field of the others, does not include the description of electronic correlation. A variety of approaches called post Hartree-Fock methods, describe the electronic correlation at different levels. We can cite perturbational methods such as MP2, coupled-cluster methods such as CCSD, multireference methods such as CASSCF etc. More information can be found in Szabo & Ostlund (1982).

The electron occupation in space can be represented by a molecular orbital which, in turn, can be expressed as a linear combination of atomic orbitals (LCAO approximation) (Equation 3-6):

Equation 3-6

$$\Psi_j = \sum_{i=1}^{n} c_{ij}\,\Phi_i$$

where Ψ_j represents the electronic state (j), c_{ij} represents the weighting coefficients and $\{\Phi_i\}$ the atomic orbitals. These basis functions can be expressed as Slater type orbitals (STOs) or, more commonly, as atom-centered Gaussian orbitals (GTOs) in the form:

Equation 3-7

$$\phi_{\zeta,l_x,l_y,l_z}(x,y,z) = N\, x^{l_x} y^{l_y} z^{l_z}\, e^{-\zeta r^2}$$

where N is a normalization factor, l_x, l_y, l_zdetermine the type of orbital and zeta (ζ) is a parameter that determines the width of the orbital (small ζ gives a diffuse function). The main advantage of using GTOs is the fact that the product of two GTOs on different centers is equal to a single other GTO at center r' between the original center.

For the systems studied in this thesis and the type of data needed, HF approaches become too computationally costly due to the many electronic structure calculations involved, and DFT-based approaches become a more suitable option. In the following section, I present these DFT approaches, which are used in the majority of calculations regarding PAHs in their ground electronic state.

3.2.2 Density Functional Theory (DFT)

DFT is a cost-effective alternative to the wavefunction methods in order to determine the ground state charge density and electronic structure of a system. Its success resides in the use of a functional of the electron density, $\rho(\mathbf{r})$, through which the number of degrees of freedom of the N-body system decreases significantly – from 3N to only the three spatial coordinates of the particle density. This electron density is a measurable observable, described as the probability of finding any of the N electrons with an arbitrary spin (s) within a volume element $d\boldsymbol{x}_1$ while the remaining N- electrons have arbitrary positions and spin. It is mathematically described as:

Equation 3-8

$$\rho(\boldsymbol{r}) = N \int \dots \int |\Psi(\mathbf{x_1}, \mathbf{x_2}, \dots, \mathbf{x_N})|^2 \, ds_1 d\boldsymbol{x}_2 \dots . d\boldsymbol{x}_N$$

The basis of DFT resides in the Hohenberg-Kohn theorems (Hohenberg & Kohn (1964)), which declare that we can obtain the ground state, and thus the electronic structure of a system through its electronic density.

- Theorem I, principle of existence: For any system of interacting particles in an external potential $V_{ext}(\mathbf{r})$, the ground state particle density $\rho_0(\boldsymbol{r})$ is uniquely determined. This implies that there exists a universal functional $E[\rho(\boldsymbol{r})]$ linking the ground-state energy E_0 of the system and its density ρ_0, and it is valid for any external potential $V_{ext}(\mathbf{r})$. All the electronic properties of the ground state can be determined if the electronic density is known.

- Theorem II, variational principle: The exact ground state energy and density of a system is the one that minimizes the energy functional $E[\rho(\boldsymbol{r})]$. This minimal energy corresponds to the exact electronic density of the system in its ground state.

From these theorems[4], one can write the energy of the system as a sum over the kinetic energy of the electrons $T[\rho(\boldsymbol{r})]$, of the electron-electron interaction $E_{ee}[\rho(\boldsymbol{r})]$, and of the Culomb interactions between electrons and nuclei:

Equation 3-9

$$E[\rho(\boldsymbol{r})] = T[\rho(\boldsymbol{r})] + E_{ee}[\rho(\boldsymbol{r})] + \int V_{Ne}(\boldsymbol{r})\rho(\boldsymbol{r})\, d\boldsymbol{r},$$

The goal is to minimize this energy functional, but the challenge resides in that the expressions of $T[\rho(\boldsymbol{r})]$ and $E_{ee}[\rho(\boldsymbol{r})]$ are not known for a system of particles in interaction. Kohn and Sham introduced the idea of non-interacting reference orbitals (KS orbitals), through an effective potential $V_s(\mathbf{r})$ such that the KS density is the same as the ground state density of our real target system $\rho_s = \rho_0$. They simplified the energy functional $E[\rho(\boldsymbol{r})]$ by including an exchange correlation functional, $E_{XC}\,[\rho(\boldsymbol{r})]$, that allows to make the link between the real system and the imaginary one (non-interacting electrons). $E_{XC}\,[\rho(\boldsymbol{r})]$ contains all the unknown terms: self-interaction correction, exchange and correlations, and a residual part of the kinetic energy that is not covered by the kinetic energy of the non-interacting system (Ts):

Equation 3-10

$$E_{XC}\,[\rho(\boldsymbol{r})] = (T[\rho(\boldsymbol{r})] - T_s[\rho(\boldsymbol{r})]) + (E_{ee}[\rho(\boldsymbol{r})] - J[\rho(\boldsymbol{r})])$$

with $J[\rho(\boldsymbol{r})] = \frac{1}{2}\int\int \frac{\rho(r)\rho(\boldsymbol{r}')}{|\boldsymbol{r}-\boldsymbol{r}'|}$

Therefore, under the Kohn-Sham approach, the DFT electronic energy is given as a function of the electron density:

Equation 3-11

$$E_{KS-DFT}\,[\rho(\boldsymbol{r})] = T_S[\rho(\boldsymbol{r})] + E_{Ne}[\rho(\boldsymbol{r})] + J[\rho(\boldsymbol{r})] + E_{XC}[\rho(\boldsymbol{r})]$$

where $T_S[\rho(\boldsymbol{r})]$ is the kinetic energy of the non-interacting electrons, $E_{Ne}[\rho(\boldsymbol{r})]$ is the electron-nucleus interaction energy, $J[\rho(\boldsymbol{r})]$ is the classical

---

[4] A thorough explanation of DFT is not the aim of this thesis; a demonstration of these theorems, along with a more exhaustive explanation of DFT can be found in Koch & Holthausen (2001).

Coulomb interaction term and $E_{xc}[\rho(\boldsymbol{r})]$ is the exchange correlation functional, whose exact expression in unknown.

There are various DFT approximations on the exchange-correlation functional. A first approximation is the so-called local density approximation (LDA) based on the description of the electron gas (Ceperley & Alder (1980); Perdew & Zunger (1981)). This approximation is not correct for molecular systems whose density varies in space. For this reason, $E_{XC}\,[\rho(\boldsymbol{r})]$ was expressed as a function of density but also of the gradient of the charge density, accounting for the non-homogeneity of the true electron density; this is the so-called generalized gradient approximation (GGA). Several GGA functionals exist, popular ones being PW91 (Perdew (1991); Perdew et al. (1998)) or PBE (Perdew et al. (1996)). A class of functionals called hybrid functionals was first proposed by Becke in 1993 (Becke (1993a), (1993b)). The idea was to add a Hartree-Fock contribution to the exchange because, for a non-correlated system, the HF energy is exact whereas for a correlated system, a GGA energy is more appropriate. Different approaches exist to build hybrid exchange correlation functionals, and they can be distinguished by the number of adjustable parameters (Becke (1993a), (1993b), (1996)):

Equation 3-12

$$E_{XC}[\rho(\boldsymbol{r})] = E_{XC}^{LDA}[\rho(\boldsymbol{r})] + a_0(E_{HF}^{x} - E_{LDA}^{x}) + a_x E_{GGA}^{x} + a_c E_{GGA}^{x}$$

Amongst the most used hybrid functionals we find the B3LYP functional, which has been used in the context of this thesis. It is based on the exchange and correlation corrections from Becke (B) and Lee, Yang and Parr (LYP) (Lee et al. (1988)). The parameters a_0, a_x and a_c are determined so as to reproduce a set of properties for a set of molecules as wide as possible.

The auxiliary DFT wavefunctions are also described in the LCAO formalism. In the work presented in this thesis we have used the popular 6-31G(d,p) basis set, which assumes two basis functions for each atomic orbital (double-zeta type basis) and accounts for the orbital shape distortion (polarization) due to the influence of other atoms.

3.2.3 Density Functional Tight Binding (DFTB)

In this work, molecular dynamic simulations have also been performed, which require millions of single point energy calculations and gradients. The DFT approach is not efficient or fast enough, and therefore we used an approximate DFT scheme: the DFTB method (Porezag et al. (1995); Seifert et al. (1996)) in its self-consistent charge version (SCC-) (Elstner et al. (1998)). In SCC-DFTB, only the valence electrons are treated explicitly and the Hamiltonian is obtained from a Taylor expansion at the second order around a reference KS density of the energy functional:

Equation 3-13

$$E[\rho_0 + \delta\rho] = E[\rho_0] + \int \frac{\partial E}{\partial \rho}|_{\rho_0}\, \delta\rho\, d\boldsymbol{r} + \frac{1}{2}\iint \frac{\partial^2 E}{\partial\rho\partial\rho'}\, \delta\rho(\boldsymbol{r})\delta\rho'(\boldsymbol{r}')d\boldsymbol{r}\, d\boldsymbol{r}'$$

This means that the electron density that minimizes the energy, $\rho(\boldsymbol{r})$, is composed by a reference density $\rho_0(\boldsymbol{r})$ plus a perturbation due to energy fluctuation $\delta\rho(\boldsymbol{r})$. The final energy $E^{SCC-DFTB}\,[\rho_0 + \delta\rho]$ includes a repulsive contribution depending on the reference density ρ_0, a term corresponding to the band energy, and second order terms of the expansion, E^{2nd}:

Equation 3-14

$$E^{SCC-DFTB}\,[\rho_0 + \delta\rho] = V^{rep}[\rho_0] + \sum_i \rho_i < \Psi_i \big| \hat{H}(\rho_0) \big| \Psi_i > \; + E^{2nd}$$

with $i : \rho_0, \{\alpha\beta\}\, atoms$ and where $E^{2nd} = \frac{1}{2}\sum_{\alpha\beta} \gamma_{\alpha\beta}\, q_\alpha q_\beta$ is a function of Mulliken charges (the difference between the atomic Mulliken population (Mulliken (1955)) and the number of valence electrons of the neutral free atom), and α, β run either on atoms or on atomic orbitals. This method allows for a much lower computational cost because integrals are pre-calculated, a minimal valence basis set is used, and three center terms (integrals involving more than two centers) are neglected. All SCC-DFTB calculations achieved in this thesis were performed with the deMonNano code, a code hosted and developed at LCPQ (http://demon-nano.ups-tlse.fr/)). Detailed reviews on DFTB can be found in Oliveira et al. (2009), Koskinen & Mäkinen (2009) and Rapacioli et al. (2012).

3.3 Exploration of potential energy surface (PES)

3.3.1 Structural optimization

Once the electronic energy is calculated for all the atoms, a PES can be drafted (see Chapter 2 of Lewars (2011) for a detailed explanation) which describes the energy of the system as a function of the positions of the atoms. Following the lowest energy path, the optimized geometry of the molecule can be reached. The most interesting points on PES are those where the first derivatives with respect to the internal coordinates are zero, because they represent stationary points, *i.e.*, stable or quasi-stable species (reactants, products and intermediates). If the second derivative along all the directions is positive, one will have found a local minimum, while a transition state will be represented by one negative value of the second derivative, along the reaction coordinate (Figure 3-1).

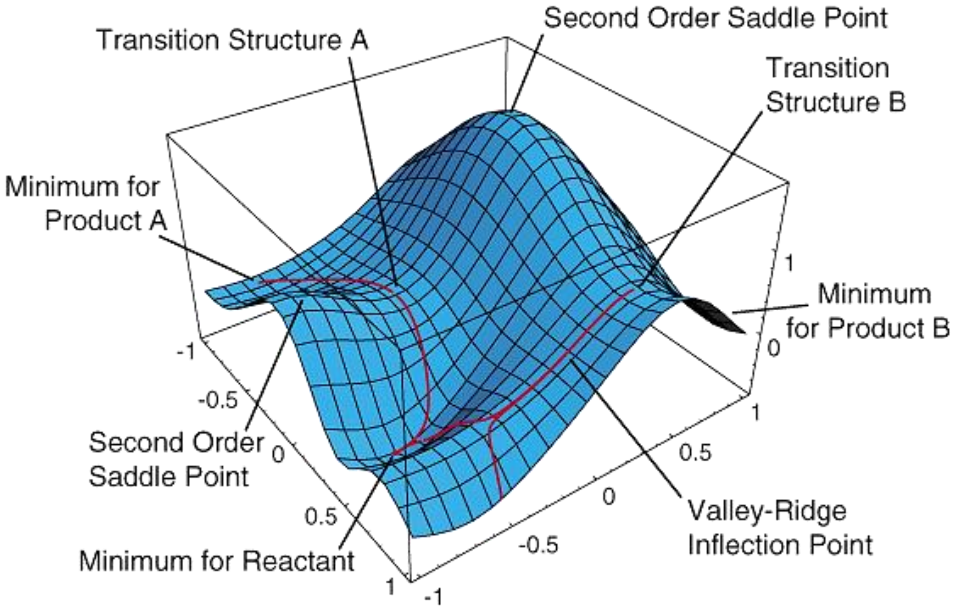

Figure 3-1. An example of a PES. The initial products A and B will follow the least energetic paths, represented by red lines, to reach the final reactant point. Saddle points and transition structures are presented, where the local curvatures reach a maximum. *Image taken from (http://www.chem.wayne.edu/~hbs/chm6440/PES.html).*

A geometry optimization will be carried out by starting with a meaningful input structure and allowing the molecule to explore different geometrical configurations until a minimum has been found. A search must be done to confirm this minimum is, indeed, a global minimum.

The local geometry optimizations presented in these thesis have been performed using the B3LYP functional with the 6-31G(d,p) basis set using the Gaussian09 Package Frisch (2013). These were complemented by full harmonic frequency calculations by diagonalizing the Hessian matrix at this level. Frequency calculations were used to characterize each stationary geometry as a minimum or a saddle point of first order and to obtain the zero-point vibrational energies (ZPEs). Transition states (TS) were optimized using the interpolation methods implemented in the Gaussian09 suit of programs. The Berny algorithm was used for most elementary steps. We used in a few cases the Synchronous Transit-Guided Quasi-Newton (STQN) algorithm and in litigious cases, the initial TS search was complemented with the Intrinsic Reaction Coordinate (IRC) procedure to confirm the reaction path. Finally, we also obtained the rotational constants, corresponding to the three primary moments of inertia of the molecule, which will be used as an input in the RRKM calculations described in the end of this chapter.

3.3.2 Molecular Dynamics (MD)

MD simulations with classical nuclei and quantum electrons described at the SCC-DFTB level were achieved. The procedure used in this thesis is explained in Simon et al. (2017), and is briefly reminded hereafter: All simulations are performed in the microcanonical ensemble within the Born–Oppenheimer MD scheme, computing the potential energy on-the-fly. The nuclei obey the classical equations of motion, integrated with the velocity Verlet algorithm using a timestep of 0.1 fs so as to ensure a constant total energy (deviation less than 0.5 % of the initial kinetic energy), except in the particular case of constrained density functional tight binding (DFTB). Initially, the kinetic (vibrational) energy is spread randomly over all the atoms of the molecular system, with fast statistical redistribution over all vibrational modes. Besides, we specify that such MD are achieved on the ground state potential energy surface. This can be justified assuming a fast internal conversion (less than a hundred of fs), which is probably reasonable in the case of PAH due to the presence of conical intersection (Hall et al. (2006)).

We used a Fermi distribution (Fermi temperature of 1500 K) to determine the molecular orbital occupations. It avoids oscillation problems during the search for a self-consistent solution, often arising when computing DFTB energy for dissociated or close to dissociation systems, and allows the recovery of continuity in energy and gradients in the case of level crossing. For a given PAH$^+$ and for a given energy, we typically perform 100 trajectories of several hundreds of picoseconds, up to 1 ns. From such extensive simulations, we can derive branching ratios and kinetic data. This approach has been benchmarked for a series of PAH radical cations (Simon et al 2017). Such simulations can also be used in a less extensive manner to provide insight into reaction mechanisms (Jusko et al. (2018)).

3.4 Statistical calculations: RRKM

Dissociation rates of unimolecular reactions can be derived from the iPEPICO experiments described in Chapter 2 based on the Rice–Ramsperger–Kassel–Marcus (RRKM) theory (Rice & Ramsperger (1927), (1928); Kassel (1928)). They proposed that the rates of such reactions are not dependent on the activation mechanism, but only on the vibrational modes of the excited molecule (A*). Assuming that the molecule is formed by a set of identical harmonic oscillators, only one in particular is associated with the reaction coordinate (the critical oscillator). Assuming also that all the energy is freely distributed amongst all the vibrational modes, the excited molecule must go through a transition state (A‡) before ending up in the products (P) (Marcus (1952); Green (1992)). This transition state will be built statistically considering that any configuration in which the critical oscillator contains more energy that the bond energy will be associated to the transition state, and the remained configurations will be assigned to the molecule.

Equation 3-15

$$A^* \xrightarrow{k} A^\ddagger \rightarrow P$$

This theory assumes that the excitation energy randomizes rapidly compared to the reaction rate and is distributed statistically among the modes prior to the reaction, as had been confirmed by Oref & Rabinovitch (1979). Under this assumption, getting to the transition state will require that the energy stored in its vibrational modes will be enough to break the bonds at play. This theory is applicable to intramolecular processes, in which the collisional and radiative interactions with the environment are negligible during the time scale of interest (Uzer & Miller (1991)). The rate of this reaction is given by:

Equation 3-16

$$k(E) = \frac{\sigma N^{\ddagger}(E - E_0)}{h\, \rho(E)}$$

where

- σ is the degeneracy of the reaction, *i.e.*, the number of equivalent paths that lead to the same product
- $N^{\ddagger}(E - E_0)$ is the sum of the internal rotational-vibrational states of the transition state from 0 to (E-E_0), with E_0 being the 0 K activation energy.
- h is the Plank constant
- $\rho(E)$ is the parent ion density of states of at an internal energy E

$N^{\ddagger}(E - E_0)$ and $\rho(E)$ can be calculated based on the DFT calculated structures for the precursor, the vibrational frequencies and rotational constants through the direct count method (Beyer & Swinehart (1973)).

The obtained reaction rates will be useful to determine the 0K activation energy (E_0) and the entropy of activation (ΔS‡) from the experimental breakdown curves, as has been widely done in previous studies, for example Baer & Mayer (1997); West et al. (2012), (2014c).

Chapter 4: *STABILITY OF TWO DIBENZOPYRENE ISOMERS UNDER VUV RADIATION: LINEAR ION TRAP EXPERIMENTS*

I WANT YOU TO SUBMIT AN ABSTRACT TO A CONFERENCE THAT IS HAPPENING IN 7 MONTHS.
BUT, I HAVE NO IDEA WHAT KIND OF RESULTS I'LL HAVE IN 7 MONTHS!
DON'T WORRY.
THE TRICK IS TO MAKE IT AS VAGUE AND AS OPEN TO INTERPRETATION AS POSSIBLE. THE MORE AMBIGUOUS, THE BETTER.
JORGE CHAM © 2016
IS THAT WHY IT'S CALLED AN ABSTRACT?
IT'S AN ABSTRACT ART FORM.

WWW.PHDCOMICS.COM

4.1 Introduction 62
4.2 Experimental campaign 63
4.3 Evolution of action spectra with VUV photon energy 65
4.4 Ionization and fragmentation 70
4.5 Fragmentation pathways 71
4.6 Discussion 76

4.1 Introduction

As discussed in Chapter 1, it is paramount to obtain as much information as possible about the interaction of VUV photons with a wide range of PAH molecules, in particular dissociation rates and dissociation energy thresholds, in order to feed them into astronomical models.

Several experimental studies have explored the effect of size, hydrogenation state and structure on the stability of PAHs. Jochims et al. (1994) performed photoion mass spectrometry under synchrotron radiation on several PAHs of sizes between 10 and 24 carbon atoms. They reported that the loss of H was the lowest energy channel for all the studied PAHs, while only some of them, especially the smallest ones, were observed to lose H_2 and C_2H_2. They estimated the dissociation rate of their experimental conditions to be 10^4 s^{-1} and extrapolated their values to 10^2 s^{-1} to reach the astrophysical conditions in which dissociation is in competition with infrared cooling. In this pioneer experimental study on the PAH size effect on the dissociation energies, they concluded that larger PAHs are more resistant to UV photons. The effect of hydrogenation on the PAH stability has been addressed by Szczepanski et al. (2011) who concluded, through FT-ICR and DFT calculations, that small superhydrogenated PAHs have a tendency to dehydrogenate in the form of H_2. Additionally, Reitsma et al. (2014) confirmed the low binding energies for the additional hydrogen atoms on superhydrogenated coronene, and concluded that these molecules should be stable in the ISM, which differs from the results obtained from Gatchell et al. (2015) and Wolf et al. (2016) for pyrene. Finally, the specific effect of PAH structure has been subject to several studies, such as Ling & Lifshitz (1998) or Jochims et al. (1999). The first group studied two isomers of anthracene, obtaining an effect of the geometry on the C-H bond energies. The latter discusses the structural effects (such as the presence of a methyl group, H-H steric hindrance, isomers, etc.) and size-dependent effects on the photostability of a large number of PAHs by photoion mass spectrometry in the BESSY synchrotron.

In this work, we present the first study of VUV photo-fragmentation of two cation isomers of the dibenzopyrene molecule ($C_{24}H_{14}$) which contain the same number of carbons as coronene but have a less compact structure, presenting some areas with H-H hindrance, otherwise known as bay areas. Structures containing such areas have been shown to exhibit characteristic infrared signatures. One is located at shorter wavelength than the usual C-H stretch mode due to the steric interaction between the hydrogen atoms that are across bay regions (Bauschlicher et al. (2009)). Another one is located at 12.7 µm and is a good candidate to account for the band observed at this position in astrophysical spectra (Candian et al. (2014)). In addition, one of the studied isomers presents a non-planar structure (Figure 4-1), which is specific compared to previous studies mentioned above.

The samples of the isomers under study, dibenzo(a,e)pyrene and dibenzo(a,l)pyrene – referred to as AE and AL hereafter – were obtained from the PAH Research Institute in Greifenberg (Dr. Werner Schmidt). These two isomers contrast in structure, differing in the location of one of the benzene rings attached to the pyrene skeleton (see Figure 4-1). AE^+ presents a planar geometry, with an open structure while AL^+ is more compact, with a non-planar configuration due to the steric repulsion of two hydrogens located in adjacent benzene rings.

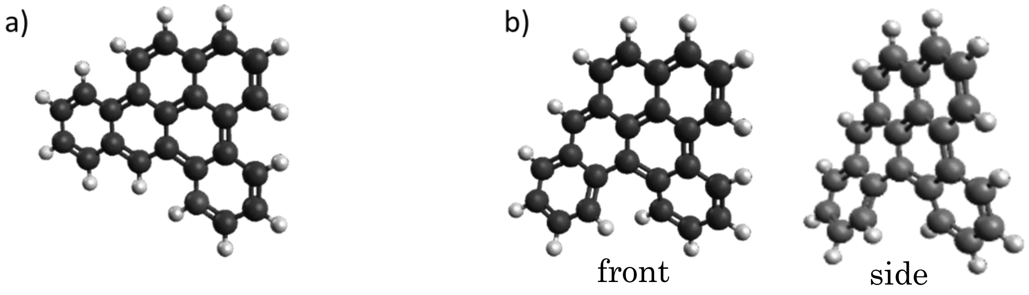

Figure 4-1. Schematic geometries of the dibenzo(a,e)pyrene isomer cations studied in this thesis. The planar isomer, AE^+, is shown in (a) and the non-planarity of AL^+ can be seen in (b).

4.2 Experimental campaign

To explore the impact of the structure on fragmentation and ionization we performed action spectroscopy experiments under VUV photons at SOLEIL (described in Chapter 2). The results presented in this chapter for the dibenzopyrene isomers belong to a campaign in which a set of 8 PAHs was studied. Conclusions obtained for the other PAHs can be found in Zhen et al. (2016b) and will be summarized in Chapter 7.

In these ion trap experiments, the samples were subjected to photons of energies between [7 –15.6 eV] with steps of 0.3 eV, and [15 – 20.0] eV with steps of 0.5 eV. The irradiation times corresponding to these two sets of data were 1 and 0.2 seconds respectively. Mass spectra of the resulting photo-products were recorded as a function of the incident photon energies, and were averaged around 150(400) times for low(high) energies. Blank spectra were recorded at each photon energy in similar conditions as the PAH signals, for both isomers, in order to subtract possible contaminant peaks also present in the background signal. The number of contaminant peaks typically increased with photon energy, so extreme care had to be taken in order to remove the actual background from the raw signal at each energy. The intensity of the peaks in the mass spectrum was then determined over the 3 sigma level. Additionally, in our experimental conditions the intensities of the photo-products are expected to scale linearly with the number of absorbed photons and therefore with the photon flux and irradiation time. We therefore corrected the data for the spectral response of the photon flux as well as for the relative irradiation time difference between the two scans (the low-energy part was scaled down to match the high-energy part in the overlapping range). The procedure for data treatment was not straightforward, and although an automatized method was developed to speed up the process, a careful analysis of each molecule at each energy value had to be done in order to confirm that the results were correct.

An example of the raw spectra of AE^+ at 15.5 eV incident photon energy (green) and the corresponding background signal (yellow) can be seen on Figure 4-2. The blue line shows the corrected spectra, showcasing the importance of the removal of the background in order to obtain proper analysis.

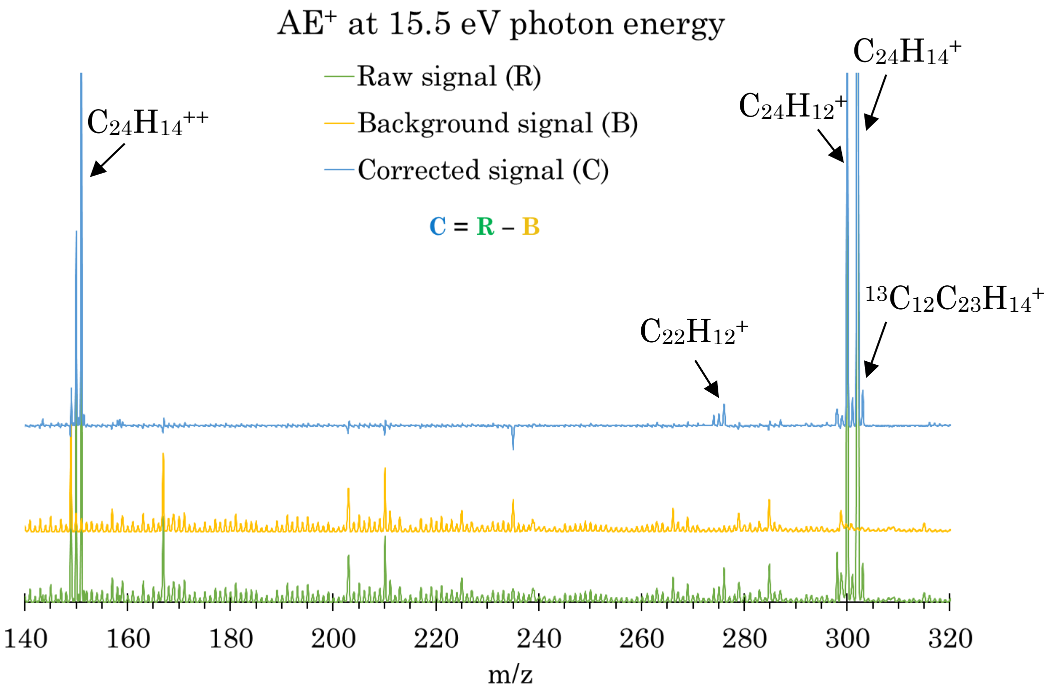

Figure 4-2 Example of a mass spectra obtained for AE⁺ after the absorption of 15.5 eV photons. The green line represents the raw ion signal, the yellow line represents the background ion signal and the final corrected signal can be seen in the blue line.

4.3 Evolution of action spectra with VUV photon energy

Three examples of processed spectra for each isomer can be seen in Figure 4-3, as a function of increasing incident photon energies. The evolution of peaks corresponding to the loss of a single H atom ($C_{24}H_{13}^{+}$), two hydrogens ($C_{24}H_{12}^{+}$), and small hydrocarbon (*e.g.* C_2H_2) can be clearly seen. In particular, at the lowest photon energy, the peak corresponding to H loss is minimal in AE⁺ (Figure 4-3 a)) while for AL⁺ we have already passed the threshold for this channel (Figure 4-3 b)). At 11.9 and 13.4 eV, we can see a clear peak attributed to the doubly ionized species ($C_{24}H_{14}^{++}$).

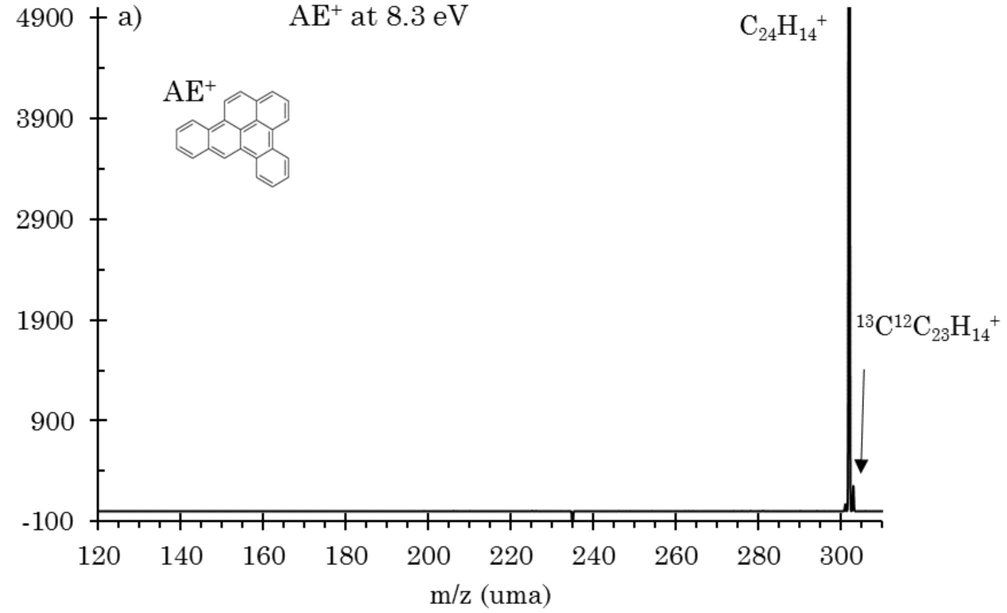
a)
AE$^+$ at 8.3 eV
AE$^+$
$C_{24}H_{14}^+$
$^{13}C^{12}C_{23}H_{14}^+$
4900
3900
2900
1900
900
-100
120
140
160
180
200
220
240
260
280
300
m/z (uma)

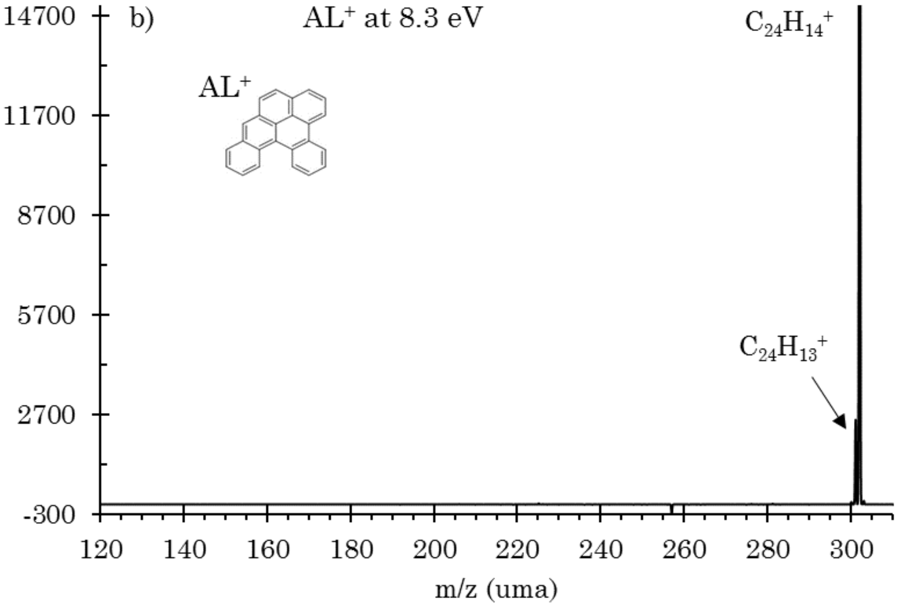
b)
AL$^+$ at 8.3 eV
AL$^+$
$C_{24}H_{14}^+$
$C_{24}H_{13}^+$
14700
11700
8700
5700
2700
-300
120
140
160
180
200
220
240
260
280
300
m/z (uma)

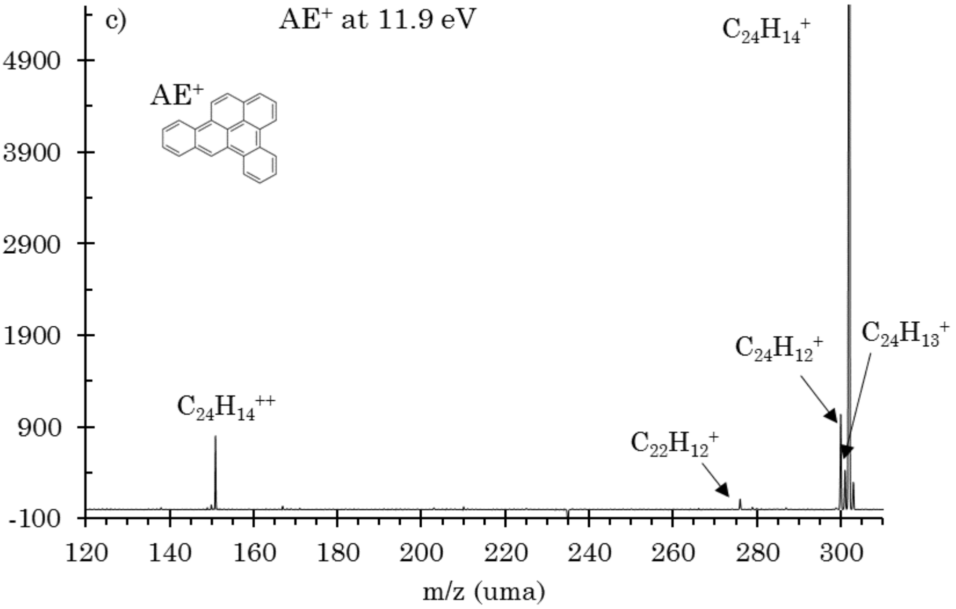
c)
AE+ at 11.9 eV
AE+
C24H14+
C24H12+
C24H13+
C24H14++
C22H12+
4900
3900
2900
1900
900
-100
120
140
160
180
200
220
240
260
280
300
m/z (uma)

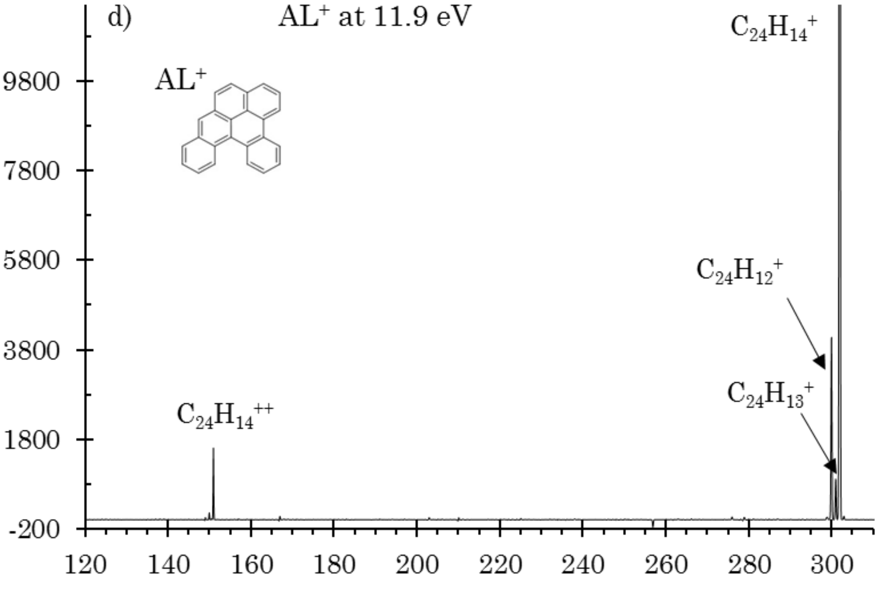
d)
AL+ at 11.9 eV
AL+
C24H14+
C24H12+
C24H13+
C24H14++
9800
7800
5800
3800
1800
-200
120
140
160
180
200
220
240
260
280
300
m/z (uma)

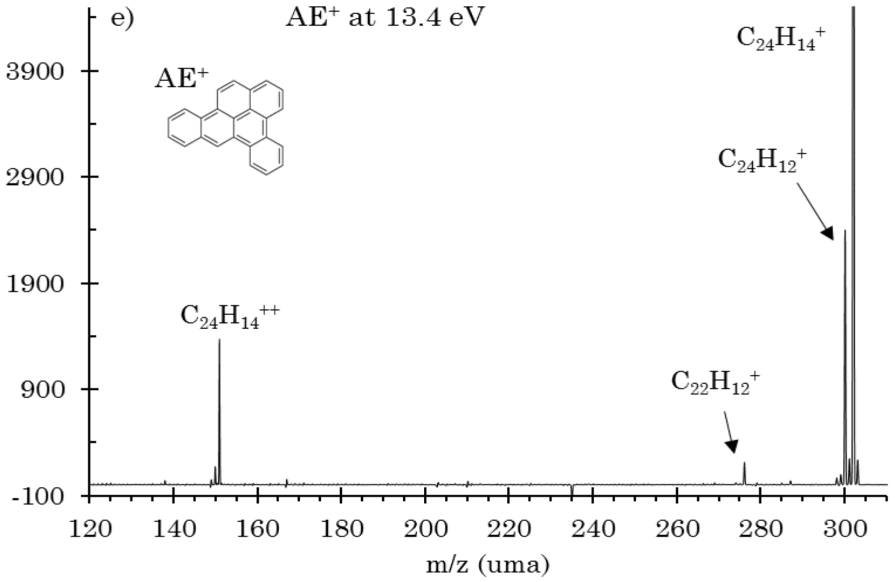

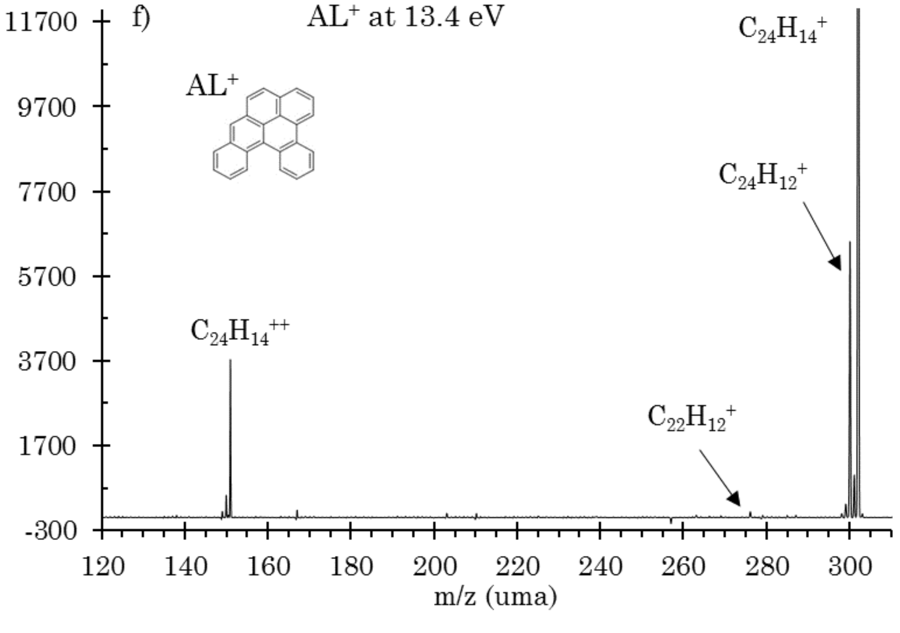

Figure 4-3. Mass spectra obtained with the LTQ mass spectrometer for AE⁺ and AL⁺ under different VUV irradiation energies (8.3, 11.9 and 13.4 eV). The parent is labelled as $C_{24}H_{14}^{+}$. $C_{24}H_{13}^{+}$ and $C_{24}H_{12}^{+}$ correspond to the loss of H and 2H/H_2 fragments, respectively. $C_{24}H_{14}^{++}$ corresponds to the ionization of the parents leading to doubly ionized species. The vertical axis represents the intensities of the corrected signal and it has been scaled in each case to 1/5 of the parent peak value.

Upon analyzing all the corrected spectra, the relative abundances of photo-fragments and photo-ionization products were obtained. These abundances are given in percentage of the event normalized over the total number of ions in the trap (parent plus photo-events). The corresponding errors are mainly associated with the removal of the background signal, and increase in intensity with photon energy due to increasing noise, while the total ion intensity decreases systematically. Another source of error is related with water contamination, and was only seen for AE^+ with peaks at m/z= 320, 319 and 318 a.m.u. These correspond to water-complexes related to the parent ions and their fragments after the loss of one and two hydrogens respectively. We added these contributions in our analysis to the corresponding bare species. Other experimental errors may be present but are more difficult to quantify. In general, experimental errors are minimized by the fact that the signal is averaged over a large number of shots.

From these photo-induced events we can obtain ionization and fragmentation yields, assuming that amongst all the possible independent relaxation processes taking place (*i.e.*, dissociation, radiative cooling and collisional relaxation with the He gas atoms in the trap) the last two could be negligible. This approximation is supported by the close overall correlation between the photo-absorption cross sections obtained theoretically by Malloci et al. (2004), (2007a), and the sum of all the events in our trap (fragments + doubly ionized) as reported in Zhen et al. (2016b) and illustrated in Figure 4-4. We can derive the photo-ionization yield as: $Y_{ion} = \frac{I_{double\ ionized}}{I_{fragments}+I_{double\ ionized}}$.

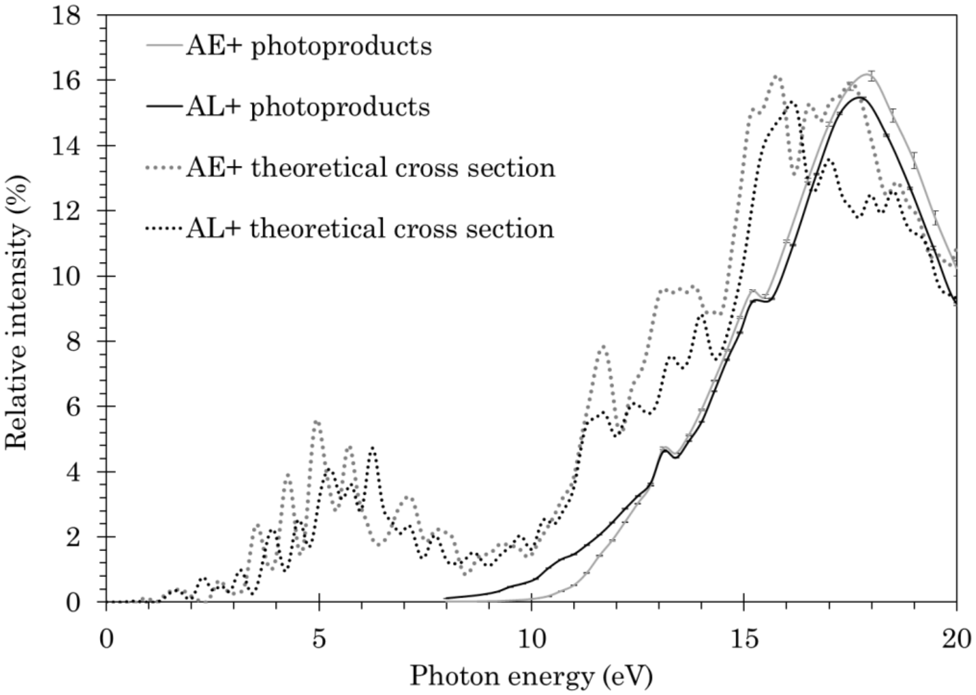

Figure 4-4 Values of the relative intensity of the photoproducts of AE⁺ and AL⁺ submitted to VUV photons as a function of photon energy (solid lines). The dotted lines are the computed photo-absorption cross sections calculated with the same method as in Malloci et al. (2004). Black lines correspond to AL⁺ and grey lines correspond to AE⁺.

4.4 Ionization and fragmentation

The yields of ionization and fragmentation as a function of photon energy are presented in Figure 4-5. The full lines correspond to the sum of all fragments from the parent cation, including those reacting with water found in the case of AE⁺, while the dashed lines represent the doubly-ionized products.

The ionization behavior of these two isomers is very similar, with double ionization (IP2) starting at a photon energy of ≈10.7 eV in both cases. On the opposite, we observe that the molecular structure has a considerable effect on the fragmentation process (full lines), with fragmentation thresholds of AL⁺ and AE⁺ differing by at least 2 eV. This structure-dependent behavior will be discussed in detail in the following chapter.

Furthermore, we observe that the ionization becomes a very competitive channel at high energies. We will discuss this in detail in Chapter 7, where we gather data on AE⁺, AL⁺, and other small and medium-sized PAHs and confirm that, as the size of PAH increases, the ionization yield increases – compared to the fragmentation yield – as suggested by Zhen et al. (2015).

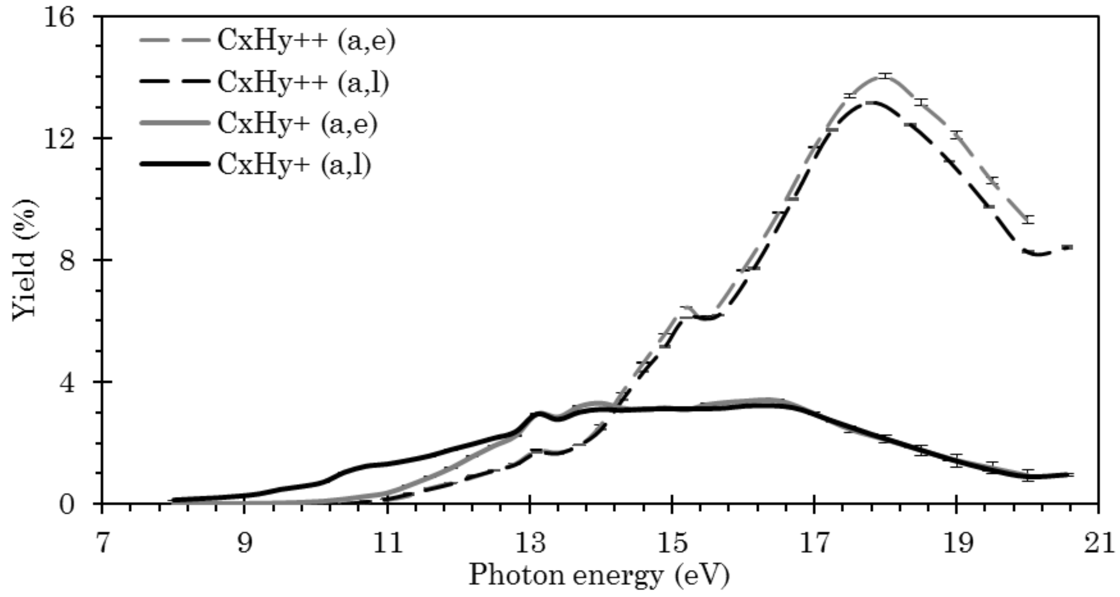

Figure 4-5 Ionization (dashed) and fragmentation (full) related abundances of both isomers (grey for AE$^+$ and black for AL$^+$).

4.5 Fragmentation pathways

Under our experimental conditions, we obtained hydrogen- and hydrocarbon-related dissociation products, as shown in Figure 4-6 and Figure 4-8. Photo-fragmentation at the lowest energies is found to be dominated by the loss of H. However, the dominant fragmentation process, mainly at mid-energies (~11-17 eV), is the loss of two hydrogens (Figure 4-6). Our experimental technique only indicates the presence of $C_{24}H_{12}^+$ in the trap, and cannot discriminate whether the mechanisms that led to these molecules were the loss of two H atoms or of a single H_2 molecule. The loss of 3 and 4 hydrogens is negligible until photon energies of about ~12.8 and ~14 eV respectively. It is interesting to note that at high enough energies the dominant fragment is the loss of 3H. At such energies, however, ionization clearly dominates, as shown previously. In the following, our interest will be focused on the lowest energies.

a) AE$^+$

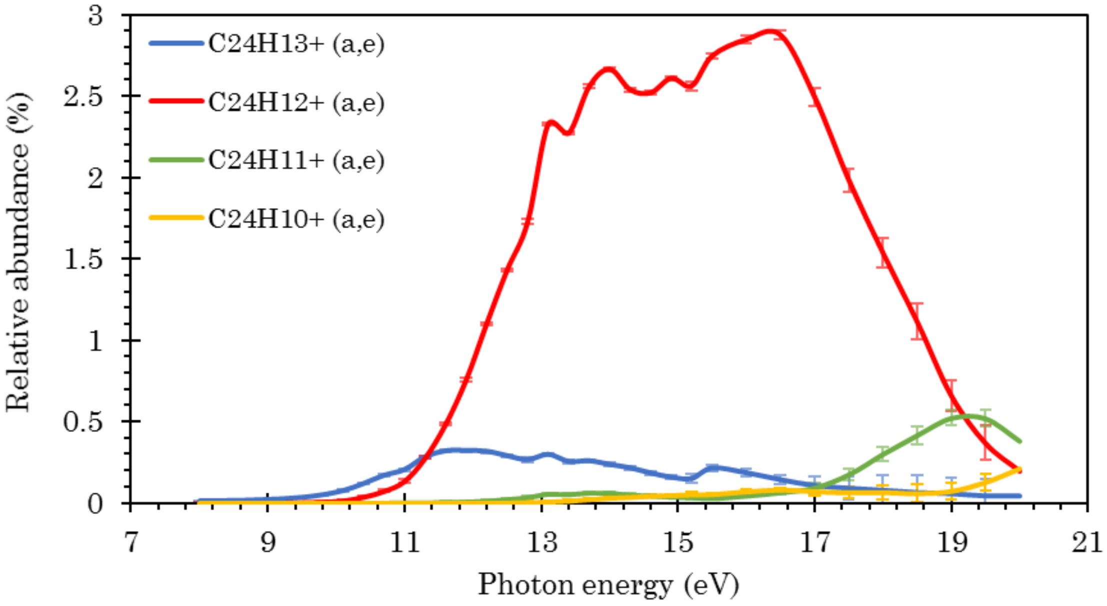

b) AL$^+$

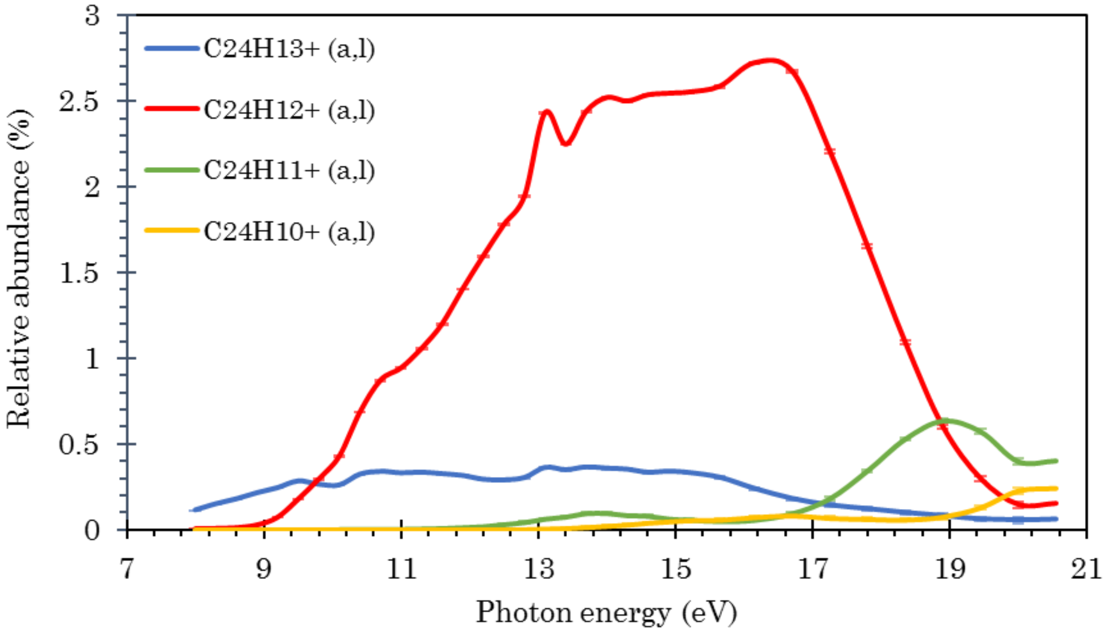

Figure 4-6 Abundances of the photofragments of AE$^+$ (a) and AL$^+$ (b) as a function of the VUV photon energy. The values are normalized to the total number of trapped ions and estimated error bars are also reported. Up to 4 hydrogen losses are observed: loss of H ($C_{24}H_{13}^+$) (blue), loss of 2 hydrogens ($C_{24}H_{12}^+$) (red), loss of 3 hydrogens ($C_{24}H_{11}^+$) (green) and loss of 4 hydrogens ($C_{24}H_{10}^+$) (yellow).

Zooming on the lowest photon energies (Figure 4-7), we observe essential differences in the -H and -2H/H_2 fragments, both on the dissociation thresholds and on the curve shape. Quantifying dissociation energies at experimental threshold is tricky, and the process was explained in Rodriguez Castillo et al. (2018). For the loss of H we obtained dissociation energies of 8.0 ± 0.1 eV in the case of AL^+ and 10.2 ± 0.2 eV in the case of AE^+ (Figure 4-7 a)). This implies an energy difference of 2.2 ± 0.2 eV. Regarding 2H/H_2 loss, the derived values are 9.3 ± 0.1 eV and 10.8 ± 0.2 eV respectively (Figure 4-7 b)), giving an energy difference of 1.5 ± 0.2 eV.

a) Single H loss

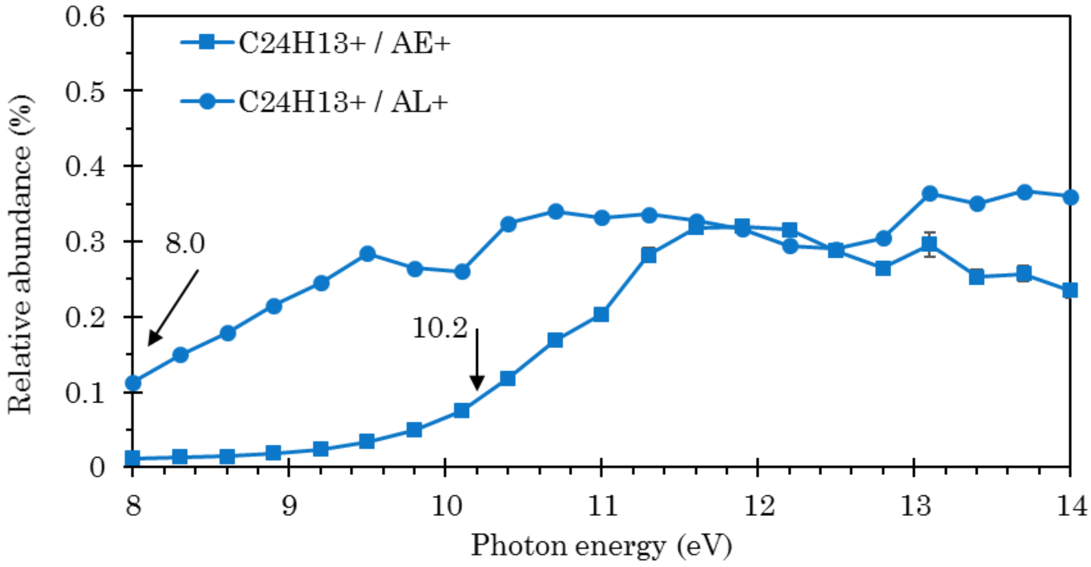

b) 2H/H_2 loss

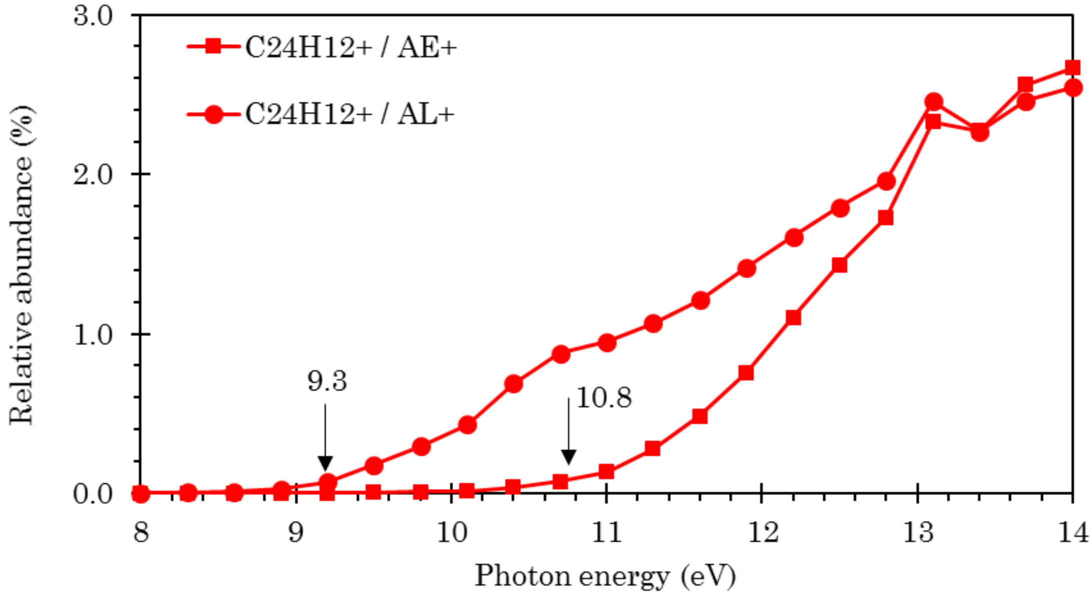

Figure 4-7 Zoom on the abundance of $C_{24}H_{13}^+$ formed by H loss as a function of the VUV photon energy. b) Similar for $C_{24}H_{12}^+$ resulting from 2H/H_2 loss. Circles correspond to AL^+ and squares to AE^+ parent cations. Error bars are included in the boxes.

Secondly, we observed minor hydrocarbon loss in both isomers, as shown in Figure 4-8. The abundances of these fragments are one order of magnitude lower than for the main hydrogen-related channels and thus do not represent significant dissociation channels. However, some trends are worth mentioning. On the one hand, the lower threshold trend that AL^+ has presented in the hydrogen losses is maintained in the hydrocarbon losses, but the exact values are harder to be derived due to the larger error bars. On the other hand, both isomers present -CH_3, and -C_2H_2 channels with similar shapes and peaks at around 14 eV, followed by the loss of "C_2H_3" with peak at ~ 16.2 eV and a final "-C_2H_4" channel peaking at ~18.4 eV. Note again that due to our experimental setup we cannot confirm whether these are single-fragment events or are due to two consecutive hydrogen and hydrocarbon losses, especially at high energies where the molecule will have enough internal energy for both mechanisms. The main difference between AE^+ and AL^+ resides in the relative abundances of these channels; the main fragmentation pathway in AE^+, -C_2H_2, is 4 times higher than the main fragmentation pathway for AL^+, which is also

-C_2H_2. In the following, focus will be given on low photon energies, at which these C_xH_y channels are negligible.

a) AE^+

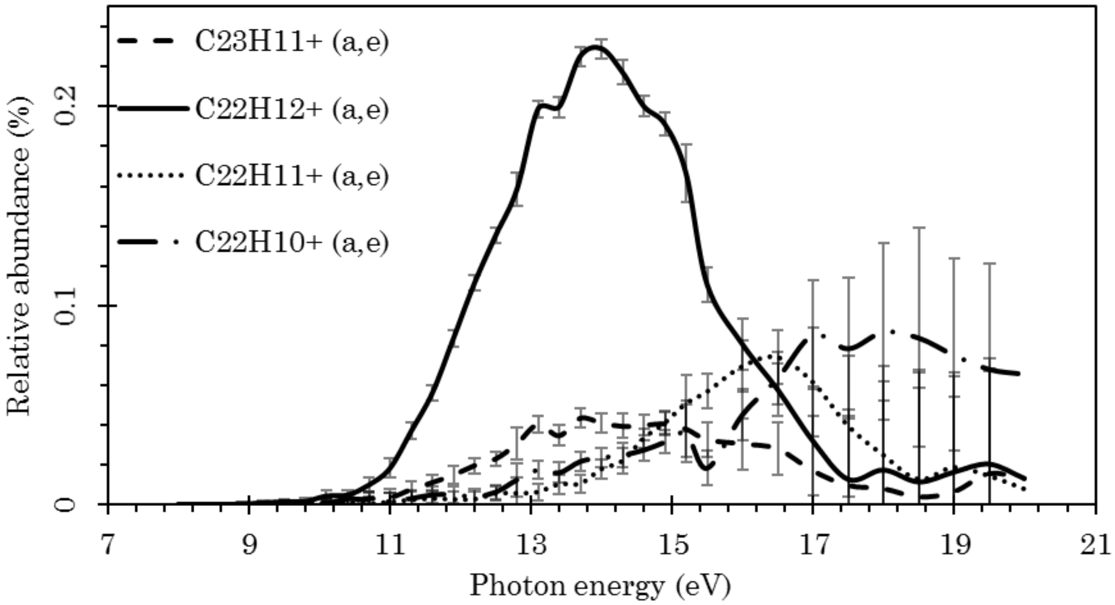

b) AL^+

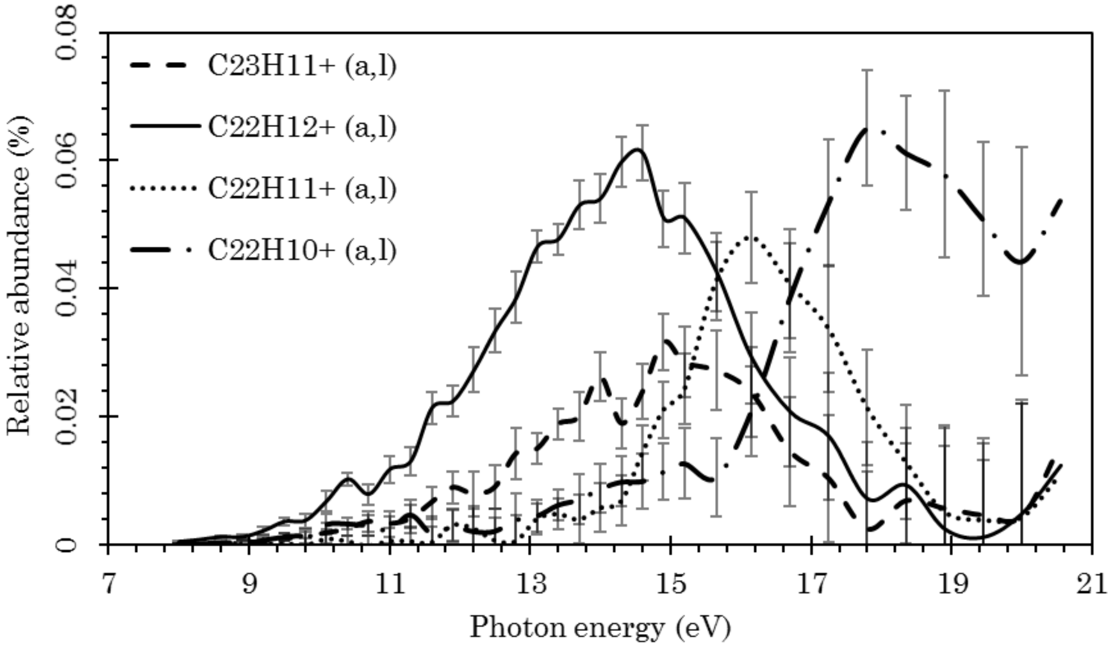

Figure 4-8 Hydrocarbon losses for AE^+ (top) and AL^+ (bottom). Note the difference in the Yield scale.

4.6 Discussion

In this section, we discuss the results obtained from action spectroscopy experiments under incident VUV synchrotron photons (energies ranging from 8 to 20 eV) absorbed by two isomeric PAH cations: AE^+ and AL^+.

First, both molecules follow similar trends in the mechanisms leading to photo-fragmentation, especially at low and medium photon energies. On the one hand, the dominant channel at the lowest energies is found to be the loss of H, following the results previously reported for smaller PAHs (Guo et al. (1999); Jolibois et al. (2005); West et al. (2014c)). On the other hand, the most significant fragmentation process, especially at mid-energies (~11-17 eV), is the loss of two hydrogens, which is in agreement with Chen et al. (2015). Due to the characteristics of the technique, it is not possible to discern between the two possible mechanisms: two consecutive H losses or loss of H_2.

However, these isomeric cations present significant differences related with the dissociation energies at play: the fragmentation channels of the non-planar molecule, AL^+, recurrently open at lower energies than those of AE^+. This can be seen in Figure 4-6, where the main differences in the fragmentation channels are observed below 11 eV. This facility of AL^+ to dissociate at lower energies evidences the effect of structure on the fragmentation mechanisms of PAHs, indicating that different geometries should be taken into account in the models of photochemical evolution of PAHs in the ISM. In the following chapter, we will tackle this difference in fragmentation energetics, in particular in dehydrogenation, from a computational point of view.

Moreover, we report similar ionization yields for both molecules (Figure 4-5), independent of the structure. This behavior is expected, because the ionization pathways are not so dependent on the molecule size or shape, since it involves promoting π electrons to unbound states, and π states have a rather weak dependence on the specific structure (Salem 1996). With fragmentation and ionization thresholds closer together, AE^+ presents a stronger competition between the yields of these two processes than AL^+, and behaves in a similar way to other, same-sized, planar cations such as benzoperylene (Zhen et al. (2016b)).

Chapter 5: *ENERGETICALLY FAVORABLE DISSOCIATION PATHS OF DIBENZOPYRENE ISOMERS*

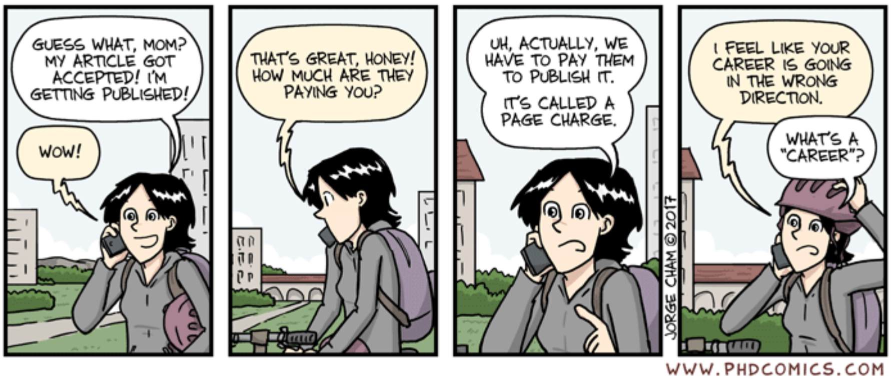
GUESS WHAT, MOM? MY ARTICLE GOT ACCEPTED! I'M GETTING PUBLISHED!
WOW!
THAT'S GREAT, HONEY! HOW MUCH ARE THEY PAYING YOU?
UH, ACTUALLY, WE HAVE TO PAY THEM TO PUBLISH IT.
IT'S CALLED A PAGE CHARGE.
I FEEL LIKE YOUR CAREER IS GOING IN THE WRONG DIRECTION.
WHAT'S A "CAREER"?
JORGE CHAM © 2017
WWW.PHDCOMICS.COM

5.1 Introduction **78**
5.2 DFT calculations **78**
5.2.1 Direct loss of H ________ 79
5.2.2 H+H loss ________ 81
5.2.3 H_2 loss ________ 82
5.3 Discussion: comparison with experimental data **86**

5.1 Introduction

In this chapter, we will analyze the experimental results presented in Chapter 4 by performing DFT calculations. The objective is to evaluate the structures and paths involved in the dissociation of both isomers, in particular the competition between the 2H and H_2 channels. We will start by showing DFT reaction paths leading towards dehydrogenation, in which reaction intermediates and transition states were computed at the B3LYP/6-31G(d,p) level following the algorithms introduced in Chapter 3. We will also discuss how they contribute to rationalize experimental results, in particular the predisposition of AL$^+$ to dehydrogenate at lower energies than AE$^+$. This study was published in Rodriguez Castillo et al. (2018). The following labelling will be adopted in order to define each hydrogen position in both molecules:

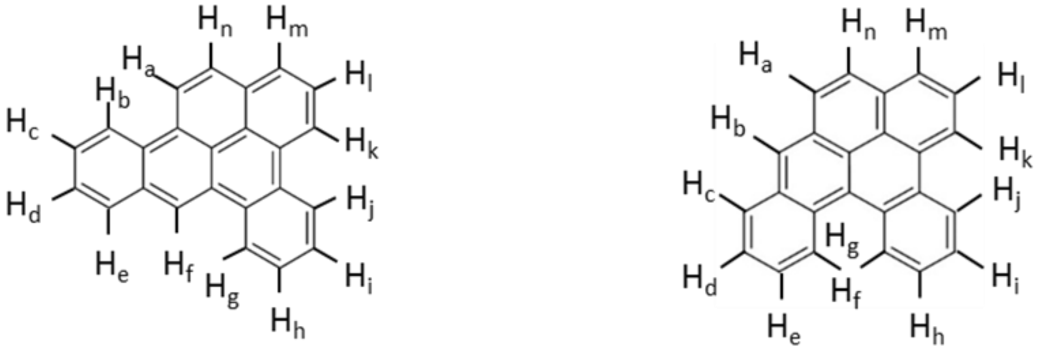

Figure 5-1 Optimized geometries of AE$^+$ (left) and AL$^+$ (right) with the hydrogens labelled.

5.2 DFT calculations

Single and double dehydrogenation mechanisms of AE$^+$ and AL$^+$ were investigated through three possible paths. For the loss of a single hydrogen only the direct loss of H was computed, since such rapid mechanism is likely to occur at the low energies at play in the ion trap experiments. MD simulations have confirmed that H loss is a fast and direct process (Simon et al. (2017)). Nevertheless, other mechanisms involving isomerization with competing energetic barriers such as the ones suggested in Solano & Mayer (2015) cannot be excluded and could be the focus of a deeper study.

In the case of the loss of two hydrogens, two mechanisms were considered: i) sequential loss of two H atoms and ii) loss of H_2 after the migration of a hydrogen to an adjacent position, the latter mechanism having been shown as the most energetically favorable path for H_2 loss (Paris et al. (2014)).

In the following we will use the term “theoretical dissociation energy” for the difference between the enthalpies at 0K (electronic energy + zero point corrections (ZPE)) of the optimized separate products and reactants, and quoted hereafter $\Delta H(0K)$.

We must specify that two possible spin-states were considered for the fragment ions: triplet and singlet for $(PAH\text{-}H)^+$; doublet and quartet for $(PAH\text{-}2H)^+$. Regarding singlet-spin states, only closed-shell systems were computed – in the restricted formalism – unless explicitly mentioned. For doublet and higher spin-states, the calculations were achieved within the unrestricted formalism, and expectation value of the $\hat{\boldsymbol{S}}^2$ spin operator was checked in order to detect potential spin-contamination. Regarding the parent ions, the AL^+ (^2A electronic state) isomer was found 0.3 eV above AE^+ ($^2A'$), which is to be expected because of the steric hindrance.

5.2.1 Direct loss of H

The removal of a single hydrogen from each and all of the sites of both molecules was considered. The resulting values of the dehydrogenated products (singlet and/or triplet) were added to those of a single H atom and compared to the initial parent geometry values. The specific values of dissociation energies for all fragment isomers for molecular cations as well as the $\hat{\boldsymbol{S}}^2$ eigenvalues can be found in Table 7-1 in the Annex.

In the case of AE^+ all the dehydrogenated products in the triplet spin-states could be easily optimized whereas closed-shell singlet spin-states could only be obtained for three sites ($-H_a$, $-H_f$, $-H_n$), the others leading to convergence problems despite the use of Fermi temperatures and quadratic convergence algorithm. In the cases in which convergence was achieved, the Singlet-Triplet gap was found in the [0.71 – 0.77 eV] range. This positive gap is in line with the results from Galué & Oomens (2011), (2012). The dehydrogenation dissociation energies lie in the [4.67 – 4.89 eV] range for these triplet-spin state products.

These values are in good agreement with the results presented for the coronene cation ($C_{24}H_{12}^{+}$) by Paris et al. (2014), whereas Chen et al. (2015) obtained a value of 5.24 eV using a different basis set.

For such large conjugated systems where triplet spin-states are stable, open-shell singlet spin states are likely to compete. These could be obtained by multireference calculations that are prohibitive for our systems. An alternative to compute singlet diradicals with unrestricted DFT methods is to perform broken-symmetry (BS) calculations. We searched for this BS ms=0 solution for the AE^{+} -H_{f} isomer. In addition, using a simplified procedure to estimate the spin-decontaminated singlet geometry (Malrieu & Trinquier (2012); Trinquier & Malrieu (2015)) we obtained a singlet-triplet gap of 0.26 eV (vertical) and 0.25 eV (adiabatic). Although such BS calculations have been achieved for one isomer only, we may expect that for all the other isomers with similar electronic structure the BS ms=0 solution to be lower in energy than the singlet closed shell one, and quite close to that of the triplet spin-state.

In the case of the non-planar molecular ion AL^{+}, a positive singlet-triplet (S-T) gap in the range [0.49 – 0.78 eV] is also found for most of the dehydrogenated species. This implies that for these cases the triplet-spin states are more stable than the closed-shell ones, as expected from theoretical and experimental studies on dehydrogenated PAHs (Galué & Oomens (2011)). The triplet-state dissociation energies reside in the [4.55 – 4.89 eV] range. Nevertheless, we have found two geometries in which the S-T gap is negative. These correspond to the removal of a hydrogen from sterically hindered sites (AL^{+} -H_{f} and AL^{+} -H_{g}) for which the S-T gap values have been found to be -1.15 and -0.95 eV respectively. Moreover, the optimization of the closed shell singlet spin state for AL^{+} -H_{f} and -H_{g} leads to the formation of an additional intramolecular C-C bond to form a 5-member ring cycle. Other authors have reported a facile 5-member ring formation in PAHs (De Haas et al. (2016)). In this case, this results in a very stable isomer, leading to an H-loss dissociation channel as low as of 3.43 eV. We may notice that planarity is not achieved yet, as seen in Figure 5-2. Several mechanisms to form this 5-member ring product could be invoked: it could start by H-migration followed by ring closure and H loss, or involve direct H loss and ring closure, either sequential or concerted. Unraveling such mechanisms is challenging, in particular due to the potential multireference character of the electronic states coming into play and possible spin-state crossing.

To summarize, considering only the thermodynamics of the reaction, the most energetically favorable paths for the loss of H in both isomers involve hydrogens in bay areas. In the case of AE^+ the most stable product is a triplet-spin state (ΔH(0K)= 4.67 eV). In addition, in AL^+, the particular local edge environment of the H_f and H_g sites favors the formation of a particularly stable closed-shell singlet spin state with a 5-member ring, reducing the dissociation energy considerably by 1.24 eV (ΔH(0K)= 3.43 eV).

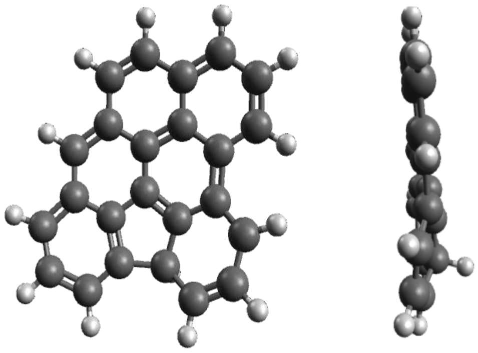

Figure 5-2. Front and side view of the optimized geometry of AL^+ after the removal of H_f.

5.2.2 H+H loss

In order to shed light on the double dehydrogenation mechanisms, we first assumed a sequential H loss after the loss of H_f from both molecules. As discussed before, this particular position involves the lowest dissociation energies, especially for AL^+ where a 5-member ring was formed in the singlet state. A second hydrogen was subsequently removed from all the remaining positions, and the theoretical dissociation energy for two consecutive H losses was estimated. In the following, we focus on the most energetically favorable paths for each isomer. Detailed results are reported in Table 7-2 in the Annex.

In the case of AE^+ we observe no significant difference in the values regardless of the position or spin multiplicity after the second hydrogen is removed (following the loss of H_f). In all cases, additional ~5 eV are needed to extract this second hydrogen, on a barrierless pathway, in addition to the 4.67 eV energy required for the first dehydrogenation in the triplet state. Previous works have estimated that the double dehydrogenation of PAHs is more favorable if the hydrogens involved are adjacent (Lindh et al. (1999)). Since H_f does not have any adjacent hydrogen, we also studied the initial removal of H_g, which requires about the same energy (+ 0.04 eV at our level of theory), followed by a subsequent subtraction of H_h, or H_i, or H_k. This most favorable geometry is the doublet spin-state AE^+ -H_g -H_h corresponding to an addition of 3.84 eV above the precursor AE^+ -H_g, or 8.55 eV above the initial reactant AE^+. It is important to note that this favorable geometry is found in other sites of AE^+, like (AE^+ -H_b -H_c), (AE^+ -H_k -H_l) or (AE^+ -H_n -H_a).

Regarding AL^+, the lowest theoretical dissociation energy corresponds to the loss of H_g from AL^+ -H_f, leading to a final fully planar structure maintaining the 5-member ring formed by the loss of H. This reaction is barrierless. The final doubly dehydrogenated species (AL^+ -H_f -H_g) lies at only 5.39 eV above AL^+ (*i.e.*, 1.96 eV above AL^+ -H_f). The remaining AL^+ -H_f -H_x positions (x= a ,.., e, h, ..., n) are less energetically favorable than AL^+ -H_f -H_g, and, in general, in agreement with the values found for the double dehydrogenation of AE^+. In brief, DFT calculations suggest that the loss of two consecutive hydrogens would require a critical energy input of 8.55 eV in the case of AE^+ and 5.39 for AL^+. This translates in an energy difference of 3.16 eV.

5.2.3 H_2 loss

Similarly to other authors, for the naphthalene and coronene cations (Solano & Mayer (2015), Paris et al. (2014)), we assumed a first H migration to the adjacent position followed by a subsequent H_2 loss. This is illustrated in Figure 5-3.

The lowest energetic paths for these isomers are reported in Figure 5-4 and Figure 5-5. We specify that only doublet spin-state potential energy surfaces (PES) were investigated. Regarding the first step (H migration), both clockwise and anticlockwise motions were explored.

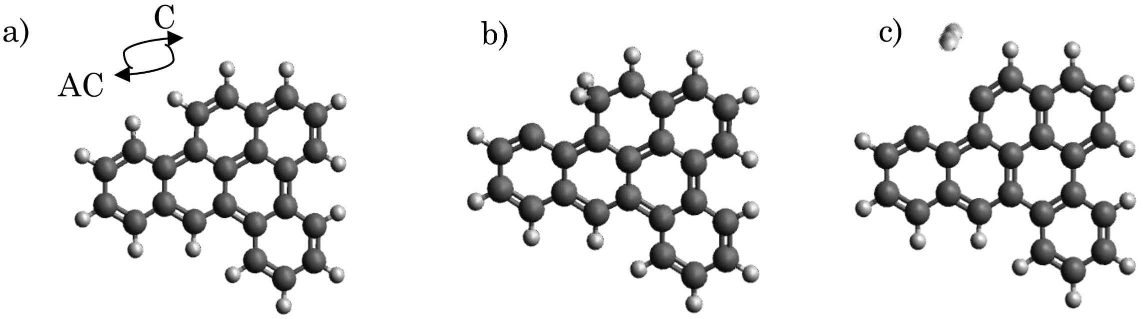

Figure 5-3. Scheme illustrating the elementary steps computed for the loss of H_2 (two-step mechanism involving bay H). a) The arrows represent the clockwise (C) and anticlockwise (AC) migration. b) Configuration after clockwise H-migration (H_b migration to the carbon bearing H_a, leading to a sp^3 configuration). c) Final geometry with the loss of H_2. AE^+ was used as an example.

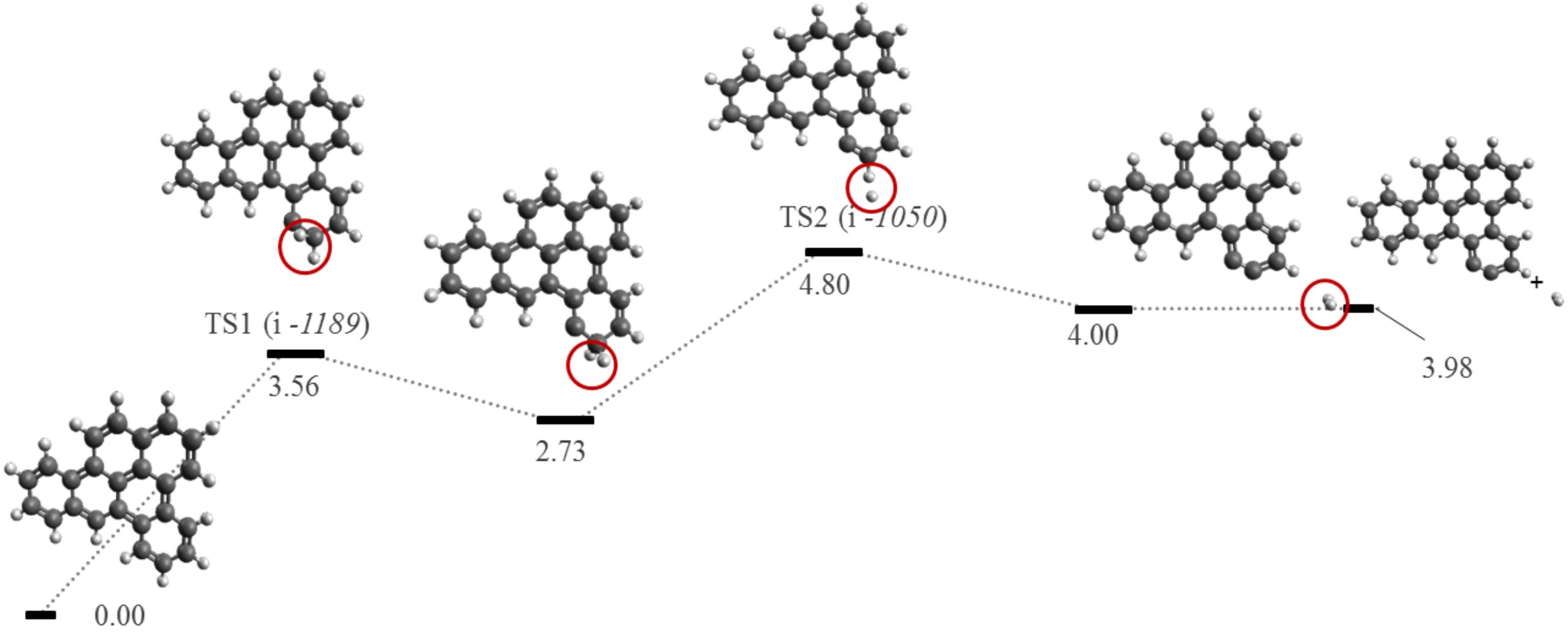

Figure 5-4. Elementary steps (B3LYP/6-31G(d,p)) of the more favorable path leading to the formation of H_2 from AE$^+$, involving the lowest energy TS. The relative energy values with respect to the reactant, given in eV, include the ZPE values. The imaginary frequencies of the TS are shown in italics and given in cm^{-1}.

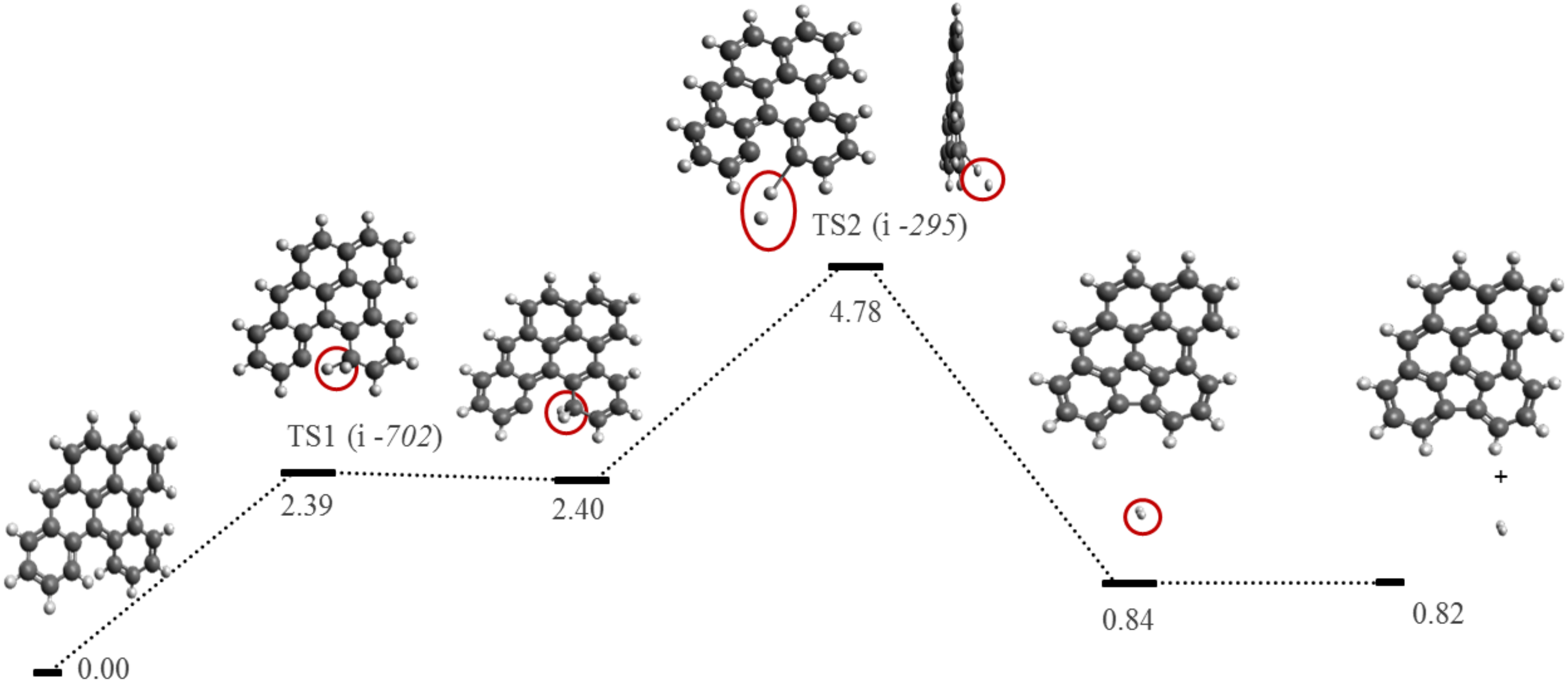

Figure 5-5. Elementary steps (B3LYP/6-31G(d,p)) of the more favorable path leading to the formation of H_2 from $AL^{+\cdot}$ The lowest energy transition states involve the special hydrogens H_f and H_g. The relative energy values with respect to the reactant, given in eV, include the ZPE values. The imaginary frequencies of the TS are shown in italics and given in cm^{-1}.

In the case of AE$^+$ the most favorable pathway corresponds to the loss of two hydrogens in the same ring, similarly to the H+H channel. The final products lie 4.00 eV above the reactant. The barrier, found at 4.80 eV, corresponds to the transition state towards the loss of the two hydrogen atoms attached to the same carbon. The values obtained for the hydrogen-migrated geometry (2.73 eV), and for the associated TS1 (3.56 eV) are in line with the ones calculated elsewhere for the coronene cation (Trinquier et al. (2017a)). For AL$^+$ the transition state corresponding to the migration of H_f onto the carbon bearing H_g (TS1) lies at a similar energy as the optimized geometry with both hydrogens (~2.4 eV), suggesting that this migration is barrierless. The barrier of the reaction is located at 4.78 eV and it corresponds to the loss of H_2, similarly to AE$^+$. The final 5-member-ring geometry lies only 0.82 eV above the parent isomer. Further, assuming a second consecutive H migration to the following carbon, we obtain a transition state of 3.27 eV and a geometry after this migration of 2.62 eV (Figure 5-6). This suggests that after the first migration, subsequent migrations may occur, resulting in a higher H_2 dissociation time than the one required for a direct H loss.

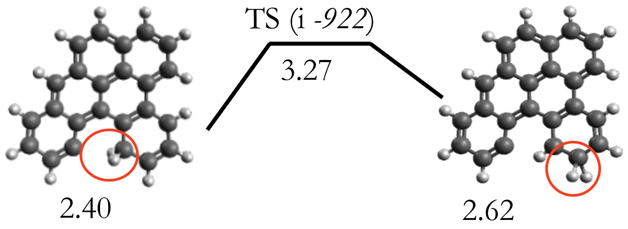

Figure 5-6. Second H migration for AL$^+$ in the path towards H_2 loss. The energy required for this second migration (around 3.3 eV) is lower than the barrier of the reaction (4.80 eV).

5.3 Discussion: comparison with experimental data

On the one hand, the DFT calculations provide a critical (minimal) energy for the fragmentation to occur. Assuming that the dissociation occurs from the ground electronic state, additional energy is expected to be stored in non-dissociating modes following intramolecular vibrational redistribution. The larger the molecule is, the larger the amount of stored energy will be. Since the two species of study are isomers we expect that, for a similar critical energy, the total energy stored in the molecule to achieve dissociation on experimental timescales will be similar. Following these statistical considerations, we can use the results of our DFT calculations to rationalize the experimental findings on AE^+ and AL^+ showed in Chapter 4.

Regarding H loss, the difference in experimental dissociation energies between AE^+ and AL^+ is around 2.2 eV (Figure 4-7 a)). DFT calculations assuming a direct H loss confirm the existence of two energetically favorable positions in AL^+: H_f and H_g. The steric hindrance in these positions, which forces the molecule out of plane, causes AL^+ to lose H from these sites at considerably lower energies (1.2 eV) than AE^+ does from any site, forming a singlet-spin state molecular cation with a 5-member ring. The additional 1 eV difference between the experimental and theoretical dissociation energies can be attributed to the energy stored in the non-dissociating modes. This suggests that direct H loss is a good explanation for the single dehydrogenation mechanism.

In the case of $2H/H_2$ loss, the experimental results (Figure 4-7 b)) indicate that the $2H/H_2$ channel opens at higher energies than the H channel by 1.3 eV and 0.6 eV for AL^+ and AE^+, respectively. Amongst the two isomers, the experimental energy difference is 1.5 eV for this channel. Resolving the specific mechanism that drives the double dehydrogenation at low energies has proven to be a challenge. Two scenarios were assumed in the DFT calculations: (i) two successive H losses (H+H) and (ii) H migration followed by a consequent H_2 loss. In the first case, computing just thermodynamical calculations we found that the loss of H+H requires at least 2.6 eV more energy in AE^+ than in AL^+. We note that, except for the case of the 5-member ring formation in AL^+, the most energetically favorable path for the sequential loss of two H from the energetic point of view is the loss of two adjacent hydrogens from the same ring, in which the first H removal relieves some steric hindrance. The overall process requires at least 6 eV and 8.6 eV for AL^+ and AE^+, respectively. In the case of H_2 loss, we found more energetically favored channels with maximum energies of around 5 eV.

From these static energetic considerations we can rationalize the difference in the experimental curves observed in Figure 4-7 b) by invoking the role of the special H of AL^+ (H_f and H_g) in opening lowest energy dissociation channels.

Moreover, we can conclude that competition between H_2 and 2H channels could be possible for AL^+ starting at about 9.3 eV. In the case of AE^+, the large energy (8.6 eV) required for the 2H loss would be difficult to reconcile with an absorbed energy of ~10 eV, considering that some of this energy will be stored in the other non-dissociating modes. Therefore we likely observe the opening of the H_2 channel at ~10.8 eV. This conclusion is of particular relevance, and will be discussed further in Chapter 7. Astrophysical observations have confirmed the high abundance of this molecule in space, but its origin is still under debate. For this reason, the correlation between non-compact PAHs containing bay regions and the potential easier route for H_2 formation should be further studied.

Chapter 6: DYNAMICS OF DISSOCIATION OF DIBENZOPYRENE ISOMERS: IPEPICO EXPERIMENTS, RRKM MODELLING AND MD

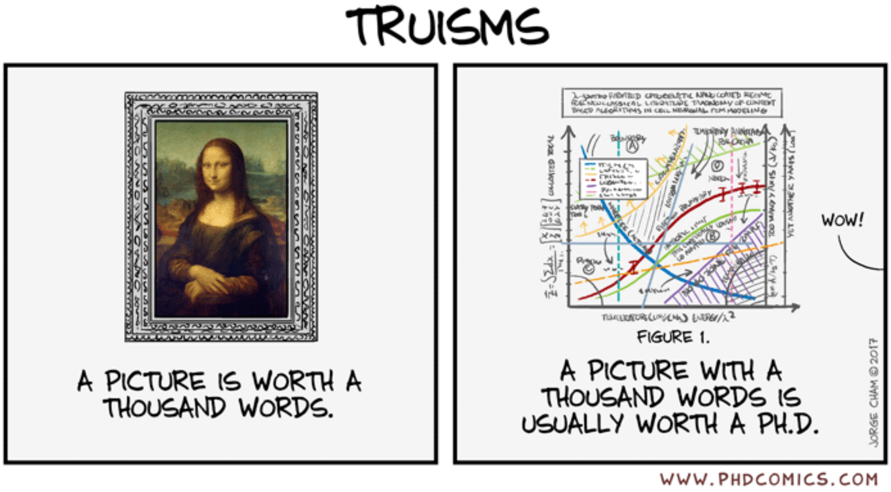
TRUISMS
A PICTURE IS WORTH A THOUSAND WORDS.
WOW!
FIGURE 1.
A PICTURE WITH A THOUSAND WORDS IS USUALLY WORTH A PH.D.
JORGE CHAM © 2017
WWW.PHDCOMICS.COM

6.1 Introduction **90**
6.2 iPEPICO Experimental details **90**
6.3 Breakdown curves and activation parameters **91**
6.4 Exploration of dissociation through molecular dynamics . **97**
6.5 Comparison of results from different techniques **104**
6.5.1 Comparison of activation energies with DFT results ____ 104
6.5.2 Comparison of threshold energies with ion trap results ____ 106
6.5.3 Comparison of dissociation rates ____ 107
6.6 Summary and discussion **108**

6.1 Introduction

In this chapter, we explore the unimolecular dissociation dynamics for AE^+ and AL^+ using iPEPICO experiments and modelling the results with RRKM theory in order to obtain dissociation rates, as described in Chapters 2 and 3. We complement these results on the dynamics of PAHs with MD/DFTB extensive simulations, introduced in Chapter 3. As in previous chapters, we will discuss in particular the results obtained for the dibenzopyrene isomer molecules that are the core of this thesis.

6.2 iPEPICO Experimental details

The iPEPICO experiments were carried out in the VUV beam at the SLS facility as described in Chapter 2. A set of PAH – with sizes spanning from 12 carbon atoms (acenaphtylene) to 24 (coronene and the dibenzopyrene isomers) – were studied. The overall results are presented in West et al. (2018). Photoion mass spectrometry studies have been previously carried out on several PAHs by Jochims et al. (1999), using synchrotron radiation. In these experiments, however, the threshold electrons were not selected, which means that the actual internal energy of the molecule could not be determined with precision. In addition, the authors could not derive precisely the dissociation rate; they assumed that it was typically 10^4 s^{-1}, based on experiments on benzene (Jochims et al. (1994)). As an example, the internal energy they derive from pyrene cation is 9.06 eV, which would correspond, according to our work (West et al. (2018)), to a rate of 10^2 s^{-1} and not to 10^4 s^{-1}.

We discuss here the case of AE and AL molecules that were subjected to VUV synchrotron radiation energies between 15.8 and 20.4 eV and 17.4 and 21.5 eV respectively, with energy steps of typically 0.1 eV in the relevant energy ranges. The samples were inserted in the chamber via a heated oven inlet system (Hemberger et al. (2017)) to temperatures of 433 K for AL and 453 K for AE. The first ionization energy was 7.11 eV for AE^+, taken from Lias et al. (2003), and 7.05 eV for AL^+, obtained from the current experiment in a low energy scan. A field strength of 120 Vcm^{-1} was selected in order to provide long ion residence times necessary for the energy resolution required at threshold.

As a drawback, this leads to large TOF peaks (see Figure 6-1), which means that the peaks from the parent and the fragmented molecules (in this case involving the loss of one and two hydrogens as we will see in the next section) will be overlapped. A deconvolution procedure was carried out based on the idea that, as each daughter peak grows with increasing photon energy, the center of the overall TOF distribution will shift towards the TOF peaks of the daughter ions. This shift will be proportional to the relative abundance of all the observed peaks (parent + daughters) and their respective ^{13}C contributions. This deconvolution procedure has been widely used, in particular by the group of Prof. P. Mayer (West et al. (2012), (2014b)). For this fitting, performed with the multi peak fitting protocol included in the IGOR PRO 4 (WaveMetrics, Lake Oswego, OR) software package, we assume that the peak positions are constant and all the peaks have the same full-width-half-maximum.

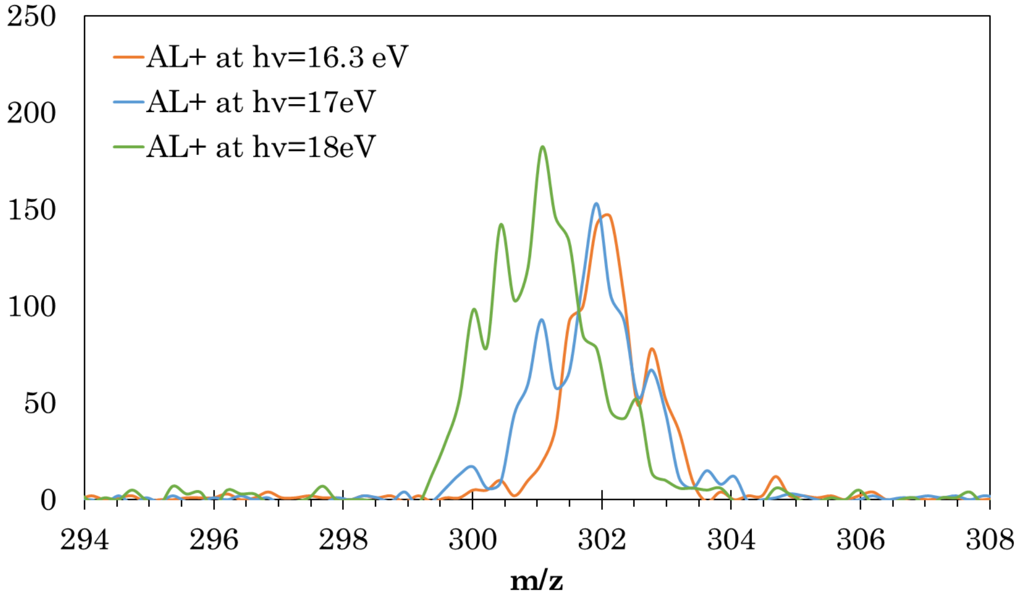

Figure 6-1 TOF mass spectra at different photon energies for AL$^+$.

6.3 Breakdown curves and activation parameters

We used the program minimal-PEPICO, explained previously in Chapter 2 for the actual fitting of the experimental breakdown diagrams, to plot each ion fractional abundance against the incident photon energy. The shape and slope of the breakdown curves are characteristic of the reaction mechanism, and establish distinguishable parallel and sequential processes in the breakdown diagrams, especially interesting for the isomers under study, since this is not achievable through ion trap experiments, as discussed previously. Statistical RRKM theory was used to model the experimental curves and derive the activation energies (E_0) and entropies ($\Delta^{\ddagger}S$), with rates given by $k(E) = \frac{\sigma N(E-E_0)}{h\rho(E)}$ (Chapter 3).

The breakdown diagrams of the unimolecular reactions of AE^+ and AL^+ are shown in Figure 6-3 and Figure 6-4, including the RRKM statistical fits. The corresponding activation energies (E_0) and entropies ($\Delta^{\ddagger}S_{1000K}$), obtained through RRKM calculations are given in Table 6-1. Let us specify that a given value of E_0 does not necessarily correspond to a specific thermodynamic dissociation reaction, but to the minimum energy for a reaction to proceed, so it will be referred to as 'reaction energy'.

These values are optimized in order to obtain the best fit to the experimental data. This fit was assumed acceptable if the relationship between the experimental (*Expt*) and calculated (*Calc*) points of the breakdown diagrams given by Equation 6-1 was at maximum 0.5%. This equation gives an approximated correlation coefficient, which describes the strength of the association between two variables.

Equation 6-1

$$1 - \frac{\Sigma((Expt)(Calc))}{\sqrt{\left(\Sigma((Expt)(Expt))\Sigma((Calc)(Calc))\right)}}$$

The values of E_0 and $\Delta^{\ddagger}S$ corresponding to such calculated points were considered as the limits of the error. As can be seen in Table 6-1, the obtained errors are significant (with values > 0.5 eV). This is mainly due to the extrapolation of the dissociation rate curve to its vanishing point, located at lower energies than the observed onset due to the kinetic shift that will be explained below. Moreover, in the case of secondary, parallel processes such as the loss of two consecutive hydrogens, constraining their exact activation energy is difficult because the breakdown curve carries information about the loss of H_2.

Such large ions – with many internal degrees of freedom – dissociate slowly, thus lengthening the dissociation rates well beyond the TOF range of the parent (Bodi et al. (2009)). This implies that not all the ions with internal energy above the bond-dissociation energy will fragment on the timescale of the experiment. This is due to the so-called kinetic shift, an effect in which the fragment ions appear only at energies (far) above their true thermodynamic energy thresholds (Chupka (1959); Lifshitz (1982); Huang & Dunbar (1990)). This effect can be seen in Figure 6-2, in which the parent breakdown diagram is shown for 9 unsaturated planar PAHs with sizes from 10 to 24 carbon atoms. We clearly observe the additional energy needed to open the dissociation thresholds of the larger molecules, despite all of them having ionization energies in the range of 7(± 1) eV. For this reason, any discussion of the reaction energies for these systems must take into account the reaction rates as done herein by employing the RRKM k(E) in the modeling process. Let us not forget that the energy that remains after the ionization corresponds in full to the internal energy of the ion.

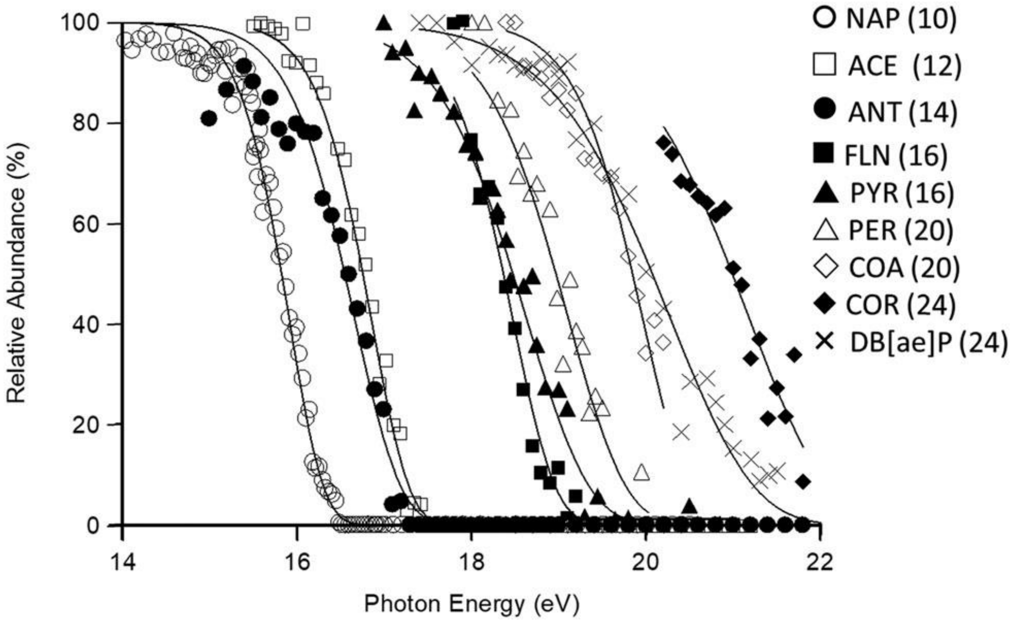

Figure 6-2 Kinetic shift due to the increase of degrees of freedom, as the size of the molecule increases. Parent ion decays are observed to occur at significant higher energies for the larger PAHs (West et al. (2018)). These decays have similar dissociation threshold values (*i.e.*, AL$^+$ is not included). The number in parenthesis corresponds to the number of carbon atoms in each molecule.

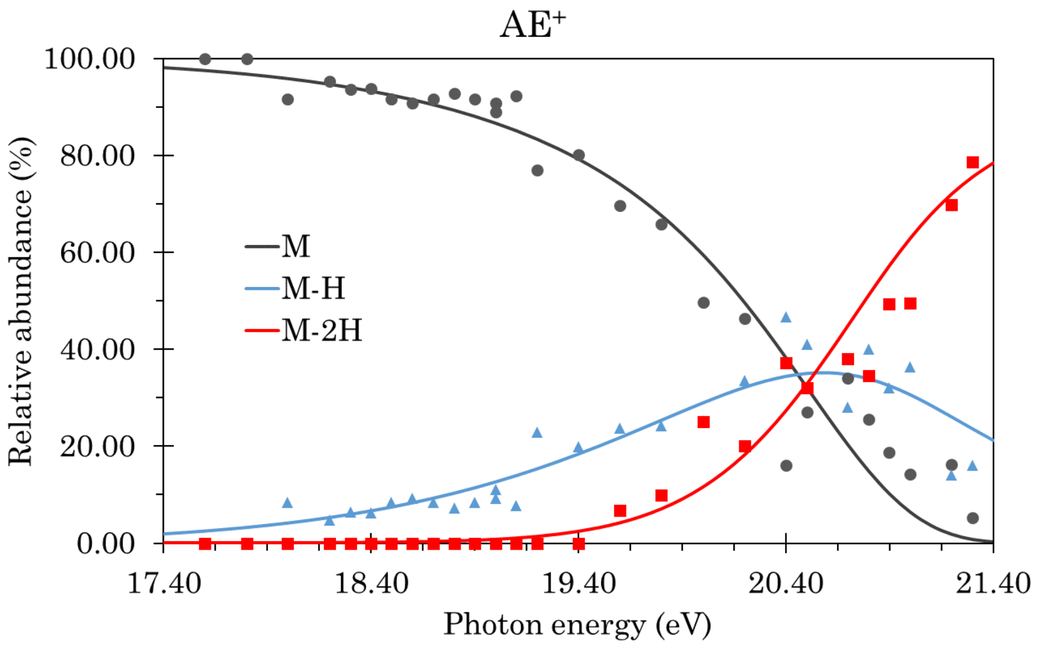

Figure 6-3 iPEPICO breakdown diagrams obtained for AE⁺ with an extraction field of 120 V/cm. The points correspond to the experimental values and the lines represent the statistical fits obtained by RRKM modelling.

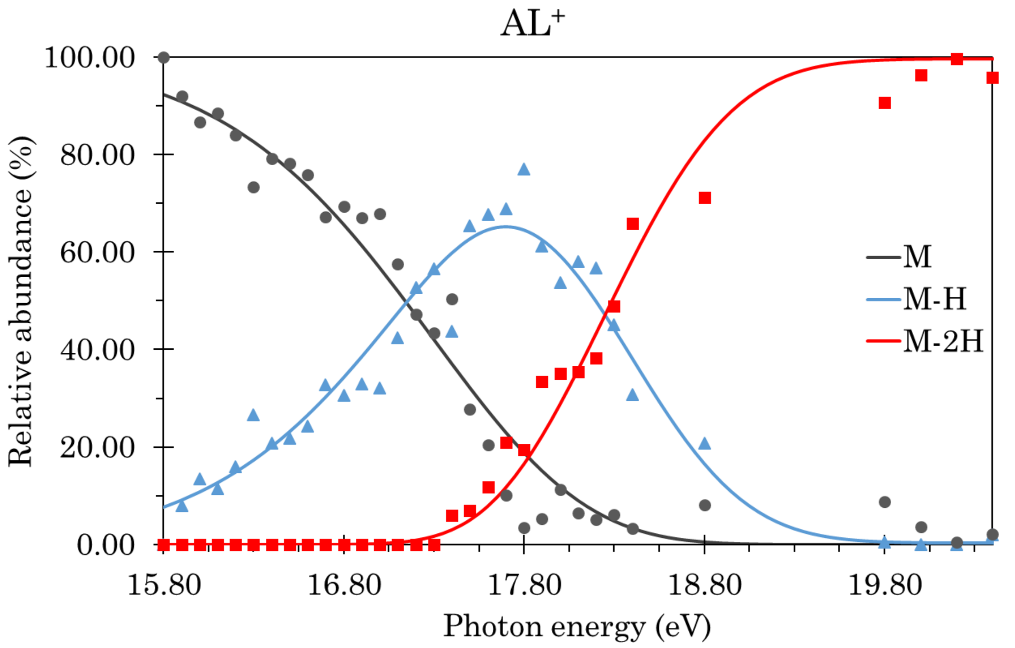

Figure 6-4 iPEPICO breakdown diagrams obtained for AL⁺ with an extraction field of 120 V/cm. The points correspond to the experimental values and the lines represent the statistical fits obtained by RRKM modelling.

As can be directly observed from the figures, the photon energies needed to dissociate AL^+ are much lower than for AE^+, which is in line with the results obtained both in ion trap experiments at SOLEIL (Chapter 4) and with DFT calculations (Chapter 5). Moreover, Figure 6-3 indicates that the first dissociation channel to open in AE^+ is the loss of H, with a parallel competing channel opening at photon energies of around 19.5 eV, corresponding to the loss of H_2. Sequential loss of H is expected to occur at higher energies (in competition with H_2), especially when the H loss channel decreases. However, precisely distinguishing the exact value of the H+H threshold from these experimental points is not straightforward. On the other hand, in Figure 6-4 we see the second fragmentation channel opening at photon energies of around 17.3 eV, coinciding with the decrease of the –H channel, which indicates a sequential loss of H.

In Table 6-1 we present the values of the activation energies calculated for both isomers. In the case of AE^+, we obtain very similar values for the loss of H and H_2; the shift observed on the breakdown diagrams can be explained by the slower dissociation times that the loss of molecular hydrogen require before dissociation, as seen in the previous chapter. The second, sequential, loss of H is found to involve a lower activation energy compared to the first H loss, as is expected (Ling et al. (1995); West et al. (2014c)). In the case of AL^+, both dehydrogenation energies (in particular the one corresponding to H loss) are substantially lower than for AE^+ and, in general, lower than the results reported up to now for any normally-hydrogenated planar PAH. The corresponding activation energies are negative, indicating a 'tight' reaction typically associated with molecular rearrangements, which is in line with what we expect – formation of a pentagonal ring –. We will compare in detail the energies obtained for the loss of one and two hydrogen atoms for different PAHs further in Chapter 7 [Figure 7-6 (see West et al. (2018))]. These values have been obtained taking into account the temporal window explored in the iPEPICO experiments.

Table 6-1 Activation energies and entropies obtained by fitting the iPEPICO experiments with a RRKM model.

	E_0 (eV)		$\Delta^{\ddagger}S_{1000K}$ (J K^{-1} mol^{-1})	
	AE^+	AL^+	AE^+	AL^+
$C_{24}H_{14}^{+} \rightarrow C_{24}H_{13}^{+} + H\cdot$	4.44 ± 0.56	2.85 ± 0.56	48 ± 31	-3 ± 38
$C_{24}H_{14}^{+} \rightarrow C_{24}H_{12}^{+} + H_2$	4.46 ± 0.62	–	56 ± 34	–
$C_{24}H_{13}^{+} \rightarrow C_{24}H_{12}^{+} + H\cdot$	3.50 ± 0.65	2.35 ± 1.3	66 ± 36	-4 ± 100

We can obtain dissociation rates for each reaction as a function of the internal energy of the molecule as a by-product of RRKM fitting and the derived activation parameters. As we mentioned in the astrophysical context, these are of particular interest in order to model the photochemical evolution of PAHs in photodissociation regions. Figure 6-5 compares the rates corresponding to the loss of H from the parent cations (AE^+ and AL^+) and from the dehydrogenated cations ($[AE\text{-}H]^+$ and $[AL\text{-}H]^+$).

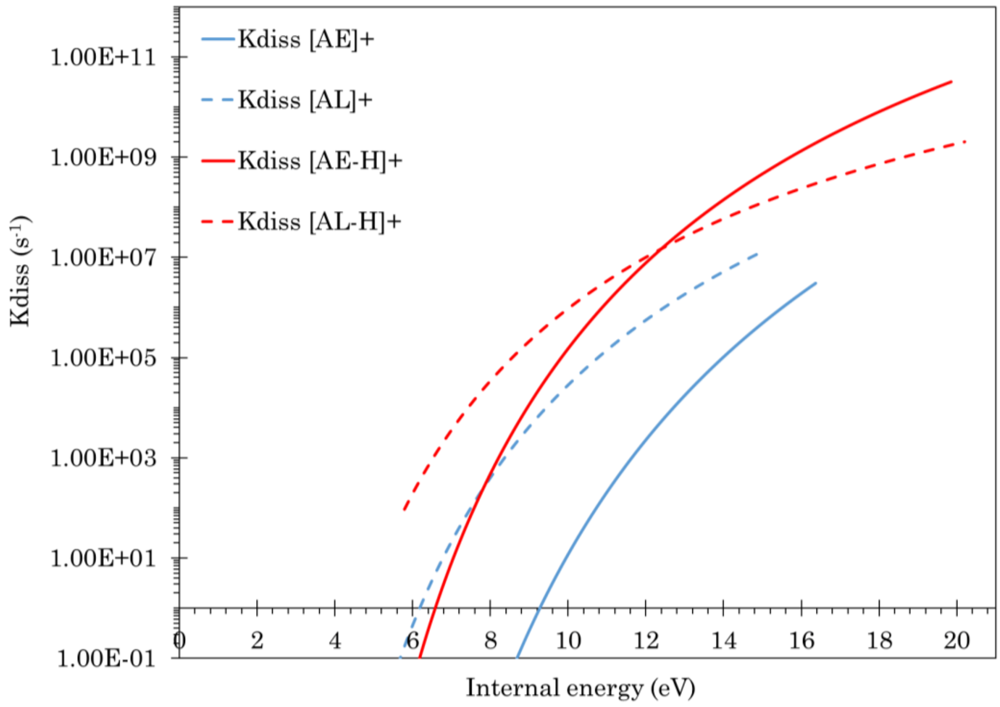

Figure 6-5 Comparison of the dissociation rates as a function of the internal energy for the loss of H from the parent cation $[M]^+$ – blue – and from the singly dehydrogenated cation $[M\text{-}H]^+$ – red. Full lines: $M=AE^+$; dotted lines: $M=AL^+$. These rates were obtained using RRKM theory and the activation parameters reported in Table 6-1.

6.4 Exploration of dissociation through molecular dynamics

In RRKM theory, only the transition states of a specific reaction path are used in order to obtain the dissociation rates, omitting all other dissociation channels and possible isomerization mechanisms, which in principle should be included in the calculation. Indeed, it is now well known that isomerization reactions are likely to occur within PAH molecular ions within an energy range of a few eV (Trinquier et al. (2017a), (2017b),Parneix et al. (2017)). Doing so in the case of such large molecules would imply the analysis of extremely complex PES. As an alternative, MD simulations, in which no *a priori* information is needed, can be performed.

For this reason, and following the procedure explained in Section 3 of Chapter 3, extensive MD/DFTB simulations were carried out within the 100 ps – 1 ps timescale. For each dibenzopyrene cationic isomer, three internal energies were investigated: 26, 28 and 30 eV, with the aim of detecting differences in the fragmentation 'thresholds'. Typically, 100 trajectories were ran at each energy. We may note, and this is a drawback of the approach when there is a need to compare with experimental photodissociation data, that high energies must be used in order to observe dissociation in a reasonable timescale. MD/DFTB simulations in this context will only provide interesting insights into the dissociation mechanisms, that otherwise can become difficult to intuit (Solano & Mayer (2015)).

The ratios of the fragment ions as a function of simulation time are presented in Figure 6-6. It is important to mention that not all the obtained fragments have been depicted; the figures only show those whose value was higher than 1% at 500 ps for both isomers. Minor (1%) C_xH_y channels occur at the highest energies, in particular for AL^+. For the lowest energy, at least 1 ns is needed to see any fragmentation in AE^+, which corresponds to a hydrogen loss. For the other energies, dissociation already starts at 100 ps, so simulations were ran up to 500 ps, which appears as an interesting time to compare dissociation of the two molecular cations.

The results show that at 26 eV of internal energy there is already a clear difference between the statistical dissociation of the isomers; only 1% of the AE^+

ions dissociate after 1 ns, *versus* 9% in the case of AL^+. For the latter, H loss is the main dissociation mechanism, followed by H_2 and CH_3 losses (Figure 6-6 a) and b)). When the internal energy is increased by 2 eV, we can observe that 5% of the AE ions have dissociated and lost a hydrogen atom (3%) or acetylene (2%). Meanwhile 7% of the AL ions have lost a single H, 4% have undergone 2H/H_2 loss, 4% of the losses are equally divided between "-CH_3" and "-C_3H_4", while acetylene loss represents 8% of the fragment ions, adding up to a total of 27%. The overestimation of the acetylene channel in comparison the dehydrogenation channels may be due to the DFTB potential (Simon et al (2017)). At this internal energy, we can see that 2H/H_2 loss for AL^+ is already higher than any of the two channels in AE^+, where no double dehydrogenation loss has been obtained. Most of the dissociation mechanisms for AL^+, especially dehydrogenation pathways, involve the formation of a 5-member ring (see Figure 6-9).

Finally, 30 eV is the highest internal energy explored by our MD/DFTB simulations. Figure 6-6 e) shows that the C_2H_2/H branching ratio has evolved considerably for AE^+, with still no presence of 2H/H_2 fragments. We do observe, however, a small percentage of ions that lose CH_3 and "C_3H_3". All the dissociations in AE^+ ascend to 17%, which is considerably lower than for AL^+ (61%). This 61% of resulting fragment ions are found to be divided as follows: (Figure 6.6 f)): $C_{24}H_{13}^+$: 19%, $C_{22}H_{12}^+$: 17%, $C_{24}H_{12}^+$: 5%; and finally $C_{23}H_{11}^+$, $C_{22}H_{11}^+$, $C_{21}H_{12}^+$, $C_{21}H_{11}^+$ each accounts for 3%. However, the exact fragmentation pathway become less obvious at this (high) energy. For example, we observe that only 1/5 of the $C_{24}H_{12}^+$ molecules arise from H_2 loss, and $C_{22}H_{11}^+$ was reached after a sequential loss of H and C_2H_2. We also observe smaller (=1%) fragments such as $C_{21}H_{10}^+$, not shown in the figure, which we have not detected in the experiments.

a) AE$^+$ at 26 eV

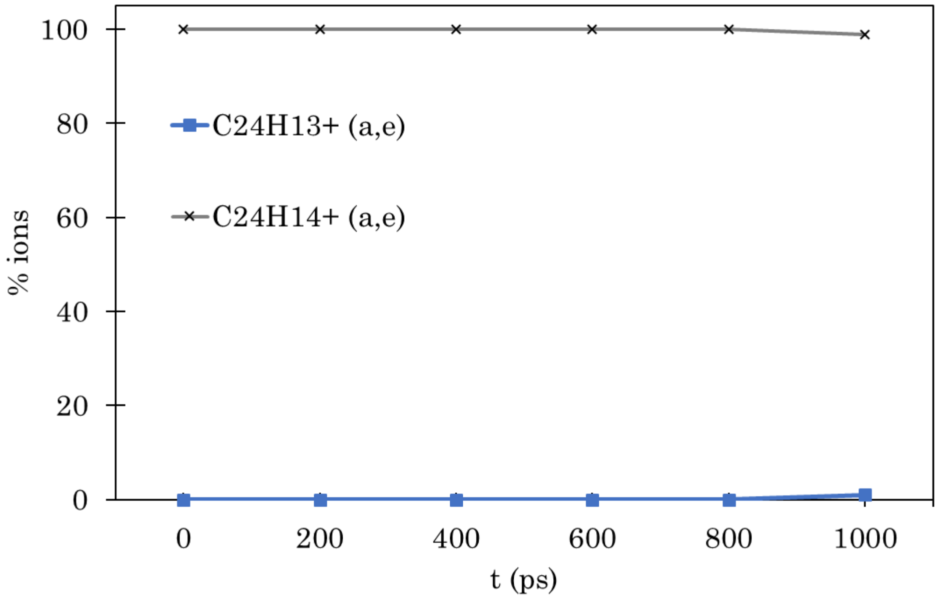

b) AL$^+$ at 26 eV

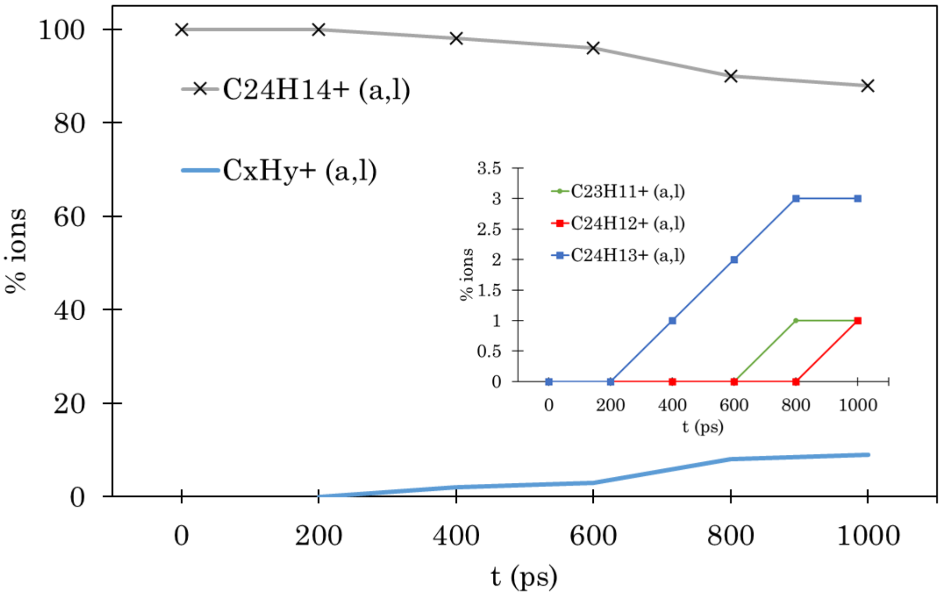

c) AE$^+$ at 28 eV

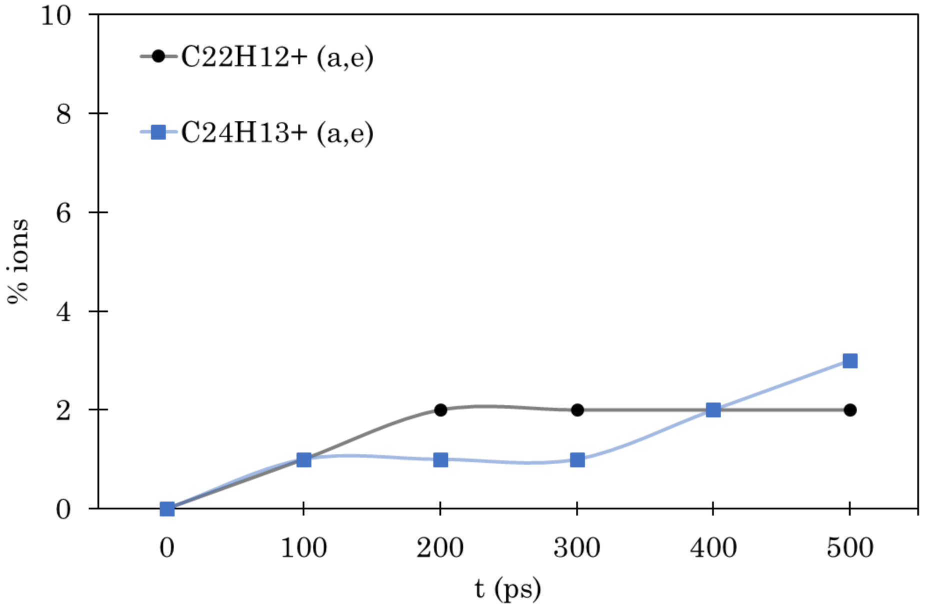

d) AL$^+$ at 28 eV

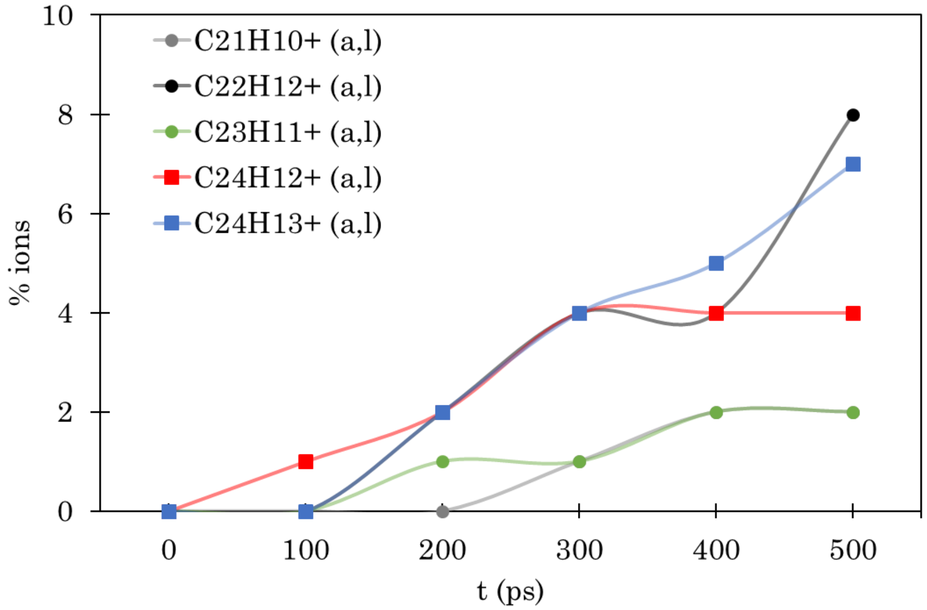

e) AE$^+$ at 30 eV

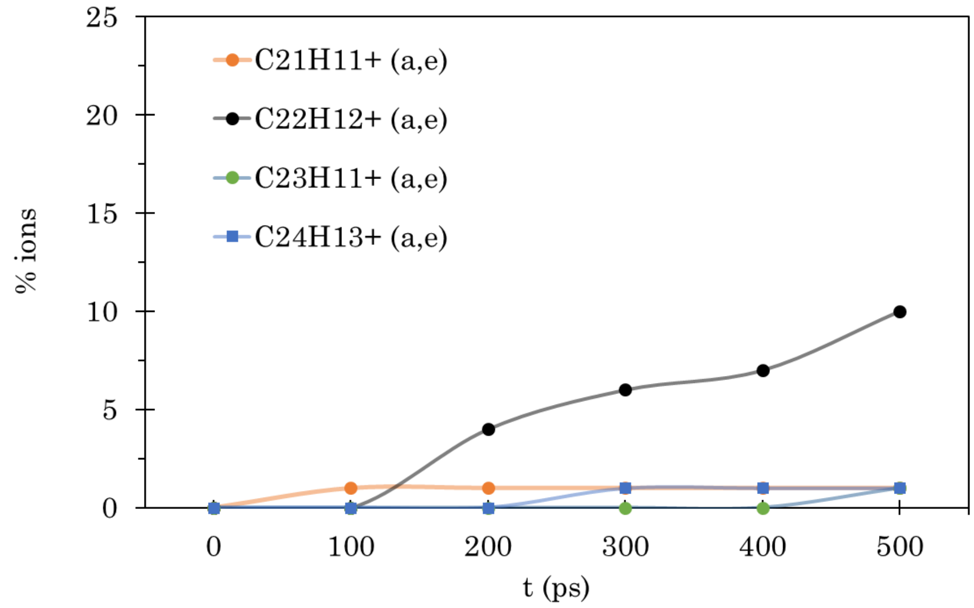

f) AL$^+$ at 30 eV

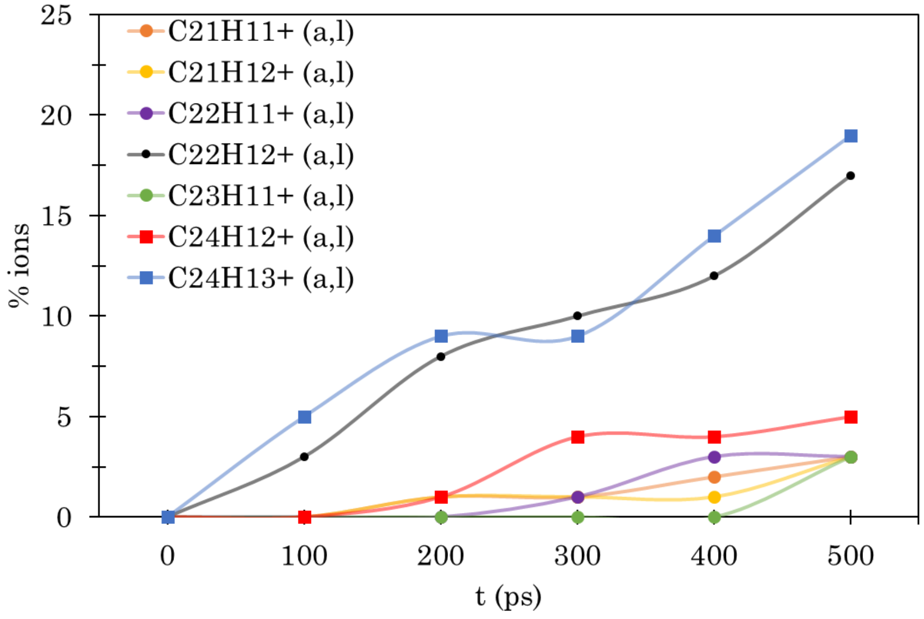

Figure 6-6 MD/DFTB simulations: Dissociation of AE$^+$ and AL$^+$ with 26 eV (a,b), 28 eV (c,d) and 30 eV (e,f) of internal energy. Point-connecting lines are introduced for clarity. The parent ions are only depicted in (a) and (b) as an example.

Focusing on the main dissociation channels, H, 2H/H_2 and C_2H_2, we can follow their evolution as a function of the internal energy (Figure 6-7) at 500 ps. As expected, the non-planar molecule that contains hydrogens in bay regions (AL^+) dissociates earlier, and more, than the planar one (AE^+). This tendency is directly related with the structural rearrangements that occur in our simulations, in a similar way as reported in Simon et al. (2017).

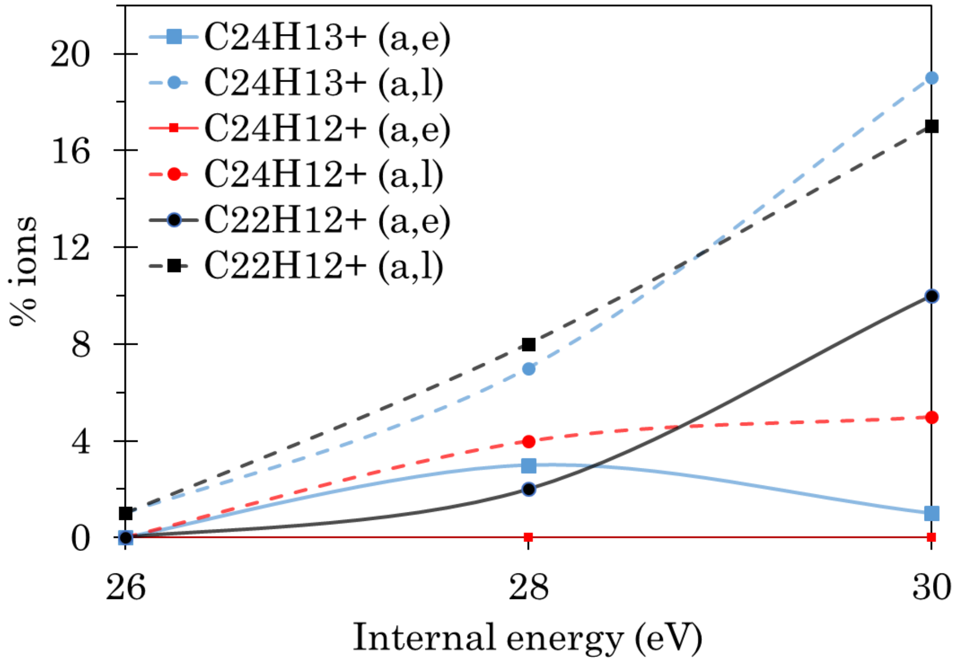

Figure 6-7 Evolution of fragments as a function of the internal energy (26, 28, 30 eV) at 500 ps for both isomers from MD/DFTB simulations. Straight lines and square markers correspond to AE^+ while dashed lines and circles correspond to AL^+.

In particular, at the lowest energy (26 eV), isomerization into 5-member ring AL ions occurs in all the H-loss mechanisms. Figure 6-8 depicts an example. Interestingly, the formation of the 5-member ring structure does not always occur in the carbon sites related to bay-hydrogens, and globally, the molecule undergoes multiple re-structurations before the loss of H. Indeed, the molecular ion possesses enough internal energy to explore many regions of the PES. This rearrangement is still observed at 28 eV (Figure 6-9), where both double dehydrogenation mechanisms (2H and H_2) occur. Typically, the protagonists of these dehydrogenations are H atoms that are not directly involved in the 5-member ring (see for example Figure 6-8 and Figure 6-9). Finally, at high energies we see the migration of H atoms inside the AE$^+$ molecule (Figure 6-11), and many more ring openings for AL$^+$ (Figure 6-10), as is to be expected.

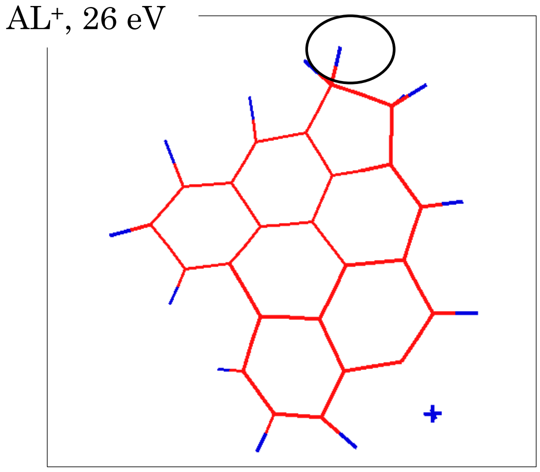

Figure 6-8 MD/DFTB simulations: Screenshot of the molecular geometry of AL$^+$ before the loss of H from a sp^3–C center after the formation of a 5 member ring at 26 eV of internal energy.

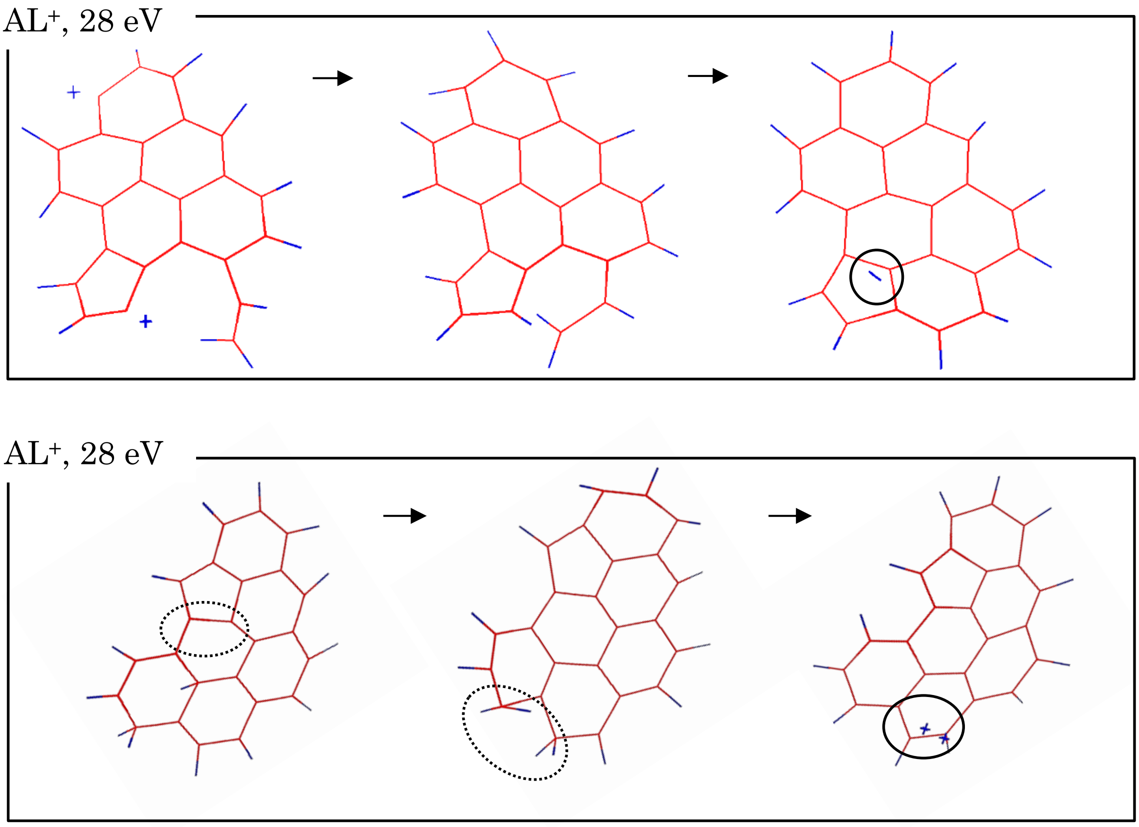

Figure 6-9 Two sequences leading to H$_2$ loss (top) and 2H loss (bottom) in AL$^+$ at 28 eV of internal energy from MD/DFTB simulations. The first step always involves the formation of a 5-member ring. For H$_2$ loss, the ring adjacent to this 5-member ring opens and closes before the H$_2$ loss. For the loss of 2H a hydrogen migration occurs inside the molecule before 2 losses of (adjacent) hydrogens.

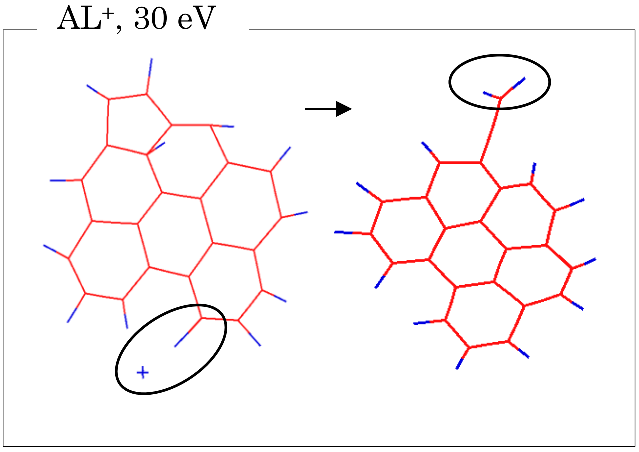

Figure 6-10 MD/DFTB simulations: Example of two sequential H losses in AL$^+$ at 30 eV of internal energy. The first H atom leaves from a carbon bearing two hydrogens. Then the 5-member ring opens and another H from the CH$_2$ group is lost.

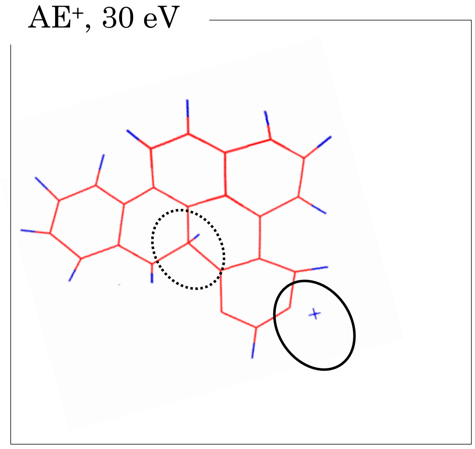

Figure 6-11 MD/DFTB simulations: Example of H loss in AE$^+$ at 30 eV of internal energy. Similarly to the case of AL$^+$ at lower energies in the hindered sites, we observe H migrations inside AE$^+$ at this high energy (dashed circle). The full circle corresponds to the actual loss of H.

6.5 Comparison of results from different techniques

6.5.1 Comparison of activation energies with DFT results

One of the attractions of the iPEPICO results resides on the fact that it is possible to discriminate between two possible mechanisms for the double dehydrogenation, thus providing reaction energies for each channel. We can then compare (see Table 6-2) the activation energies obtained from the RRKM analysis of the iPEPICO experiment, to the DFT-calculated dissociation energies of the different pathways that we had previously discussed in Chapter 5.

Table 6-2 Comparison of dissociation energies calculated by DFT with the activation energies obtained from the RRKM analysis of the iPEPICO data.

	Dissociation E from DFT (eV)	Activation energy, E_0 (eV)
$[AE-H]^+$	4.6	4.44 ± 0.56
$[AL-H]^+$	3.43	2.85 ± 0.56
$[AE-H_2]^+$	4.8	4.46 ± 0.62
$[AE-2H]^+$	8.55	7.94 ± 0.86
$[AL-2H]^+$	5.39	5.2 ±1.42

In the TOF experiments, AL^+ is confirmed to dissociate at lower energies than AE^+, for all the channels at play. Interestingly, the derived activation energies for the loss of H and H_2 in AE^+ (4.44 eV and 4.46 eV respectively) are in good agreement with the ones calculated by DFT, *i.e.*, 4.6 and 4.8 eV respectively. For the sequential loss of 2 H, the values derived from the RRKM analysis of iPEPICO are around 1.2 eV lower than those obtained through DFT (7.94 eV *versus* 8.55 eV for the most energetically favorable combination), which can still be considered to lay within the error bars.

On the other hand, we only see H and H+H loss for AL^+ in the current experiment. Although with a higher discrepancy, the iPEPICO and DFT results of H loss are still in agreement (2.85 ± 0.56 *versus* 3.43 eV respectively), while in this case the energetics involved in the loss of 2H are more similar (~5.2 *versus* 5.39 eV respectively for iPEPICO and DFT calculations). It is important to mention that we do not see the loss of molecular hydrogen in AL^+, which suggests that this is indeed a slower mechanism, and thus is not observable on the energy and time scale of iPEPICO. This is in good agreement with the DFT results explained on section 5.2.3, where we obtained a low transition state barrier for the migration of a hydrogen in a sp^3 carbon towards an adjacent carbon. This suggests that if the molecule has enough internal energy to overcome the first hydrogen migration, subsequent migrations can occur before dissociation is achieved, increasing the time required for this channel.

6.5.2 Comparison of threshold energies with ion trap results

In Chapter 4 (Figure 4-7) we presented the internal energies of the parent ions at which we observed the opening of the H loss and $2H/H_2$ loss channels in the ion trap experiments at SOLEIL. These threshold energy values are reminded in Table 6-3. In order to compare them with the threshold energies derived from iPEPICO experiments, we must translate the photon energies displayed in Figure 6-3 and Figure 6-4 into the internal energies of the molecular parents, simply by removing the corresponding ionization potential mentioned in section 6.2. (*i.e.*, 7.11 eV for AE^+ and 7.05 eV for AL^+). The threshold energies obtained from both experiments are shown in the following table:

Table 6-3 Comparison of the threshold internal energies for the main dehydrogenation channels observed in SOLEIL and iPEPICO experiments.

	$E_{Threshold}$ (eV)	
	SOLEIL	*iPEPICO*
$[AE - H]^+$	10.2 ± 0.2	11.1 ± 0.1
$[AL - H]^+$	<8 ± 0.1	8.8 ± 0.1
$[AE - 2H/H_2]^+$	10.8 ± 0.2	12.4 ± 0.1
$[AL - 2H/H_2]^+$	9.3 ± 0.1	10.3 ± 0.1

The comparison of these values shows the relevance of kinetic shift induced by the different timescales involved in the two experiments. In the ion trap the molecules are confined for longer timescales, and so the energy needed to open a channel is lower than in iPEPICO, where the reaction has to occur during the available time of flight and therefore at shorter timescales. It is worth pointing out that this energy difference is found to be around 1 eV in all cases, and it typically increases with increasing threshold energy. The largest energy difference between experiments corresponds to the loss of two hydrogens from AE^+, which can be related to the higher energy needed for the dissociation to occur.

6.5.3 Comparison of dissociation rates

The dissociation rates calculated through RRKM modelling of the iPEPICO results have been presented in Figure 6-5. In our TOF experiments, the characteristic times are in the order of 0.1 ms, which implies that dissociation rates in the order of 10^4 s^{-1} are needed in order to observe any fragmentation. At such rates, the loss of H from the parent cation occurs at an internal energy of approximately 9.1 eV for AL^+ and 12.3 eV for AE^+. This energy difference of around 3.2 eV is approximately constant for all the dissociation rates. On the other hand, for the loss of H from the dehydrogenated daughter cations, we see that the difference between the k_{diss} of $[AL\text{-}H]^+$ and $[AE\text{-}H]^+$ evolves as a function of their internal energy. Initially, $[AL\text{-}H]^+$ would start dissociating at lower internal energies than $[AE\text{-}H]^+$. When increasing in internal energies, other H loss channels will enter in competition leading to higher dissociation rates for $[AE\text{-}H]^+$ compared to $[AL\text{-}H]^+$.

Additionally, from the MD/DFTB results we can derive dissociation rates at high internal energies. In Figure 6-7b) we observe that at 26 eV, the loss of H from AL^+ starts at 400 ps, from which we can derive a dissociation rate of $2.5 \cdot 10^{+9}$ s^{-1}. In the case of AE^+, the loss of H occurs at 100 ps at 28 eV, which corresponds to a dissociation rate of 10^{+10} s^{-1} at such energy. Adding these two points to the values presented in Figure 6-5, we can obtain a qualitative comparison between the dissociation rates derived from the MD/DFTB calculations (squares), at very short timescales, with those derived from the iPEPICO experiment (lines), at longer timescales. Figure 6-12 confirms that the results from these two approaches are qualitatively consistent.

Finally, this figure also includes two points corresponding to the threshold energies obtained in the ion trap in the SOLEIL campaign (see Figure 4-7a). The corresponding dissociation rates, following the RRKM calculated curves, are found to be < 350 s^{-1} for AL^+ (for which we missed the threshold) and 20 s^{-1} for AE^+. These values reflect the long timescales in the ion trap with some limitation due to the cooling through collisions with He atoms (IR cooling is expected at a rate of about 10 s^{-1} according to Montillaud et al. (2013)).

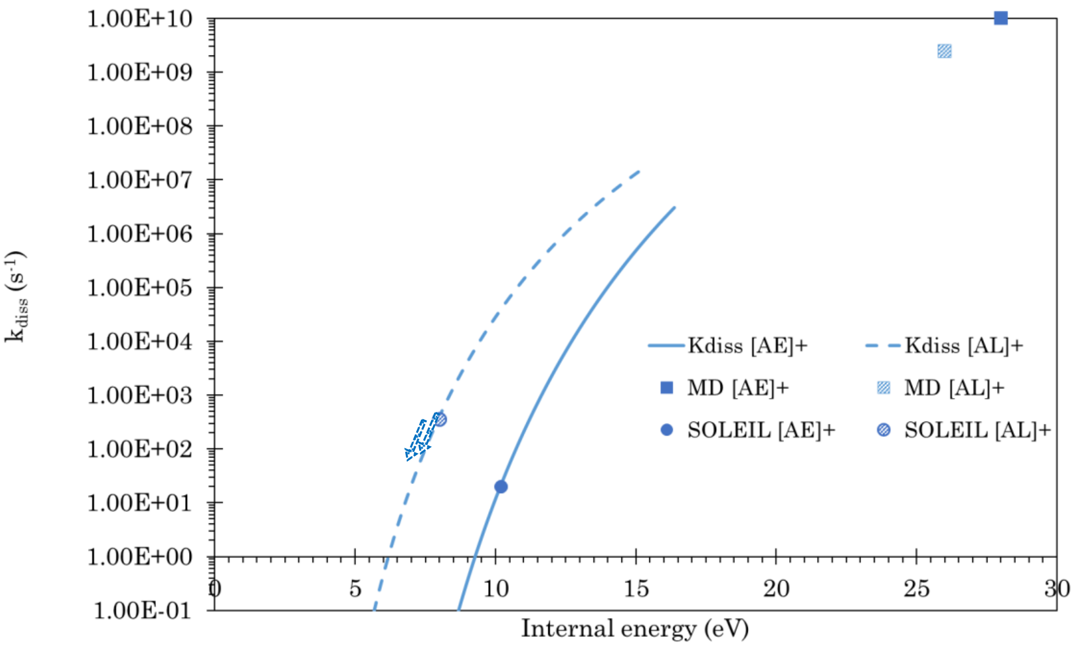

Figure 6-12 Comparison of the dissociation rates as a function of the internal energy obtained through RRKM fitting of the iPEPICO experiments (lines) and MD calculations (squares) for the loss of H from the parent cation. Also added on the figure are the threshold energies measured in the SOLEIL experiments (dots) for such fragmentation pathway. The arrow points towards lower dissociation rates corresponding to the actual threshold of H loss from AL$^+$, which we missed. Full figures represent [AE]$^+$ and dotted figures represent [AL]$^+$.

6.6 Summary and discussion

In this chapter, we presented results related with the dynamics of the dissociation of PAHs as a function of their internal energy. On the one hand, the activation energies of AE$^+$ and AL$^+$ obtained in iPEPICO studies are reported. They show an overall agreement with dissociation energies previously calculated through DFT. Furthermore, we observe that dissociation occurs at higher internal energies in the TOF experiments than in the ion trap experiments, which is associated with the kinetic shift due to experimental timescales. In addition, we report here the kinetic shift as a function of the carbon number for a set of PAHs (Figure 6-2), showing that it is more pronounced as the size of the molecule – and thus the number of degrees of freedom – increases. For larger molecules, more energy will be needed to initiate the dissociation because the energy is statistically distributed into more non-dissociating vibrational modes that must be explored before a reaction occurs.

On the other hand, we explored through MD/DFTB a few other structural rearrangements that lead to fragmentation. These calculations not only confirm the need of less energy to fragment AL^+ than AE^+ but also the higher tendency of AL^+ to lose $2H/H_2$ – let us recall that we obtain no $2H/H_2$ fragments for AE^+ at 30 eV of internal energy, while they are already present at 26 eV for AL^+. This 4 eV difference in the loss of $2H/H_2$ is far from the one observed in the ion trap experiments. It is important to realize that kinetic shift will be significant at such high internal energies: the higher the energy barrier, the more additional energy should be given for dissociation. However, the higher internal energies involved in MD/DFTB make a direct comparison with such experiments difficult. MD/DFTB simulations are probably more appropriate to rationalize the results of some high energy collision experiments (Gatchell et al. (2015); Simon et al. (2018)). From these MD/DFTB simulations, we have also calculated characteristic dissociation rates, and they are in reasonable agreement with an extrapolation of the RRKM curve to high energies.

Finally, as we have already mentioned, the H/H_2 loss may be overestimated with respect to C_2H_2 loss in the MD/DFTB simulations. Interestingly, most of the dehydrogenation pathways in AL^+, especially at lower energies, involve the formation of a 5-member ring, which we had previously obtained in our calculations at the DFT level of theory. This illustrates the usefulness of both approaches that appear complementary to get insight into dissociation paths and mechanisms for such complex systems as PAHs.

Chapter 7: GENERALIZATION TO MEDIUM-SIZED PAHS, ASTROPHYSICAL IMPLICATIONS

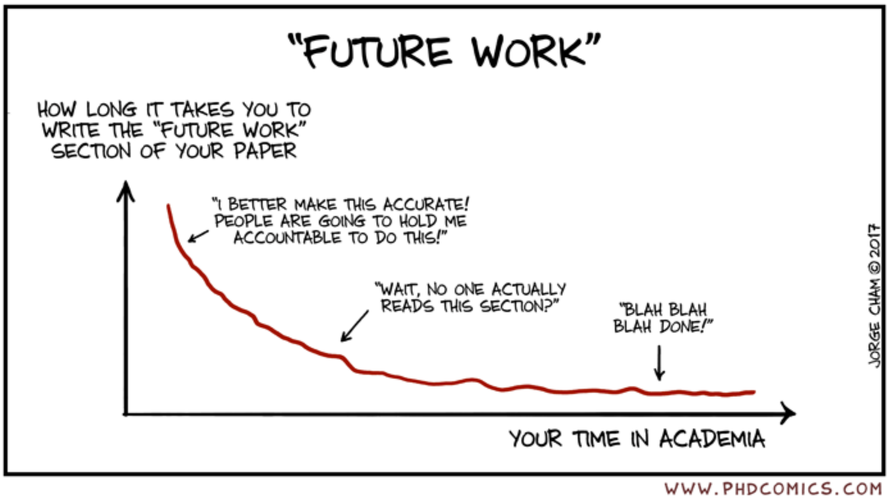
"FUTURE WORK"
HOW LONG IT TAKES YOU TO WRITE THE "FUTURE WORK" SECTION OF YOUR PAPER
"I BETTER MAKE THIS ACCURATE! PEOPLE ARE GOING TO HOLD ME ACCOUNTABLE TO DO THIS!"
"WAIT, NO ONE ACTUALLY READS THIS SECTION?"
"BLAH BLAH BLAH DONE!"
YOUR TIME IN ACADEMIA
JORGE CHAM © 2017
WWW.PHDCOMICS.COM

7.1 Introduction 112
7.2 Ionization *versus* fragmentation of medium-sized PAHs .. 112
7.3 Activation energies of small and medium-sized PAHs 116
7.4 A new possible route for H_2 formation 120
Conclusions [En] ________ 123

7.1 Introduction

In this manuscript, we have presented a detailed view on the interaction with VUV photons and energetics of two isomers of the dibenzopyrene cation. This work combines experimental data obtained at synchrotron facilities (SOLEIL and SLS) with computational work using DFT calculations, RRKM modelling and MD simulations. This study gives us some insight into the impact of the PAH structure on stability and dissociation pathways. Additionally, information about the effect of PAH size can also be retrieved from our experimental campaigns, in which a set of smaller PAHs were studied, which samples a range of sizes from 10 to 24 carbon atoms. All these results are summarized in this chapter.

The yields of ionization and dissociation are first discussed, including our work published in Zhen et al. (2016). They are relevant to the stability of PAHs in astrophysical environments. In particular the ionization yield is related to the contribution of these species to the heating of the gas by photoelectric effect. We next move to the energetics approach of fragmentation pathways as a function of PAH size, based on the iPEPICO data as given in our article (West et al. 2018), in which the importance of both types of carbon (sp^2 *versus* sp^3) in the dissociation energies is highlighted. Finally, we detail the ion trap results we obtained for coronene in order to support our theory of a possible new H_2 formation mechanism.

7.2 Ionization *versus* fragmentation of medium-sized PAHs

The results presented in this section correspond to a campaign at SOLEIL, and have been reported in Zhen et al. (2016b). The molecular ions under study span over a range of sizes and structures (see Figure 7-1), being: anthracene ($C_{14}H_{10}^+$), pyrene ($C_{16}H_{10}^+$), tetracene ($C_{18}H_{12}^+$), perylene ($C_{20}H_{12}^+$), benzo[g,h,i]perylene ($C_{22}H_{12}^+$), coronene ($C_{24}H_{12}^+$), and the already introduced dibenzo[a,l]pyrene and dibenzo [a,e]pyrene ($C_{24}H_{14}^+$).

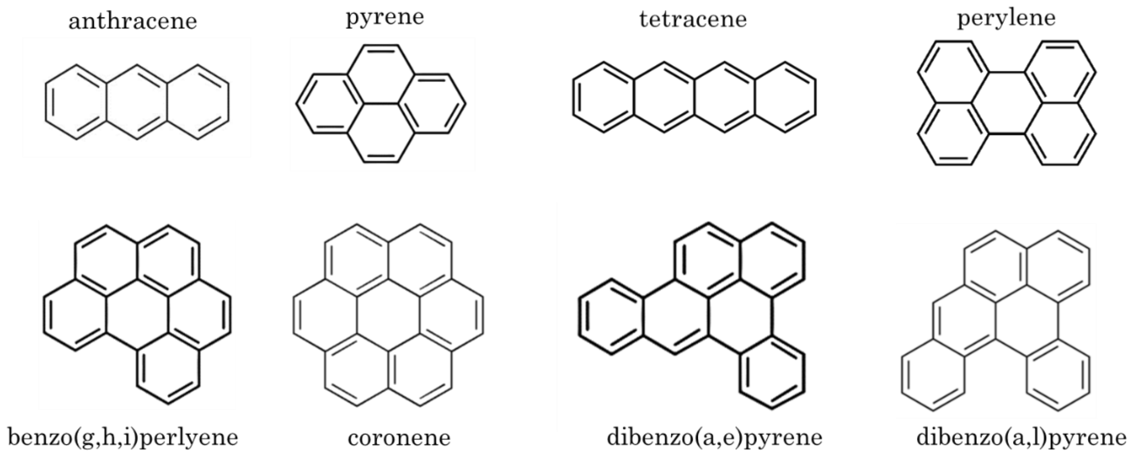

Figure 7-1 Schematic drawings of the eight molecules of the ion trap campaign. From left to right and top to bottom: anthracene ($C_{14}H_{10}$), pyrene ($C_{16}H_{10}$), tetracene ($C_{18}H_{12}$), perylene ($C_{20}H_{12}$), benzoperylene ($C_{22}H_{12}$), coronene ($C_{24}H_{12}$), dibenzo(a,e)pyrene ($C_{24}H_{14}$), dibenzo(a,l)pyrene ($C_{24}H_{14}$).

The aim of this study was to quantify the yields of fragmentation and ionization of PAH cations of different sizes in order to provide data to model accurately the abundance of PAHs in different ionization states. As we saw in Chapter 1, PAHs are expected to be found in different charge states in the ISM but so far the ionization yield used in astronomical models relies on the works of Verstraete et al. (1990) and Jochims et al. (1996) for neutral PAHs. Moreover, charge also has a profound effect on the IR spectral characteristics of PAHs (Bakes et al. 2001b; Malloci et al. 2007b) as well as on its electronic absorption spectrum (see *e.g.*, Cecchi-Pestellini et al. 2008). Therefore, it is of interest to consider all possible charge states that PAHs can experience in astrophysical environments.

The ionization yield of these PAH cations was obtained under a similar assumption as in Chapter 4. Briefly, we rely on the close similarity between the photo-absorption cross sections obtained theoretically by Malloci et al. (2004), (2007a), and the sum of all the photo-events in our experimental setup (fragments + doubly ionized) as reported in Zhen et al. (2016b) and illustrated in Figure 7-2 for pyrene, tetracene, perylene and benzoperylene as an example.

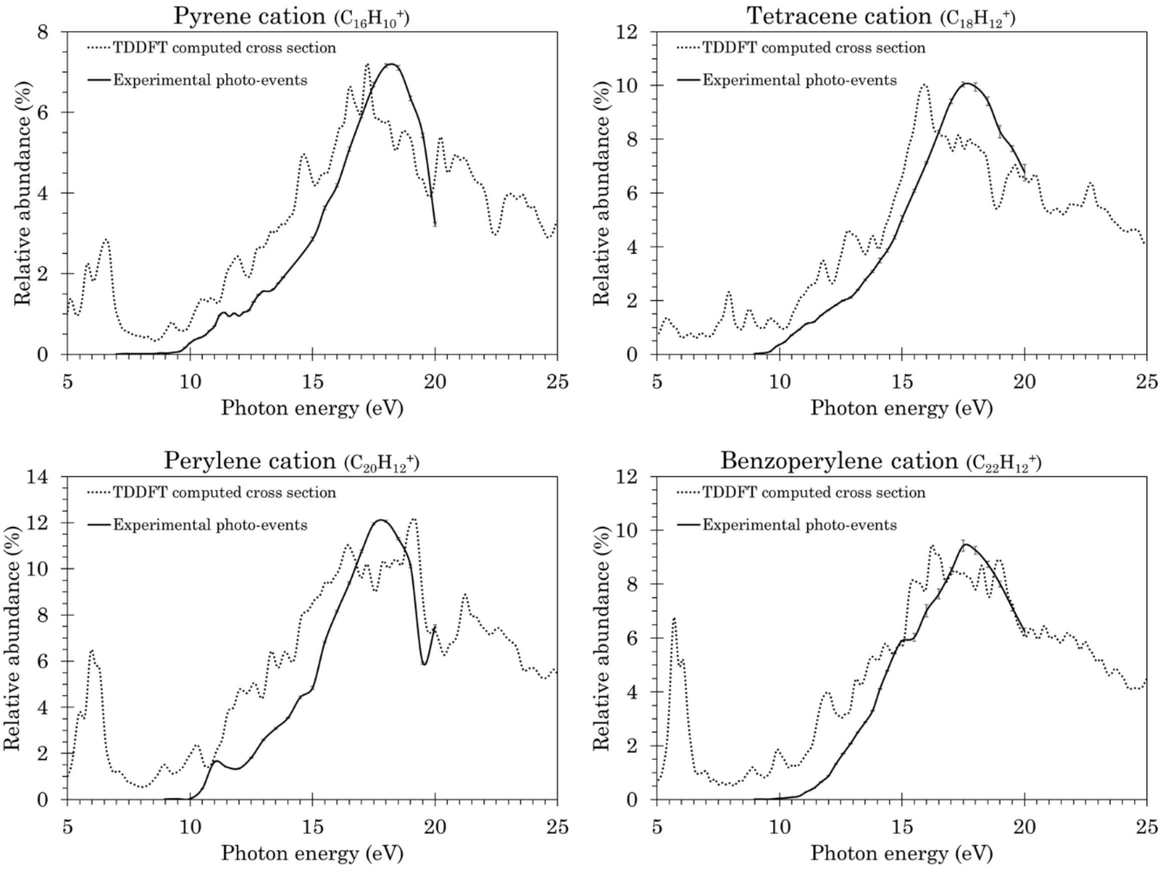

Figure 7-2 Values of the relative intensity of the photo-products of different PAHs (full black lines) submitted to VUV photons as a function of photon energy. Theoretical cross sections calculated by Malloci et al. (2004), (2007a) are shown in grey dotted lines.

We can derive two trends from these yields, shown in Figure 7-3. First, for a given photon energy the ionization yield increases with increasing PAH size, especially in the range from the second ionization potential (IP2) to ~13.6 eV. This yield increases more smoothly for the smaller molecules, while in the bigger ones we see a steep jump between IP2 and 12 eV. This can be accounted for by their photo-fragmentation dynamics (Jochims et al. (1994)). A larger species (with higher number of vibrational modes) will need a higher internal energy to reach the same level of excitation in a given bond if this internal energy is distributed statistically. In addition the value of IP2 decreases with PAH size (Malloci et al. (2007b)). A point must be made for the ionization yields of the two dibenzopyrene isomers, clearly different at low photon energies. Even though the ionization cross sections of both molecules are similar, the photo-fragmentation cross sections are not, as we have seen throughout this work (in

Chapter 4). This translates in the importance of the specific structure of the PAH on the ionization yield at low energies.

Second, the ionization yield is relatively independent of the size and structure of the PAH cations in the high energy range (≥ 15 eV); for all the molecules this yield shows a gradually increasing behavior up to around 0.9 at ~18 eV, consistent with the values previously reported by Zhen et al. (2015) on the larger PAH cations ovalene ($C_{32}H_{14}^+$) and 'HBC' ($C_{42}H_{18}^+$).

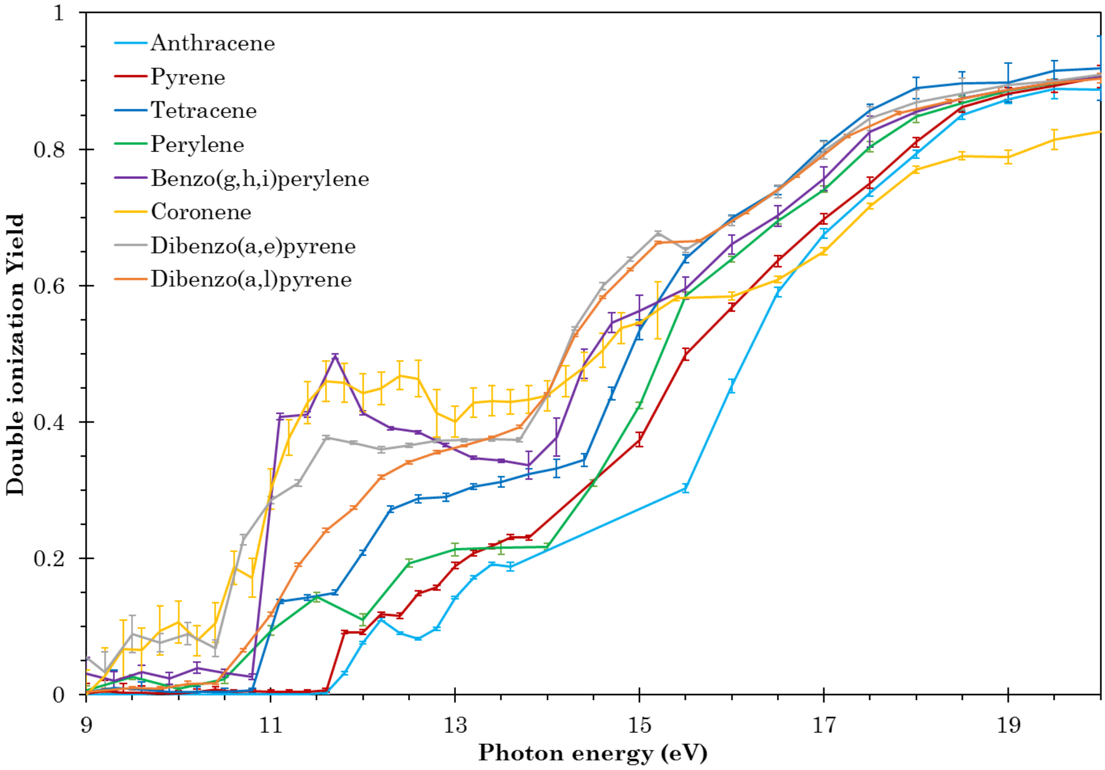

Figure 7-3 Photoionization yields of PAH cations as a function of incident photon energy in the 8-20 eV range, including error bars.

The relevance of these results resides on the clear need to include information on cations and doubly-charged PAHs in the astrophysical models, especially due to the effect of charge on the IR spectral characteristics of these molecules. For this reason, we provide in Zhen et al. (2016b) first experimental data on the ionization yields of a set of medium-sized PAH cations. In particular, the ionization yield obtained in this work for coronene cation is compared to that of neutral coronene from Verstraete et al. (1990) in Figure 7-4. They display similar trends, aside from the obvious shift due to different IPs. However, ionization yields of larger species than coronene are needed and have not yet been obtained. Let us recall that only PAHs containing more than ~50 carbon atoms are expected to be stable in the ISM (Montillaud et al. (2013)).

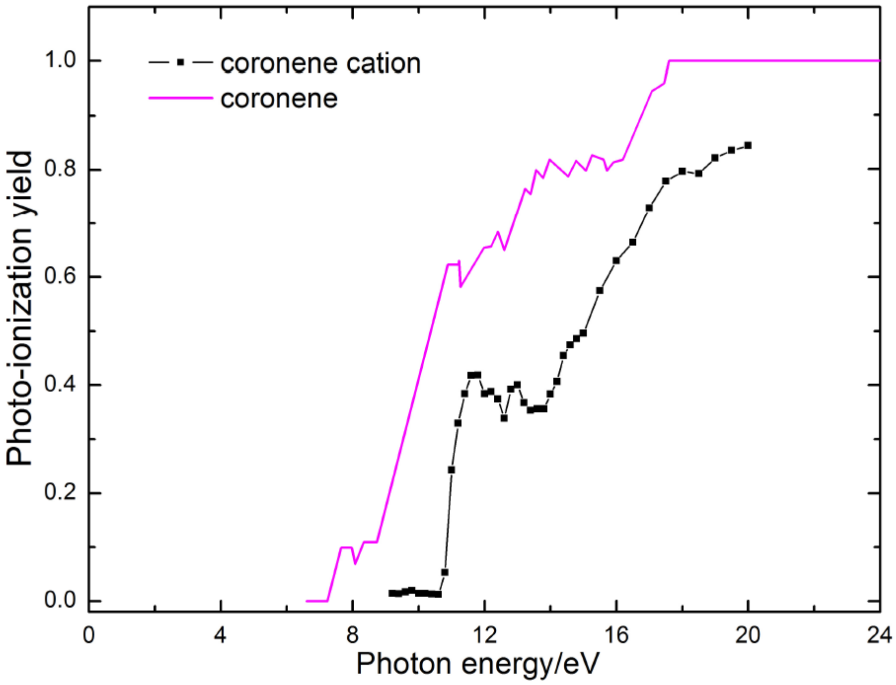

Figure 7-4 Comparison between the photo-ionization yield of coronene neutral (Verstraete et al. (1990)) and cation (this work, Figure 7-3).

7.3 Activation energies of small and medium-sized PAHs

In addition to the results reported in Chapter 6 on activation energies of the dehydrogenation of the dibenzopyrene isomers, we also studied the unimolecular dissociation of eight more PAH molecules in iPEPICO experiments with the aim of establishing clear, experimentally-derived trends in the reaction energies over a wide range of sizes. These molecules were: acenaphthylene ($C_{12}H_8$), fluorene ($C_{13}H_{10}$), cyclopenta[d,e,f]phenanthrene ($C_{15}H_{10}$), fluoranthene ($C_{16}H_{10}$), pyrene ($C_{16}H_{10}$), corannulene ($C_{20}H_{10}$), perylene ($C_{20}H_{12}$) and coronene ($C_{24}H_{12}$). The ion structures of pyrene, perylene, coronene and the dibenzopyrene isomers were shown previously in Figure 7-1. Figure 7-5 shows the 2D representations of the five molecules that have not been previously presented, all of which present a 5-member ring in their structures.

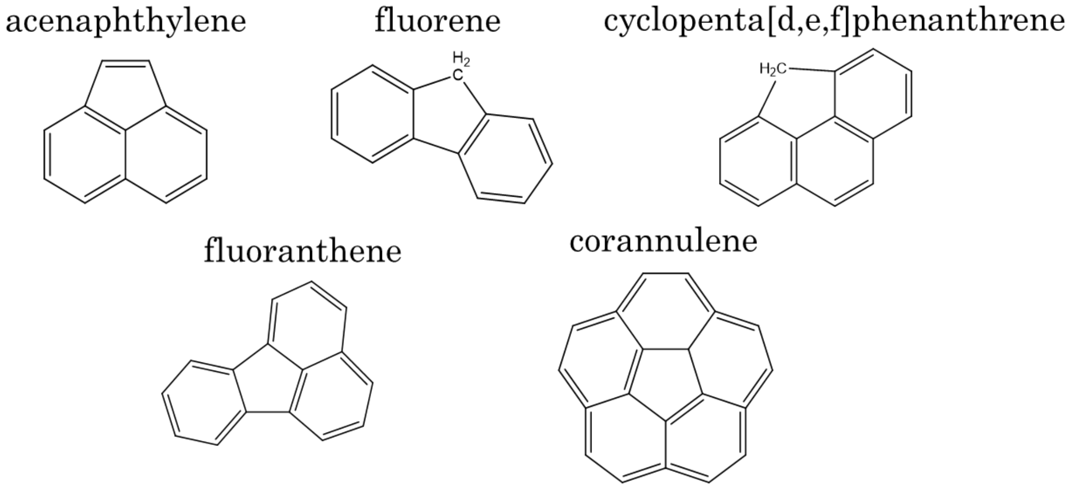

Figure 7-5 Schematic figures of five of the molecules studied on the iPEPICO test campaign. The remaining five are shown in Figure 7-1.

In total, 25 different fragmentation reactions were observed and fit using RRKM modelling (see West et al. (2018) for the detailed results and breakdown curves) for these ten molecules. Fluorene and cyclopentaphenanthrene present a sp^3-carbon center, similarly to other two PAHs studied previously by the group of Prof. P. Mayer: dihydronaphthalene ($C_{10}H_{10}$) and dyhydrophenanthrene ($C_{14}H_{12}$) (West et al. (2014a)). The results on the activation energies of the dehydrogenation reactions of the latter two molecules are combined with the ones obtained in West et al. (2012) for naphthalene and those from this campaign. They are presented in Figure 7-6 as a function of PAH size (from 10 – dihydronaphthalene and naphthalene – to 24 carbon atoms – coronene and the dibenzopyrene isomers).

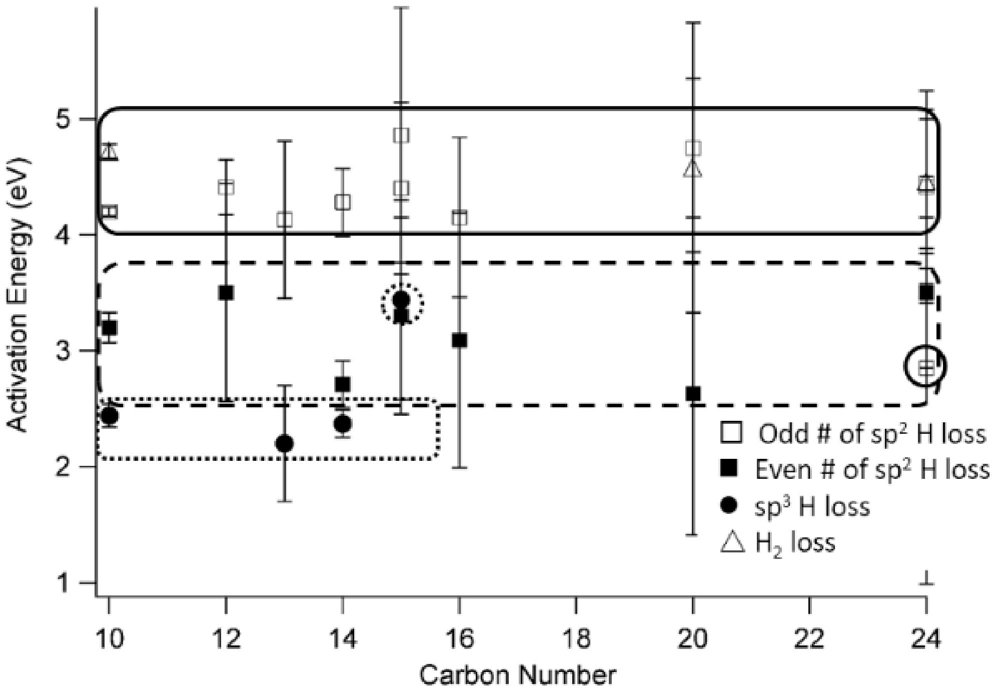

Figure 7-6 Activation energy as a function of carbon number for the dehydrogenation reactions from naphthalene (C10) to coronene (C24). Outlines highlight the three trends observed. The distinctively low values obtained for the single loss of H from a sp² carbon of AL⁺ are shown in the full circle.

As we can see, the reaction energies for the dehydrogenation of PAH cations are independent of the PAH size as well as of their structure (catacondensed *versus* pericondensed), However, they are related to the number of unpaired electrons in the molecule. For the molecules with at least one sp^3-C center, the loss of H from this site is always the lowest channel in energy, as the molecule tends to regain the stability associated with a normally-hydrogenated PAH. The average activation energy associated with this channel is 2.34 eV, not including the one obtained for cyclopenta[d,e,f]phenanthrene (CPP) ions, for which the E_0 was 3.44 ± 0.86 eV due to steric constraints. Single H loss from an sp^2-C center is the only reaction observed in all cases, occurring at ≈ 4.4 eV for all the molecules except dibenzo(a,l)pyrene, due to its unique structure (see Chapter 5) and marked with a full circle in Figure 7-6. The activation energy for the second hydrogen loss (from this daughter precursor) from a sp^2-C center falls typically in the 2.8-3.5 eV range, indicating that the ions gain stability from the pairing of unsaturated sites through the formation of a triple bond. This “even-odd” - alternating higher and lower- activation energy pattern has been previously observed in earlier studies of the dissociation of ionized coronene and pyrene (Montillaud et al. (2013); West et al. (2014c) respectively). Finally, H_2 loss was only observed in iPEPICO experiments for perylene and dibenzo(a,e)pyrene at energies of around 4.5 eV. These two molecules present the highest number bay structures in their structure (not taking into account the special case of dibenzo(a,l)pyrene), suggesting that molecular hydrogen loss could be facilitated by the geometry.

Additionally to dehydrogenation we observe minor loss of hydrocarbons from the smaller molecules, such as acenaphtylene, fluorene, fluoranthene, cyclopentaphenanthrene and naphthalene. The activation energy of acetylene, the most commonly lost hydrocarbon from the precursor cation, falls at around ~4.16 eV. A similar energy value is obtained by averaging the loss of C_4H_2, however only seen in naphthalene and fluorene-H. The last observed fragment is the loss of methyl from the dihydro-PAHs (West et al. (2014a)). The energy required for the proposed isomerization and dissociation is on average 2.48 eV.

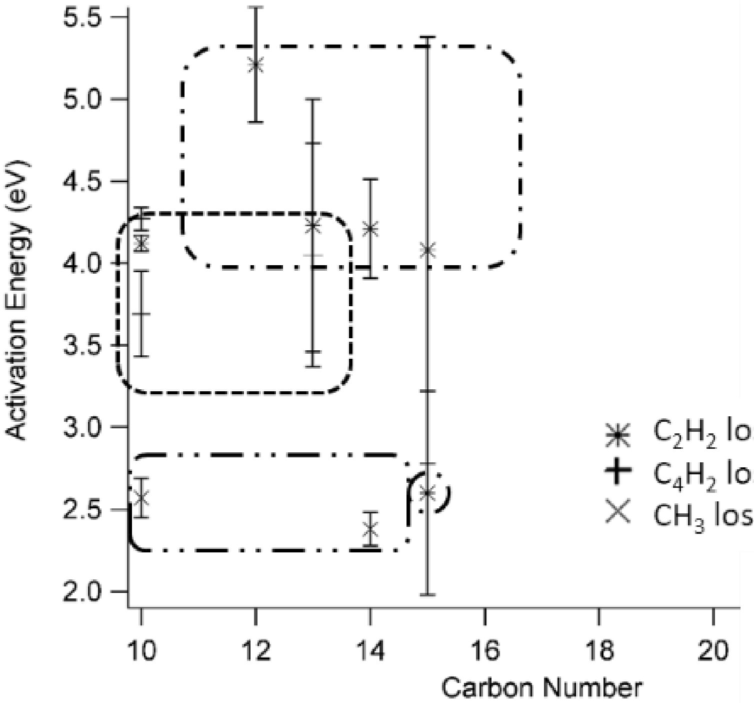

Figure 7-7 Trends for hydrocarbon fragment loss as a function of carbon number. Some results from previous work by the group of Prof. P. Mayer were included for completeness.

Finally, from these iPEPICO experiments and the corresponding RRKM simulations, the role of the kinetic shift related with molecule size in these systems is highlighted. As we had seen in Figure 6-12, the energy needed to dissociate the precursor ions increases significantly with the number of carbon atoms, *i.e.*, with the size of the PAH. For example, for naphthalene ($IP_{naphthalene} = 8.14\ eV$) photon energies of approximately ~15.5 eV are enough to see at least 20% of $[M\text{-}H]^+$ daughter ions. However, 21 eV-photons are needed to see 20% of the coronene parent ions dissociating into $[M\text{-}H]^+$ ($IP_{coronene} = 7.29\ eV$). With this, we confirm the statistical character of the dissociation of PAHs: the internal energy is statistically distributed over all the vibrational modes before dissociation. This directly implies that, the larger the PAH, the more additional energy will be needed to fragment it, and that, in turn, larger PAHs are expected to survive longer after the incidence of an VUV photon, in line with the results of the astrophysical model by Montillaud et al. (2013).

7.4 A new possible route for H_2 formation

The role of PAHs as catalysts for H_2 formation has been the focus of several studies in relation with the astrophysical context. Experimental studies on compact PAH cations such as pyrene and coronene have concluded that photodissociation mainly proceeds by sequential H loss (West et al. 2014c, Montillaud et al. 2013). Chen et al. (2015) report the potential importance of H_2 loss but at higher energies than the threshold observed for H loss. Other mechanisms have been proposed that would be more favorable for the formation of H_2 by PAHs, all involving the adsorption of at least one H atom. The Eley-Rideal mechanism considers first that a gas-phase hydrogen is attached to a PAH, preferably on an edge site, and is then abstracted by a passing-by H, forming H_2 (Hirama et al. (2004); Rauls & Hornekær (2008)). However models that incorporate this process in the chemical evolution of PAHs have concluded that it does not provide a major contribution to the formation of H_2 (Boschman et al. (2015); Andrews et al. (2016)). This brings back the possibility of photodissociation of PAHs being a potentially attractive mechanism to contribute to the formation of H_2 in PDRs and calls for a better quantification of this process in laboratory experiments (Andrews et al. (2016)).

A major result of our study on the dibenzopyrene isomer cations is to provide an H_2 formation pathway, which would lead to an easier route for H_2 formation in the case of non-compact PAHs containing bay regions, based on the study of AE^+ and AL^+. The experimental and theoretical results for AE^+, shown on

Chapters 4 and 5 respectively, can only be reconciled at low photon energies if the mechanism driving the loss of two hydrogens in these PAHs is indeed the loss of H_2. In contrast, similar studies carried out on coronene ($C_{24}H_{12}^+$), a similar-sized molecule with a compact structure and no bay sites, indicate that the double dehydrogenation mechanism is energetically compatible with two sequential H losses. The relative abundance of the dehydrogenated species as a function of incident photon energy, obtained from our campaign at SOLEIL, is shown in Figure 7-8. The onset energies for the loss of one and 2 hydrogens are 10.0 ± 0.1 and 12.8 ± 0.1 eV respectively, obtained in the same fashion as those previously reported for AE^+ and AL^+.

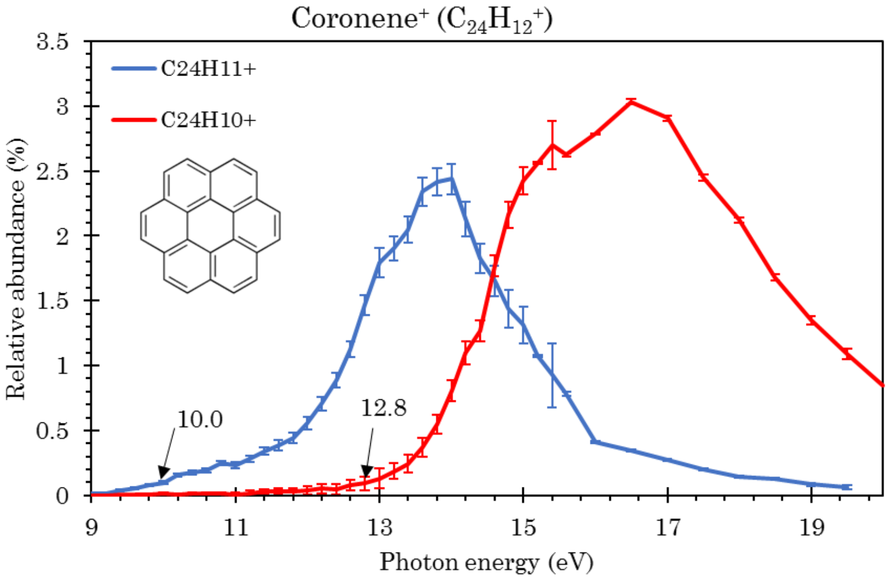

Figure 7-8 Abundances of the photo-dehydrogenation fragments of coronene cation ($C_{24}H_{12}^+$) as a function of the VUV photon energy. The values are normalized to the total number of trapped ions. Blue represents the loss of a single H atom ($C_{24}H_{11}^+$) and red represents the loss of 2H/H_2 ($C_{24}H_{10}^+$). Minor (< 0.2%) losses of 3 and 4 hydrogens observed in the experiment are not shown for clarity.

Assuming a dissociation energy of ~ 4.4 eV for the C-H bond and having into account that the loss of the second hydrogen requires less energy than the first (~ 3.2 eV) (see Figure 7-6 and West et al. (2018)), we conclude that the experimental onset energy for the double dehydrogenation of coronene is compatible with sequential 2H loss. These conclusions suggest a possible relationship between the presence of bay hydrogens and the loss of H_2, which should be further studied.

Conclusions [En]

The study presented in this work can be regarded as a first step towards the exploration of the interaction of PAH cations with VUV photons, in order to get further insights into their evolution in astrophysical environments. This interaction has been investigated through laboratory experiments using iPEPICO and ion trap setups, both installed on synchrotron facilities in order to benefit from the wide of photon energy ranges that they provide, in particular in the VUV range.

On the one hand, ion trap experiments allowed us to derive the ionization yield of several medium-sized PAH cations. These should then be input to astronomical models for a more precise description of the charge state of PAHs (Montillaud et al. (2013)) and their contribution to the heating of the gas in the ISM through the photoelectric effect (Bakes & Tielens (1994)). Additionally, the branching ratios between different fragmentation channels were measured. However, dissociation rates cannot be derived directly from the information obtained in this technique.

On the other hand, we explored the evolution of these molecules after the absorption of VUV radiation on a iPEPICO setup. The RRKM fitting of the obtained breakdown curves allowed us to obtain activation energies and entropies. Our results show that H loss is the only channel that is always present in the set of PAH cations under study (West et al. (2018)), being the lowest dissociation channel for the medium-sized molecules. For smaller molecules such as the naphthalene cation ($C_{10}H_8^+$), the lowest channel is the loss of C_2H_2. Furthermore, we obtained trends on dependence of the activation energy of H loss on the number of hydrogens lost (one or two) in the fully aromatic molecules, and the effect of sp^3-C center in PAHs with aliphatic sites. The increase in threshold energies as a function of the PAH size was also highlighted, confirming the statistical behavior of the distribution of the internal energy over all the vibrational modes before dissociation. These conclusions indicate that larger PAHs are expected to survive longer after the incidence of an astro-VUV photon, in agreement with astronomical models (*e.g.* Montillaud et al. (2013)). These models can also benefit from the dissociation rates that we have obtained from the activation parameters. Finally, a comparison of threshold dissociation energies obtained from ion trap experiments and iPEPICO experiments shows the importance of the kinetic shift due to the different timescales available in these experiments. The time-of-flight technique requires photo-events to occur during ~100 μs timescale in order to be detected. For this reason, higher photon energies than the ones involved in the ion trap are required which implies that not all fragmentation channels might be open at such short timescales. There is a clear complementarity between both experiments: ion trap experiments at long timescales provide more complete branching ratios while iPEPICO experiments provide useful dissociation rates.

This work also brings attention to the importance of the PAH structure through a study on two isomers of the dibenzopyrene molecule. The experimental results obtained with the above-mentioned techniques indicate that the isomer presenting a non-planar structure due to a steric hindrance photodissociates at lower energies than the planar one. This was confirmed by our results from DFT calculations and MD simulations, which suggest that the special geometry of the non-planar molecule favors the dehydrogenation from the sterically hindered sites, leading to the formation of a 5-member ring. DFT allowed us to study in detail the energetics involved on specific fragmentation pathways, while we were able to obtain quantitative statistical dissociation results through the exhaustive exploration of the potential energy surfaces thanks to MD. This approach, however, overestimates the loss of carbon-related fragments and underestimates the loss of H_2; therefore further benchmarking with experimental results should be carried out.

Additionally, a major result of our study on these isomeric cations is to provide a new route for H_2 formation in the case of non-compact PAHs containing bay regions. Indeed, our experimental and theoretical results can only be reconciled at low photon energies if the mechanism driving the loss of two hydrogens in such PAH cations is indeed H_2 loss, rather than H+H loss, assuming statistical distribution of the internal energy. This result is consolidated through the comparison with the coronene cation, a compact PAH containing also 24 carbon atoms, but with no bay-areas. The role of PAHs as catalysts for H_2 formation has been the focus of several studies in relation with the astrophysical context. Experimental studies on compact PAH cations such as pyrene and coronene have concluded that photodissociation mainly proceeds by sequential H loss, while H_2 loss is only potentially relevant at high energies. Other mechanisms have been proposed that would be more favorable for the formation of H_2 by PAHs, all involving the adsorption of at least one H atom, such as the Eley-Rideal mechanism. However, models that incorporate this process in the chemical evolution of PAHs have concluded that it does not present a major contribution to the formation of H_2. This brings back the possibility of photodissociation of PAHs being a potentially attractive mechanism to contribute to the formation of H_2 in PDRs and calls for a better quantification of this process in laboratory experiments.

Following the results of this thesis, the effect of bay hydrogens should be further investigated and considered while modeling the formation of H_2 in photodissociation regions. Therefore, further experimental and theoretical investigations should be carried out on similar molecules – presenting bay hydrogens –. Two examples of such molecules are naphtho[8,1,2-ghi]chrysene and benzo[c]naphtho[8,1,2-ghi]chrysene; their structures are presented in Figure II in the Annex. The first one has the same formulation as the isomers presented in this thesis but different geometry, and therefore would be an ideal candidate to compare with the results presented here. The second one has four carbon atoms more but a hindered structure similar to the one presented in this work. The effect of this type of structures and their evolution under VUV irradiation should be further addressed using similar experimental techniques and theoretical tools as those used in the present manuscript.

Finally, all these conclusions should be contrasted with data from much larger species, since the astrophysical models predict that mainly large PAHs (with 50 carbon atoms or more) survive in the PDRs. For this reason, it is necessary to quantify the effects that size might have on the processes studied in this work: ionization and fragmentation. However, it is important to have in mind that we would rely mostly on laboratory experiments since theoretical calculations cannot account for excited states and, moreover these large sizes would require computational times that are prohibitive.

Conclusions [Fr]

L'étude présentée dans ce manuscrit est une première étape dans l'exploration de l'interaction de cations de PAH avec des photons VUV afin de mieux comprendre l'évolution de ces molécules dans les milieux astrophysiques. Cette étude a été menée en utilisant à la fois un dispositif d'imagerie de photoélectrons-photoions en coïncidence (iPEPICO) et un piège à ions. Ces deux dispositifs sont couplés au rayonnement synchrotron ce qui permet d'accéder à des photons accordables dans le domaine VUV.

Dans les expériences de piège à ions nous avons étudié le rendement d'ionisation de différents cations de PAH, donnée qui peut être utilisée dans les modèles astrophysiques pour décrire l'évolution de la charge des PAH (cf. Montillaud et al. (2013)*)* et leur impact sur le chauffage du gaz par effet photoélectrique (Bakes & Tielens (1994)). Les rapports de branchement entre les voies de dissociation ont été mesurés. Cependant, les taux de dissociation ne peuvent pas être dérivés directement des informations obtenues avec cette technique.

D'autre part, nous avons exploré l'évolution de ces molécules suite à l'absorption d'un photon VUV avec un dispositif iPEPICO. L'ajustement des données expérimentales avec un modèle RRKM nous a permis d'obtenir des énergies et des entropies d'activation. Nos résultats montrent que la perte de H est le premier canal de dissociation pour les PAH de taille moyenne (10-24 atomes de carbone) étudiés dans West et al. (2018). Pour le cation de naphtalène ($C_{10}H_8^+$), la perte de C_2H_2 est le canal le plus bas. Pour la perte de H, nous avons obtenu l'énergie d'activation correspondant à la perte du premier et du deuxième hydrogène pour une molécule complétement aromatique. Une énergie a également été dérivée pour des sites aliphatiques (sp^3). L'augmentation du seuil de dissociation avec la taille des PAH a été mise en évidence, ce qui confirme le caractère statistique de la dissociation, l'énergie se redistribuant sur l'ensemble des modes accessibles. Ces résultats impliquent que les PAH de plus grande taille doivent survivre plus longtemps dans les milieux astrophysiques où ils sont exposés aux photons UV, en accord avec les modèles astrophysiques (Montillaud et al. (2013)). Ces modèles peuvent aussi bénéficier des taux de dissociation et paramètres d'activation que nous avons obtenus. Finalement, la comparaison des énergies de dissociation au seuil obtenue des expériences en pièges et des expériences iPEPICO montre l'importance du déplacement cinétique en lien avec les différentes fenêtres temporelles de ces expériences. Dans la technique à temps de vol, cette fenêtre est limitée à ~100 µs ce qui amène à des énergies de seuil plus grandes que dans les expériences de pièges à ions qui permettent d'atteindre des temps plus longs. Il y a une complémentarité entre ces deux types d'expériences: les rapports de branchement entre les voies de dissociation sont mieux étudiés en pièges alors que les expériences iPEPICO permettent de déterminer des taux de dissociation.

Ce travail attire aussi l'attention sur l'importance de la structure des PAH par une étude sur deux isomères du dibenzopyrène. Le rapport de branchement entre les voies de dissociation de ces isomères a été étudié en détail en fonction de l’énergie du photon absorbé. Nous avons montré que l’isomère présentant une structure non-plane se fragmente à plus basse énergie que l’isomère plan en raison d’effets stériques. Ceci est confirmé par nos calculs de structures utilisant la DFT ainsi que par une exploration extensive des surfaces de potentiel grâce aux simulations MD. Ces simulations montrent que la structure non-plane favorise la déshydrogénation et amène la formation d’un cycle à 5 carbones. Nous avons calculé l’énergétique de chemins spécifiques de fragmentation avec la DFT et nous avons obtenu une vision statistique de ces chemins par une exploration extensive grâce aux simulations MD. Cette approche néanmoins surestime la perte de fragments carbonés et sous-estime la perte de H_2, ce qui suggère qu’une comparaison systématique avec des résultats expérimentaux doit être menée.

Un résultat majeur de notre étude sur les isomères du dibenzopyrène est la mise en évidence d’un nouveau chemin de formation de H_2 par photodissociation. Celui-ci est favorisé par la présence de régions de type « baies ». En effet, nos résultats expérimentaux et théoriques ne peuvent être conciliés à basse énergie que si la perte des deux hydrogènes implique H_2 plutôt que H+H, en supposant une distribution statistique de l’énergie interne. Ceci est renforcé par la comparaison avec le cas du cation coronène, un PAH contenant aussi 24 atomes de carbone mais de forme compacte et sans « baies ». Le rôle des PAH comme catalyseurs de la formation de H_2 a été le sujet de plusieurs études en lien avec le contexte astrophysique. Des études expérimentales menées sur des PAH compacts comme le pyrène et le coronène avaient conclu que la perte de H_2 est un canal minoritaire, du moins à basse énergie. D’autres mécanismes ont donc été proposés qui seraient plus favorables à la formation de H_2, tous impliquant l'adsorption d'au moins un H sur le PAH tel que le mécanisme d'Eley-Rideal. Cependant les derniers modèles astrophysiques qui ont inclus ce processus ont conclu que ce n'était pas un processus majoritaire (Andrews et al. 2016). Notre étude montre que la photodissociation peut redevenir un mécanisme attractif pour la production de H_2 dans les régions de photodissociation mais il faut étendre son étude à d'autres types de structures que celle compacte du coronène.

Une perspective proposée pour ce travail est de mener des études supplémentaires à la fois expérimentales et théoriques sur des molécules avec des régions de type « baies ». Deux exemples de telles molécules sont le naphtho[8,1,2-ghi]chrysène et le benzo[c]naphtho[8,1,2-ghi]chrysène, représentés dans la Figure II de l'Annexe. Le premier a la même formule chimique que le dibenzopyrène mais une géométrie très différente. Ce serait donc un candidat d'étude idéal pour comparer à nos résultats. Le deuxième a 4 atomes de carbone en plus mais une structure empêchée similaire à celle présentée dans ce manuscrit. Il serait donc intéressant d'étudier ces deux molécules avec les méthodes théorétiques et expérimentales présentées dans ce travail.

Finalement, les modèles astrophysiques prédisent que les PAH qui survivent dans les PDR sont de grande taille (50 atomes de carbone ou plus). Il est donc nécessaire de quantifier les effets de la taille sur les processus étudiés : ionisation et fragmentation. Les études expérimentales restent cruciales dans ce domaine car les simulations ne peuvent traiter correctement les états excités et doivent faire face à des temps de calcul qui deviennent prohibitifs.

ANNEX

Table 7-1: DFT (B3LYP/6-31 G(d,p)) calculated dissociation energies for the direct loss of hydrogen in the different positions. Calculated $\widehat{S}^2$ eigenvalues for the triplet spin-states are indicated in parenthesis. Spin contamination occurs if the values are far from 2.0 in the case of the triplet.

	ΔH(0K) AE⁺ [eV]		*ΔH(0K) AL⁺ [eV]*	
	Triplet	Singlet	Triplet	Singlet
$C_{24}H_{14}^{+}$- H_a	4.77 (2.02)	5.50	4.85 (2.02)	5.38
$C_{24}H_{14}^{+}$- H_b	4.75 (2.02)	-	4.79 (2.02)	5.43
$C_{24}H_{14}^{+}$- H_c	4.82 (2.03)	-	4.82 (2.03)	5.45
$C_{24}H_{14}^{+}$- H_d	4.89 (2.02)	-	4.89 (2.03)	5.48
$C_{24}H_{14}^{+}$- H_e	4.82 (2.04)	-	4.82 (2.03)	5.32
$C_{24}H_{14}^{+}$- H_f	4.67 (2.03)	5.38	4.58 (2.02)	3.43
$C_{24}H_{14}^{+}$- H_g	4.71 (2.03)	-	4.55 (2.03)	3.60
$C_{24}H_{14}^{+}$- H_h	4.85 (2.03)	-	4.86 (2.02)	5.43
$C_{24}H_{14}^{+}$- H_i	4.84 (2.03)	-	4.83 (2.03)	5.53
$C_{24}H_{14}^{+}$- H_j	4.73 (2.03)	-	4.74 (2.03)	5.40
$C_{24}H_{14}^{+}$- H_k	4.70 (2.04)	-	4.67 (2.03)	5.45
$C_{24}H_{14}^{+}$- H_l	4.88 (2.02)	-	4.85 (2.02)	5.34
$C_{24}H_{14}^{+}$- H_m	4.83 (2.04)	-	4.81 (2.03)	5.59
$C_{24}H_{14}^{+}$- H_n	4.82 (2.03)	5.59	4.82 (2.02)	5.44

Table 7-2: DFT (B3LYP/6-31 G(d,p)) calculated dissociation energy for two consecutive H losses for the AE$^+$ and AL$^+$ isomers. The spin states of the products are specified. Calculated $\widehat{S^2}$ eigenvalues are indicated in parenthesis. Spin contamination occurs if the values are far from 0.75 for doublet and 3.75 for quartet. Left table: The second dehydrogenation occurs after a first loss of H from H_f. Right table: Two H losses departing from the same ring in AE$^+$, where the first dehydrogenation is the loss of H_g.

	$\Delta H(0K)$ AE$^+$ [eV]		$\Delta H(0K)$ AL$^+$ [eV]
	Doublet	Quartet	Doublet
$C_{24}H_{14}^{+}$- H_f - H_a	-	9.44 (3.78)	8.37 (0.76)
$C_{24}H_{14}^{+}$- H_f - H_b	9.19 (1.68)	9.49 (3.78)	8.36 (0.75)
$C_{24}H_{14}^{+}$- H_f - H_c	9.54 (1.78)	9.38 (1.78)	8.32 (0.77)
$C_{24}H_{14}^{+}$- H_f - H_d	9.67 (1.78)	9.50 (1.78)	8.34 (0.76)
$C_{24}H_{14}^{+}$- H_f - H_e	9.70 (1.77)	9.53 (1.77)	8.34 (0.77)
$C_{24}H_{14}^{+}$- H_f - H_g	9.64 (1.78)	9.42 (3.79)	5.39 (0.77)
$C_{24}H_{14}^{+}$- H_f - H_h	9.66 (1.78)	9.49 (1.77)	8.34 (0.77)
$C_{24}H_{14}^{+}$- H_f - H_i	9.58 (1.65)	9.64 (3.79)	8.32 (0.77)
$C_{24}H_{14}^{+}$- H_f - H_j	9.53 (1.78)	9.70 (3.79)	8.28 (0.80)
$C_{24}H_{14}^{+}$- H_f - H_k	9.45 (1.78)	9.71 (3.80)	8.31 (0.76)
$C_{24}H_{14}^{+}$- H_f - H_l	9.64 (1.78)	9.50 (1.78)	8.34 (0.76)
$C_{24}H_{14}^{+}$- H_f - H_m	9.71 (1.76)	9.54 (3.80)	8.38 (0.76)
$C_{24}H_{14}^{+}$- H_f - H_n	9.68 (1.77)	9.49 (3.79)	8.34 (0.76)

	$\Delta H(0K)$ AE$^+$ [eV]	
	Doublet	Quartet
$C_{24}H_{14}^{+}$- H_g - H_h	8.55 (0.77)	9.92 (3.77)
$C_{24}H_{14}^{+}$- H_g - H_i	8.75 (0.77)	9.67 (3.79)
$C_{24}H_{14}^{+}$- H_g - H_j	9.52 (1.78)	9.52 (3.77)

Table 7-3: B3LYP/6-31G(d,p) doublet spin state minima and transition states (TS) computed on the potential energy surface related to the H_2 loss from AE^+. AC stands for anticlockwise and C for clockwise movement. Values (in eV) are given with respect to the reactant. Raw energy values are followed by ZPE in parenthesis. The dashes represent failed (unconverged) calculations.

AE^+	TS1	H-shifted	TS2	M^+ ---H_2	$[M^+$-$H_2] + H_2$
H_a- H_b (AC)	-	2.79 (-0.07)	-	5.52 (-0.44)	5.53 (-0.44)
H_a- H_b (C)	-	2.84 (-0.07)	-	5.45 (-0.41)	5.53 (-0.44)
H_b- H_c (AC)	3.54 (-0.17)	2.47 (-0.05)	5.69 (-0.33)	4.43 (-0.39)	4.43 (-0.41)
H_b- H_c (C)	3.68 (-0.17)	2.85 (-0.07)	5.69 (-0.33)	4.43 (-0.39)	4.43 (-0.41)
H_c- H_d (AC)	3.94 (-0.17)	2.98 (-0.07)	5.65 (-0.32)	4.66 (-0.39)	4.67 (-0.42)
H_c- H_d (C)	-	2.64 (-0.06)	-	4.66 (-0.39)	4.67 (-0.42)
H_d- H_e (AC)	4.01 (-0.15)	2.61 (-0.06)	5.65 (-0.33)	4.60 (-0.39)	4.61 (-0.42)
H_d- H_e (C)	3.68 (-0.17)	2.92 (-0.07)	5.44 (-0.30)	4.60 (-0.39)	4.61 (-0.42)
H_e- H_f (AC)	4.35 (-0.20)	2.16 (-0.03)	5.57 (-0.30)	6.04 (-0.44)	5.57 (-0.44)
H_e- H_f (C)	4.65 (-0.16)	2.50 (-0.05)	5.44 (-0.42)	5.56 (-0.42)	5.57(-0.44)
H_f- H_g (AC)	3.62 (-0.19)	2.81 (-0.07)	5.74 (-0.41)	5.50 (-0.41)	5.51 (-0.43)
H_f- H_g (C)	3.08 (-0.17)	2.06 (-0.04)	5.30 (-0.42)	5.30 (-0.40)	5.51 (-0.43)
H_g- H_h (AC)	3.75 (-0.19)	2.80 (-0.07)	5.22 (-0.42)	4.39 (-0.39)	4.40 (-0.41)
H_g- H_h (C)	3.86 (-0.18)	2.94 (-0.07)	5.76 (-0.33)	4.38 (-0.38)	4.40 (-0.41)
H_h- H_i (AC)	3.93 (-0.18)	2.92 (-0.07)	-	4.67 (-0.39)	4.68 (-0.42)
H_h- H_i (C)	3.93 (-0.18)	2.95 (-0.07)	-	4.67 (-0.39)	4.68 (-0.41)
H_i- H_j (AC)	3.85 (-0.18)	2.95 (-0.07)	-	4.42 (-0.39)	4.41 (-0.41)
H_i- H_j (C)	3.73 (-0.18)	2.78 (-0.06)	5.25 (-0.42)	4.42 (-0.39)	4.42 (-0.41)
H_j- H_k (AC)	-	2.29 (-0.05)	-	5.36 (-0.41)	5.52 (-0.44)
H_j- H_k (C)	-	2.85 (-0.08)	-	5.51 (-0.72)	5.52 (-0.44)

Table 7-4: B3LYP/6-31G(d,p) doublet spin state minima and transition states (TS) computed on the potential energy surface related to the H_2 loss from AE^+. AC stands for anticlockwise and C for clockwise movement. Values (in eV) are given with respect to the reactant. Raw energy values are followed by ZPE in parenthesis. The dashes represent failed (unconverged) calculations.

AL^+	TS1	H-shifted	TS2	M^+ ---H_2	$[M^+$-$H_2]$ + H_2
H_a- H_b (AC)	-	2.12 (-0.03)	5.72 (-0.37)	5.57 (-0.41)	5.57 (-0.43)
H_a- H_b (C)	-	2.87 (-0.05)	-	6.16 (-0.41)	5.57 (-0.43)
H_b- H_c (AC)	4.52 (-0.10)	2.59 (-0.05)	-	5.70 (-0.41)	5.71 (-0.43)
H_b- H_c (C)	-	2.09 (-0.03)	-	5.56 (-0.41)	5.64 (-0.43)
H_c- H_d (AC)	3.67 (-0.17)	2.91 (-0.07)	5.66 (-0.33)	4.59 (-0.39)	4.60 (-0.42)
H_c- H_d (C)	3.66 (-0.17)	2.55 (-0.05)	5.42 (-0.43)	4.59 (-0.38)	4.60 (-0.42)
H_d- H_e (AC)	3.97 (-0.18)	2.63 (-0.06)	-	4.66 (-0.40)	4.66 (-0.42)
H_d- H_e (C)	3.99 (-0.18)	2.98 (-0.07)	-	4.66 (-0.39)	4.66 (-0.42)
H_e- H_f (AC)	3.71 (-0.17)	2.90 (-0.06)	-	4.22 (-0.41)	4.23 (-0.42)
H_e- H_f (C)	3.38 (-0.19)	2.35 (-0.07)	5.30 (-0.35)	4.22 (-0.41)	4.23 (-0.42)
H_f- H_g (AC)	2.57 (-0.18)	2.48 (-0.08)	5.22 (-0.44)	1.15 (-0.31)	1.16 (-0.33)
H_f- H_g (C)	-	2.49 (-0.08)	-	1.15 (-0.31)	1.16 (-0.33)
H_g- H_h (AC)	3.53 (-0.19)	2.72 (-0.10)	5.35 (-0.35)	4.21 (-0.39)	4.22 (-0.42)
H_g- H_h (C)	-	2.88 (-0.06)	-	4.21 (-0.40)	4.22 (-0.42)
H_h- H_i (AC)	-	2.99 (-0.07)	-	4.65 (-0.39)	4.66 (-0.42)
H_h- H_i (C)	-	2.83 (-0.07)	-	4.65 (-0.45)	4.66 (-0.42)
H_i- H_j (AC)	3.82 (-0.18)	2.97 (-0.07)	-	4.40 (-0.39)	4.41 (-0.41)
H_i- H_j (C)	3.74 (-0.18)	2.69 (-0.06)	5.32 (-0.30)	4.40 (-0.38)	4.41 (-0.41)
H_j- H_k (AC)	-	2.31 (-0.05)	-	4.71 (-0.36)	4.72 (-0.38)
H_j- H_k (C)	-	2.88 (-0.07)	-	5.50 (-0.42)	5.51 (-0.44)

ANNEX II

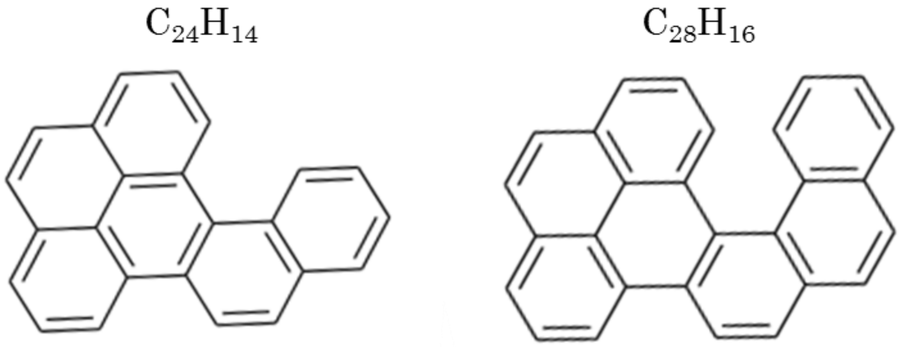

Figure II Naphtho[8,1,2-ghi]chrysene (left), with a similar formula as dibenzopyrene, and benzo[c]naphtho[8,1,2-ghi]chrysene (right), both presenting several bay areas.

List of Figures

Figure 1-1 Lifecycle of gas and dust in interstellar and circumstellar media. *Credit: M. Persson, NASA/ESA/ESO/ALMA* 7

Figure 1-2 Dust emission diagram obtained from an overlap of spectra from *ISO* and *COBE* satellites and *AROME* balloon experiment. Black lines correspond to the model output and black squares represent the photometric measurements from *COBE* after corrections. *Taken from* Compiègne et al. (2011). 9

Figure 1-3 Example of PAH molecules. From left to right and top to bottom: penanthrene ($C_{14}H_{10}$), chrysene ($C_{18}H_{12}$), triphenylene ($C_{18}H_{12}$), corannulene ($C_{20}H_{10}$), anthanthrene ($C_{22}H_{12}$), pentacene ($C_{22}H_{14}$), pentacene ($C_{22}H_{14}$), ovalene ($C_{32}H_{14}$), dicoronylene ($C_{48}H_{20}$), circumcoronene ($C_{54}H_{18}$). 10

Figure 1-4 Illustration of the PAH spectrum in the ISO-SWS spectra of planetary nebula NGC 4536, planetary nebula NGC 7027 and the PDR at the Orion bar. On the top axis the aromatic mode identifications of the major PAH bands are indicated. *Taken from* Peeters (2011)*)*. 12

Figure 1-5 Image of a reflection nebula called NGC 7023 NW depicting the young star on the bottom left (Fuente et al 1998). (b) Analysis of the spatial variation of the AIBs by Berné et al., 2007. Signals corresponding to ionized and neutral PAHs are depicted in blue and green respectively, while red corresponds to very small grains (VSGs). The contours are the IR emission at 8 µm showing the filamentary structure of this PDR (c) *Left:* Simplified blind signal separation spectra and their attribution to different carriers. *Right:* Analysis of the AIB emission in NGC 7023 along the Star-NW cut, using the PAHTAT tool (Pilleri et al. (2012); Montillaud et al. (2013)). 13

Figure 1-6 Jablonski diagram representing the relaxation mechanisms after UV absorption. Non radiative processes are presented in dotted lines: internal conversion (IC) and inter-system crossing (ISC), Radiative processes, such as infrared emission (IR), fluorescence or phosphorescence are presented in full lines. 17

Figure 1-7 Scheme of the possible evolution of a characteristic PAH (coronene, $C_{24}H_{12}^{+}$)) after the absorption of a UV photon, showcasing the main channels at play (ionization, photodissociation and relaxation). 18

Figure 2-1 Scheme of the synchrotron facility SOLEIL. 1) linear accelerator region, 2) booster, 3) storage ring with several beamlines depicted, 4) bending magnet, 5) RF cavities, 6) undolator. *Source*: *https://www.synchrotron-soleil.fr* 27

Figure 2-2 Design of the APPI setup. The photons coming from the UV lamp interact with the nebulized gas, ionizing it before it passes through the capillary to the instrument. *Source: https://www.agilent.com* 28

Figure 2-3 Schematic operation principle of a TOF. The sample target is irradiated by an ionization source, and the formed ions are subject to the applied electric field. They are accelerated before drifting into the free-field region, where the travel with a velocity proportional to their m/z ratio before being detected in the detector as a function of their arrival time. 30

Figure 2-4. Schematic design of a Penning trap (left). The right image shows the trapping of the cation in the center, due to the electric field produced between the (a) and (b) electrodes and the magnet field (B) produced by a toroidal electromagnet. *Figures by Arian Kriesch.* 32

Figure 2-5 Motion of a charged particle inside a Penning trap. It is the superposition of the axial, magnetron, and cyclotron motions. *Taken from Kluge (2013).* 33

Figure 2-6 Motion of the ions inside a FT-IRC. a) No electrical field applied. b) Motion of the ions with cyclotron frequencies in sync with the excitation field. *Adopted from Useli-Bacchitta (2010).* 34

Figure 2-7. Scheme of the PIRENEA setup, (Useli-Bacchitta (2010)). 35

Figure 2-8 Quadrupole electric field created by hyperbolic conductors. 36

Figure 2-9 Left: Scheme of a linear 4-rod geometry of a Paul trap. The oscillation is controlled by the DC (U) and RF (V) potentials applied to each pair of the rods (*taken* *from March & Todd (2005)*). Right: Scheme of the potential surface created in a Paul trap. a) At t=0 the particle is confined in the left-right direction. b) In the second half of the period the particle becomes confined in the perpendicular direction. 37

Figure 2-10 a) Stability regions in the X and Y axes of the LIT are indicated by the shaded areas. Roman numbers indicate the stability areas along the XY plane. *Taken from Du & Douglas (1999)*. b) Zoom on the most commonly used overlapping region near the origin of the quadrupole. Ions which fall into this region for a given set of trapping conditions will remain in the trap (*adapted from Paul (1990)).* 38

Figure 2-11 Schematic representation of the DESIRS beamline at SOLEIL. *Taken from https://www.synchrotron-soleil.fr/en/beamlines/desirs* 40

Figure 2-12 Scheme of DESIRS beamline *(Adapted from Milosavljevic et al. (2012)).* 41

Figure 2-13 Photograph of the LTQ ion trap setup at DESIRS/SOLEIL. The PAH solution is injected from the needle (bottom right) towards the APPI source. The shutter controller can be seen on top of the instrument. 42

Figure 2-14 VUV beamline layout at SLS (not to scale). BM: beam magnet, (Sv, Sh): vertical and horizontal slits, XB: X-ray blocker, M1: collimating mirror, G: grating, M2: refocusing mirror, M3: flip mirror, GF: gas filter, Se: exit slit, E1, E2: endstations 1 and 2. *Taken from Johnson et al. (2009).* 43

Figure 2-15 Scheme of iPEPICO setup, where the electrons are accelerated through the electron flight tube before being detected, and the ions are accelerated in the opposite direction and reach the TOF detector at a time t, measured. 45

Figure 2-16 Example of unimolecular breakdown diagram for pyrene radical cation ($C_{16}H_{10}^+$). The curves correspond to the parent and to the dehydrogenated daughter ions ($C_{16}H_9^+$ anc $C_{16}H_8^+$). *Figure taken from West et al. (2014c).* 46

Figure 3-1. An example of a PES. The initial products A and B will follow the least energetic paths, represented by red lines, to reach the final reactant point. Saddle points and transition structures are presented, where the local curvatures reach a maximum. *Image taken from (http://www.chem.wayne.edu/~hbs/chm6440/PES.html).* 56

Figure 4-1. Schematic geometries of the dibenzo(a,e)pyrene isomer cations studied in this thesis. The planar isomer, AE^+, is shown in (a) and the non-planarity of AL^+ can be seen in (b). 63

Figure 4-2 Example of a mass spectra obtained for AE^+ after the absorption of 15.5 eV photons. The green line represents the raw ion signal, the yellow line represents the background ion signal and the final corrected signal can be seen in the blue line. 65

Figure 4-3. Mass spectra obtained with the LTQ mass spectrometer for AE^+ and AL^+ under different VUV irradiation energies (8.3, 11.9 and 13.4 eV). The parent is labelled as $C_{24}H_{14}^+$. $C_{24}H_{13}^+$ and $C_{24}H_{12}^+$ correspond to the loss of H and 2H/H_2 fragments, respectively. $C_{24}H_{14}^{++}$ corresponds to the ionization of the parents leading to doubly ionized species. The vertical axis represents the intensities of the corrected signal and it has been scaled in each case to 1/5 of the parent peak value. 68

Figure 4-4 Values of the relative intensity of the photoproducts of AE^+ and AL^+ submitted to VUV photons as a function of photon energy (solid lines). The dotted lines are the computed photo-absorption cross sections calculated with the same method as in Malloci et al. (2004). Black lines correspond to AL^+ and grey lines correspond to AE^+. 70

Figure 4-5 Ionization (dashed) and fragmentation (full) related abundances of both isomers (grey for AE^+ and black for AL^+). 71

Figure 4-6 Abundances of the photofragments of AE^+ (a) and AL^+ (b) as a function of the VUV photon energy. The values are normalized to the total number of trapped ions and estimated error bars are also reported. Up to 4 hydrogen losses are observed: loss of H ($C_{24}H_{13}^+$) (blue), loss of 2 hydrogens ($C_{24}H_{12}^+$) (red), loss of 3 hydrogens ($C_{24}H_{11}^+$) (green) and loss of 4 hydrogens ($C_{24}H_{10}^+$) (yellow). 72

Figure 4-7 Zoom on the abundance of $C_{24}H_{13}^+$ formed by H loss as a function of the VUV photon energy. b) Similar for $C_{24}H_{12}^+$ resulting from 2H/H_2 loss. Circles correspond to AL^+ and squares to AE^+ parent cations. Error bars are included in the boxes. 74

Figure 4-8 Hydrocarbon losses for AE^+ (top) and AL^+ (bottom). Note the difference in the Yield scale. 75

Figure 5-1 Optimized geometries of AE^+ (left) and AL^+ (right) with the hydrogens labelled. 78

Figure 5-2. Front and side view of the optimized geometry of AL^+ after the removal of H_f. 81

Figure 5-3. Scheme illustrating the elementary steps computed for the loss of H_2 (two-step mechanism involving bay H). a) The arrows represent the clockwise (C) and anticlockwise (AC) migration. b) Configuration after clockwise H-migration (H_b migration to the carbon bearing H_a, leading to a sp^3 configuration). c) Final geometry with the loss of H_2. AE^+ was used as an example. 83

Figure 5-4. Elementary steps (B3LYP/6-31G(d,p)) of the more favorable path leading to the formation of H_2 from AE^+, involving the lowest energy TS. The relative energy values with respect to the reactant, given in eV, include the ZPE values. The imaginary frequencies of the TS are shown in italics and given in cm^{-1}. 84

Figure 5-5. Elementary steps (B3LYP/6-31G(d,p)) of the more favorable path leading to the formation of H_2 from AL^+. The lowest energy transition states involve the special hydrogens H_f and H_g. The relative energy values with respect to the reactant, given in eV, include the ZPE values. The imaginary frequencies of the TS are shown in italics and given in cm^{-1}. 85

Figure 5-6. Second H migration for AL^+ in the path towards H_2 loss. The energy required for this second migration (around 3.3 eV) is lower than the barrier of the reaction (4.80 eV). 86

Figure 6-1 TOF mass spectra at different photon energies for AL^+. 91

Figure 6-2 Kinetic shift due to the increase of degrees of freedom, as the size of the molecule increases. Parent ion decays are observed to occur at significant higher energies for the larger PAHs (West et al. (2018)). These decays have similar dissociation threshold values (*i.e.*, AL^+ is not included). The number in parenthesis corresponds to the number of carbon atoms in each molecule. 93

Figure 6-3 iPEPICO breakdown diagrams obtained for AE^+ with an extraction field of 120 V/cm. The points correspond to the experimental values and the lines represent the statistical fits obtained by RRKM modelling. 94

Figure 6-4 iPEPICO breakdown diagrams obtained for AL^+ with an extraction field of 120 V/cm. The points correspond to the experimental values and the lines represent the statistical fits obtained by RRKM modelling. 94

Figure 6-5 Comparison of the dissociation rates as a function of the internal energy for the loss of H from the parent cation $[M]^+$ – blue – and from the singly dehydrogenated cation $[M-H]^+$ – red. Full lines: $M=AE^+$; dotted lines: $M=AL^+$. These rates were obtained using RRKM theory and the activation parameters reported in Table 6-1. 96

Figure 6-6 MD/DFTB simulations: Dissociation of AE^+ and AL^+ with 26 eV (a,b), 28 eV (c,d) and 30 eV (e,f) of internal energy. Point-connecting lines are introduced for clarity. The parent ions are only depicted in (a) and (b) as an example. 101

Figure 6-7 Evolution of fragments as a function of the internal energy (26, 28, 30 eV) at 500 ps for both isomers from MD/DFTB simulations. Straight lines and square markers correspond to AE^+ while dashed lines and circles correspond to AL^+. 102

Figure 6-8 MD/DFTB simulations: Screenshot of the molecular geometry of AL^+ before the loss of H from a sp^3–C center after the formation of a 5 member ring at 26 eV of internal energy. 103

Figure 6-9 Two sequences leading to H_2 loss (top) and 2H loss (bottom) in AL^+ at 28 eV of internal energy from MD/DFTB simulations. The first step always involves the formation of a 5-member ring. For H_2 loss, the ring adjacent to this 5-member ring opens and closes before the H_2 loss. For the loss of 2H a hydrogen migration occurs inside the molecule before 2 losses of (adjacent) hydrogens. 103

Figure 6-10 MD/DFTB simulations: Example of two sequential H losses in AL^+ at 30 eV of internal energy. The first H atom leaves from a carbon bearing two hydrogens. Then the 5-member ring opens and another H from the CH_2 group is lost. 104

Figure 6-11 MD/DFTB simulations: Example of H loss in AE^+ at 30 eV of internal energy. Similarly to the case of AL^+ at lower energies in the hindered sites, we observe H migrations inside AE^+ at this high energy (dashed circle). The full circle corresponds to the actual loss of H. 104

Figure 6-12 Comparison of the dissociation rates as a function of the internal energy obtained through RRKM fitting of the iPEPICO experiments (lines) and MD calculations (squares) for the loss of H from the parent cation. Also added on the figure are the threshold energies measured in the SOLEIL experiments (dots) for such fragmentation pathway. The arrow points towards lower dissociation rates corresponding to the actual threshold of H loss from AL^+, which we missed. Full figures represent $[AE]^+$ and dotted figures represent $[AL]^+$. 108

Figure 7-1 Schematic drawings of the eight molecules of the ion trap campaign. From left to right and top to bottom: anthracene ($C_{14}H_{10}$), pyrene ($C_{16}H_{10}$), tetracene ($C_{18}H_{12}$), perylene ($C_{20}H_{12}$), benzoperylene ($C_{22}H_{12}$), coronene ($C_{24}H_{12}$), dibenzo(a,e)pyrene ($C_{24}H_{14}$), dibenzo(a,l)pyrene ($C_{24}H_{14}$). 113

Figure 7-2 Values of the relative intensity of the photo-products of different PAHs (full black lines) submitted to VUV photons as a function of photon energy. Theoretical cross sections calculated by Malloci et al. (2004), (2007a) are shown in grey dotted lines. 114

Figure 7-3 Photoionization yields of PAH cations as a function of incident photon energy in the 8-20 eV range, including error bars. 115

Figure 7-4 Comparison between the photo-ionization yield of coronene neutral (Verstraete et al. (1990)) and cation (this work, Figure 7-3). 116

Figure 7-5 Schematic figures of five of the molecules studied on the iPEPICO test campaign. The remaining five are shown in Figure 7-1. 117

Figure 7-6 Activation energy as a function of carbon number for the dehydrogenation reactions from naphthalene (C10) to coronene (C24). Outlines highlight the three trends observed. The distinctively low values obtained for the single loss of H from a sp^2 carbon of AL$^+$ are shown in the full circle.____________ 118

Figure 7-7 Trends for hydrocarbon fragment loss as a function of carbon number. Some results from previous work by the group of Prof. P. Mayer were included for completeness. ____________ 119

Figure 7-8 Abundances of the photo-dehydrogenation fragments of coronene cation ($C_{24}H_{12}^+$) as a function of the VUV photon energy. The values are normalized to the total number of trapped ions. Blue represents the loss of a single H atom ($C_{24}H_{11}^+$) and red represents the loss of 2H/H_2 ($C_{24}H_{10}^+$). Minor (< 0.2%) losses of 3 and 4 hydrogens observed in the experiment are not shown for clarity. ____________ 121

Bibliography

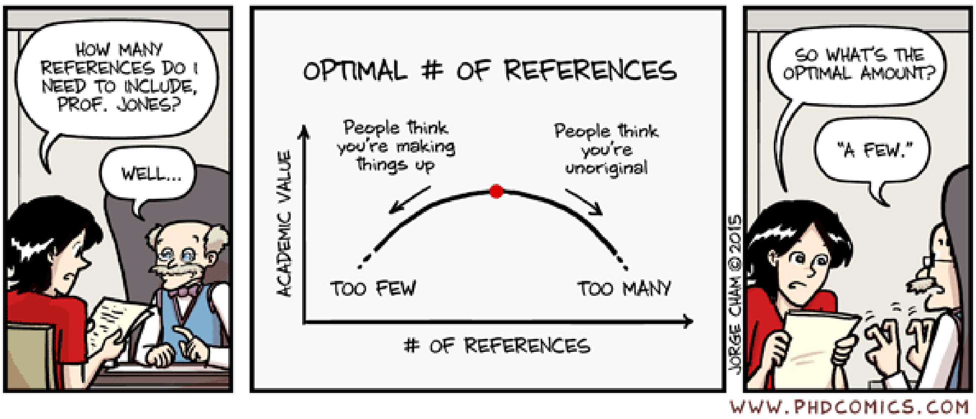
HOW MANY REFERENCES DO I NEED TO INCLUDE, PROF. JONES?
WELL...
OPTIMAL # OF REFERENCES
ACADEMIC VALUE
People think you're making things up
People think you're unoriginal
TOO FEW
TOO MANY
# OF REFERENCES
JORGE CHAM © 2015
SO WHAT'S THE OPTIMAL AMOUNT?
"A FEW."
WWW.PHDCOMICS.COM

Allain T, Leach S, Sedlmayr E (**1996**) "*Photodestruction of PAHs in the interstellar medium. I. Photodissociation rates for the loss of an acetylenic group.*" A&A, 305: pp 602–615

Allamandola LJ, Tielens AGGM, Barker JR (**1985**) "*Polycyclic aromatic hydrocarbons and the unidentified infrared emission bands - Auto exhaust along the Milky Way.*" ApJ, 290: pp L25–L28, doi: 10.1086/184435

Allamandola LJ, Tielens AGGM, Barker JR (**1989**) "*Interstellar polycyclic aromatic hydrocarbons: the infrared emission bands, the excitation/emission mechanism, and the astrophysical implications.*" ApJ Suppl Ser, 71: pp 733–775, doi: 10.1086/191396

Andrews H, Boersma C, Werner MW, et al. (**2015**) "*PAH emission at the bright locations of PDRs: The grandPAH hypothesis.*" ApJ, 807: pp 99, doi: 10.1088/0004-637x/807/1/99

Andrews H, Candian A, Tielens AGGM (**2016**) "*Hydrogenation and dehydrogenation of interstellar PAHs: Spectral characteristics and H2 formation.*" A&A, 23: pp 1–30, doi: 10.1051/0004-6361/201628819

Arlandini E, Franzoi L, Gioiat B, Sollazzo G (**1988**) "*Soft Ionization Techniques in Mass Spectrometry of Distamycin and Some Analogues.*" Bio Environm Mass Spectrom, 16: pp 419–422

Baer T, Mayer PM (**1997**) "*Statistical RRKM/QET calculations in mass spectrometry.*" J Am Soc Mass Spectrom, 8: pp 103–115

Bakes ELO, Tielens AGGM (**1994**) "*The photoelectric heating mechanism for very small graphitic grains and polycyclic aromatic hydrocarbons.*" ApJ, 427: pp 822, doi: 10.1086/174188

Bauschlicher CW, Bakes ELO (**2000**) "*Infrared spectra of polycyclic aromatic* *hydrocarbons (PAHs).*" Chem Phys, 262: pp 285–291, doi: 10.1016/s0301-0104(00)00310-4

Bauschlicher CW, Hudgins DM, Allamandola LJ (**1999**) "*The infrared spectra of polycyclic aromatic hydrocarbons containing a five-membered ring: symmetry breaking and the B3LYP functional.*" Theor Chem Acc, 103: pp 154–162, doi: 10.1007/s002149900033

Bauschlicher CW, Peeters E, Allamandola LJ (**2009**) "*The infrared spectra of very large irregular polycyclic aromatic hydrocarbons (PAHs): Observational probes of astronomical PAH geometry, size, and charge.*" ApJ, 697: pp 311–327, doi: 10.1088/0004-637x/697/1/311

Becke AD (**1993a**) "*A new mixing of Hartree-Fock and local density-functional theories.*" J Chem Phys, 98: pp 1372–1377, doi: 10.1063/1.464304

Becke AD (**1993b**) "*Density-functional thermochemistry. III. The role of exact exchange.*" J Chem Phys, 98: pp 5648–5652, doi: 10.1063/1.464913

Becke AD (**1996**) "*Density-functional thermochemistry. IV. A new dynamical correlation functional and implications for exact-exchange mixing.*" J Chem Phys, 104: pp 1040–1046, doi: 10.1063/1.470829

Bernard JP, Reach WT, Paradis D, et al. (**2008**) "*Spitzer survey of the large magellanic cloud, surveying the agents of a galaxy's evolution (sage). IV. dust properties in the interstellar medium.*" Astron J, 136: pp 919–945, doi: 10.1088/0004-6256/136/3/919

Berné O, Fuente A, Goicoechea JR, et al. (**2009**) "*Mid-infrared PAH and H2 emission as a probe of physical conditions in extreme PDRs.*" ApJ Lett, 706, doi: 10.1088/0004-637x/706/1/l160

Berné O, Joblin C, Deville Y, et al. (**2007**) "*Analysis of the emission of very small dust particles from Spitzer spectro-imagery data using blind signal separation methods.*" A&A, 469: pp 575–586, doi: 10.1051/0004-6361:20066282

Beyer T, Swinehart DF (**1973**) "*Algorithm 448: number of multiply-restricted partitions.*" Commun ACM, 16: pp 379, doi: 10.1145/362248.362275

Bodi A, Johnson M, Gerber T, et al. (**2009**) "*Imaging photoelectron photoion coincidence spectroscopy with velocity focusing electron optics.*" Rev Sci Instr, 80, doi: 10.1063/1.3082016

Boersma C, Bauschlicher CW, Ricca A, et al. (**2014**) "*The NASA Ames PAH IR Spectroscopic Database version 2.00: Content, web site, and on(off)line tools.*" ApJ Suppl Ser, 211, doi: 10.1088/0067-0049/211/1/8

Born M, Oppenheimer R (**1927**) "*Zur Quantentheorie der Molekeln.*" Ann Phys, 386: pp 457–484, doi: 10.1002/andp.19273892002

Boschman L, Cazaux S, Spaans M, et al. (**2015**) "*H2 formation on PAHs in photodissociation regions: a high-temperature pathway to molecular hydrogen.*" A&A, 579: pp 1–12, doi: 10.1051/0004-6361/201323165

Bréchignac P, Garcia GA, Falvo C, et al. (**2014**) "*Photoionization of cold gas phase coronene and its clusters: Autoionization resonances in monomer, dimer, and trimer and electronic structure of monomer cation.*" J Chem Phys, 141, doi: 10.1063/1.4900427

Buonomo F, Carraro G, Lia C (**2000**) "*Galaxy formation and evolution - II . Energy balance , star formation and feedback.*" Mon Not R Astron Soc, 312: pp 371–379

Calvo F, Basire M, Parneix P (**2011**) "*Temperature effects on the rovibrational spectra of pyrene-based PAHs.*" J Phys Chem A, 115: pp 8845–8854

Campbell EK, Holz M, Gerlich D, Maier JP (**2015**) "*Laboratory confirmation of C60+ as the carrier of two diffuse interstellar bands.*" Nature, 523: pp 322–323, doi: 10.1038/nature14566

Candian A, Sarre PJ, Tielens AGGM (**2014**) "*Polycylic Aromatic Hydrocarbons with armchair edges and the 12.7 μm band.*" ApJ Lett, 791: pp L10, doi: 10.1088/2041-8205/791/1/l10

Cazaux S, Boschman L, Rougeau N, et al. (**2016**) "*The sequence to hydrogenate coronene cations: A journey guided by magic numbers.*" Sci Reports, 6: pp 19835, doi: 10.1038/srep19835

Ceperley DM, Alder BJ (**1980**) "*Ground state of the electron gas by a stochastic model.*" Phys Rev Lett, 45: pp 566–569, doi: 10.1103/physrevlett.45.566

Cernicharo J, Heras AM, Tielens AGGM, et al. (**2001**) "*Infrared Space Observatory's Discovery of C4H2, C6H2, and Benzene in CRL 618.*" ApJ, 546: pp L123–L126, doi: 10.1086/318871

Cesarsky D, Lequeux J, Ryter C, Gérin M (**2000**) "*ISO observations of the reflection nebula Ced 201: evolution of carbonaceous dust.*" A&A Lett, 354: pp L87–L91

Chen T, Gatchell M, Stockett MH, et al. (**2015**) "*Formation of H2 from internally heated polycyclic aromatic hydrocarbons: Excitation energy dependence.*" J Chem Phys, 142: pp 1–8, doi: 10.1063/1.4917021

Cherchneff I, Barker JR, Tielens AGGM (**1992**) "*Polycyclic aromatic hydrocarbon formation in carbon-rich stellar envelopes.*" ApJ, 401: pp 269, doi: 10.1086/172059

Chupka WA (**1959**) "*Effect of unimolecular decay kinetics on the interpretation of appearance potentials.*" J Chem Phys, 30: pp 191–211, doi: 10.1063/1.1729875

Ciesla L, Boquien M, Boselli A, et al. (**2014**) "*Dust Spectral Energy Distributions of Nearby Galaxies: an Insight from the Herschel Reference Survey.*" A&A, 128: pp 1–33, doi: 10.1051/0004-6361/201323248

Compiègne M, Flagey N, Noriega-Crespo A, et al. (**2010**) "*Dust in the diffuse emission of the Galactic plane: The Herschel/Spitzer spectral energy distribution fitting.*" ApJ Lett, 724: pp 44–47, doi: 10.1088/2041-8205/724/1/l44

Compiègne M, Verstraete L, Jones AP, et al. (**2011**) "*The global dust SED: tracing the nature and evolution of dust with DustEM.*" A&A, 525: pp 103, doi: 10.1051/0004-6361/201015292

De Haas AJ, Oomens J, Bouwman J (**2016**) "*Facile pentagon formation in the dissociation of polyaromatics.*" Phys Chem Chem Phys, 19: pp 2974–2980, doi: 10.1039/c6cp08349h

de Hoffmann E, Stroobant V (**2007**) Mass Spectrometry - Principles and Applications, 3rd edn. John Wiley & Sons Ltd

DeFrees DJ, McLean AD (**1985**) "*Molecular orbital predictions of the vibrational frequencies of some molecular ions.*" J Chem Phys, 82: pp 333–341, doi: 10.1063/1.448805

Draine BT, Li A (**2007**) "*Infrared Emission from Interstellar Dust. IV. The Silicate-Graphite-PAH Model in the Post- Spitzer Era.*" ApJ, 657: pp 810–837, doi: 10.1086/511055

Du Z, Douglas DJ (**1999**) "*A novel tandem quadrupole mass analyzer.*" J Am Soc Mass Spectrom, 10: pp 1053–1066, doi: 10.1016/s1044-0305(99)00094-x

Ehrenfreund P, Charnley SB (**2000**) "*Organic Molecules in the Interstellar Medium, Comets, and Meteorites: A Voyage from Dark Clouds to the Early Earth.*" Annu Rev A&A, 38: pp 427–483, doi: 10.1146/annurev.astro.38.1.427

Ekern SP, Marshall AG, Szczepanski J, Vala M (**1998**) "*Photodissociation of gas-phase polycylic aromatic hydrocarbon cations.*" J Phys Chem A, 102: pp 3498–3504, doi: 10.1021/jp980488e

Elstner M, Porezag D, Jungnickel G, et al. (**1998**) "*Self-consistent-charge density-functional tight-binding method for simulations of complex* *materials properties.*" Phys Rev B, 58: pp 7260–7268, doi: 10.1103/physrevb.58.7260

Ferrière K (**2001**) "*The interstellar environment of our galaxy.*" Rev Mod Phys, 73: pp 1031–1066, doi: 10.1103/revmodphys.73.1031

Frenklach M, Feigelson ED (**1989**) "*Formation of polycyclic aromatic hydrocarbons in circumstellar envelopes.*" ApJ, 341: pp 372–384

Frisch MJ (**2013**) "*Gaussian 09, Revision D.01*"

Fuente A, Martín-Pintado J, Rodríguez-Fernández NJ, et al. (**1999**) "*Infrared space observatory observations toward the reflection nebula NGC 7023: A nonequilibrium ortho-to-para H2 ratio.*" ApJ, 518: pp 45–48

Galliano F (**2018**) "*A dust spectral energy distribution model with hierarchical Bayesian inference – I. Formalism and benchmarking.*" Mon Not R Astron Soc, 476: pp 1445–1469, doi: 10.1093/mnras/sty189

Galué HA, Oomens J (**2012**) "*On the electronic structure of isolated mono-dehydrogenated polyaromatic hydrocarbon ions and their astrophysical relevance.*" ApJ, 746: pp 83, doi: 10.1088/0004-637x/746/1/83

Galué HA, Oomens J (**2011**) "*Spectroscopic Evidence for a Triplet Ground State in the Naphthyl Cation **.*" Angew Chemie - Int Ed, 50: pp 7004–7007, doi: 10.1002/anie.201102333

Gatchell M, Stockett MH, De Ruette N, et al. (**2015**) "*Failure of hydrogenation in protecting polycyclic aromatic hydrocarbons from fragmentation.*" Phys Rev A, 92: pp 1–10, doi: 10.1103/physreva.92.050702

Gatchell M, Zettergren H (**2016**) "*Knockout driven reactions in complex molecules and their clusters.*" J Phys B, 49: pp 162001

Giuliani A, Giorgetta JL, Ricaud JP, et al. (**2012**) "*Atmospheric pressure photoionization using tunable VUV synchrotron radiation.*" Nucl Inst Methods Phys Res B, 279: pp 114–117, doi: 10.1016/j.nimb.2011.10.038

Green WH (**1992**) "*Transition states and rate constants for unimolecular reactions.*" Annu Rev Phys Chem, 43: pp 591–626

Guo X, Sievers HL, Grützmacher HF (**1999**) "*Hydrogen atom elimination from polycyclic aromatic hydrocarbons with sustained off-resonance irradiation: a new approach to produce carbon/hydrogen cluster cations CnHx+.*" Int J Mass Spectrom, 185: pp 1–10, doi: 10.1016/s1387-3806(98)14017-4

Habart E, Boulanger F, Verstraete L, et al. (**2004**) "*Some empirical estimates of the H(2) formation rate in photon-dominated regions.*" A&A, 414: pp 531–544, doi: 10.1051/0004-6361:20031659

Hall KF, Boggio-Pasqua M, Bearpark MJ, Robb MA (**2006**) “*Photostability via sloped conical intersections: A computational study of the excited states of the naphthalene radical cation.*” J Phys Chem A, 110: pp 13591–13599, doi: 10.1021/jp064711g

Hemberger P, Custodis VBF, Bodi A, et al. (**2017**) “*Understanding the mechanism of catalytic fast pyrolysis by unveiling reactive intermediates in heterogeneous catalysis.*” Nat Comm, 8: pp 15946, doi: 10.1038/ncomms15946

Hirama M, Tokosumi T, Ishida T, Aihara JI (**2004**) “*Possible molecular hydrogen formation mediated by the inner and outer carbon atoms of typical PAH cations.*” Chem Phys, 305: pp 307–316, doi: 10.1016/j.chemphys.2004.07.010

Hohenberg P, Kohn W (**1964**) “*Inhomogeneous electron gas.*” Phys Rev, 136: pp B864–B871, doi: 10.1103/physrev.136.b864

Hollenbach DJ, Tielens AGGM (**1999**) “*Photodissociation regions in the interstellar medium of galaxies.*” Rev Mod Phys, 71: pp 173–230, doi: 10.1103/revmodphys.71.173

Huang F-S, Dunbar RC (**1990**) “*Time-resolved Photodissociation of Methylnaphthalene ion. An illustration of kinetic shifts in large-ion dissociations.*” J Am Chem Soc, 112: pp 8167–8169

Joalland B, Rapacioli M, Simon A, et al. (**2010**) “*Molecular Dynamics simulations of anharmonic infrared spectra of [SiPAH]+ π -Complexes.*” J Phys Chem, 114: pp 5846–5854

Joblin C, D’Hendecourt L, Leger A, et al. (**1994**) “*Infrared spectroscopy of gas-phase PAH molecules. I: Role of the physical environment.*” A&A, 281: pp 923–936

Joblin C, Dontot L, Garcia GA, et al. (**2017**) “*Size Effect in the Ionization Energy of PAH Clusters.*” J Phys Chem Lett, 8: pp 3697–3702, doi: 10.1021/acs.jpclett.7b01546

Joblin C, Leger A, Martin P (**1992**) “*Contribution of polycyclic aromatic hydrocarbon molecules to the interstellar extinction curve.*” ApJ, 393: pp L79–L82, doi: 10.1086/186456

Joblin C, Mulas G (**2009**) “*Interstellar polycylic aromatic hydrocarbons: from space to the laboratory.*” EAS Publ Ser. doi: 10.1051/eas/0935008

Joblin C, Szczerba R, Berné O, Szyszka C (**2008**) “*Carriers of the mid-IR emission bands in PNe reanalysed. Evidence of a link between circumstellar and interstellar aromatic dust.*” A&A, 490: pp 189–196, doi: 10.1051/0004-6361:20079061

Joblin C, Tielens AGGM (**2011**) PAHs and the Universe : A Symposium to Celebrate the 25 th Anniversary of the PA. EAS Publications series

Joblin C, Tielens AGGM, Allamandola LJ, Geballe TR (**1996**) "*Spatial variation of the 3.29 and the 3.40 micron emission bands within reflection nebulae and the photochemical evolution of methylated polycylic aromatic hydrocarbons.*" ApJ, 458: pp 610–620

Jochims HW, Baumgartel H, Leach S (**1996**) "*Photoionisation Quantum Yields of Polycyclic Aromatic Hydrocarbons.*" A&A, 314: pp 1003–1009

Jochims HW, Baumgärtel H, Leach S (**1999**) "*Structure-dependent photostability of polycyclic aromatic hydrocarbon cations: Laboratory studies and astrophysical implications.*" ApJ, 512: pp 500–510

Jochims HW, Ruhl E, Baumgärtel H, et al. (**1994**) "*Size effects on dissociation rates of polycyclic aromatic hydrocarbon cations: Laboratory studies and astophysical implications.*" ApJ, 420: pp 307, doi: 10.1086/173560

Johnson M, Bodi A, Schulz L, Gerber T (**2009**) "*Vacuum ultraviolet beamline at the Swiss Light Source for chemical dynamics studies.*" Nucl Inst Methods Phys Res A, 610: pp 597–603, doi: 10.1016/j.nima.2009.08.069

Jolibois F, Klotz A, Gadéa FX, Joblin C (**2005**) "*Hydrogen dissociation of naphthalene cations: a theoretical study.*" A&A, 444: pp 629–634, doi: 10.1051/0004-6361:20053508

Jusko P, Simon A, Wenzel G, et al. (**2018**) "*Identification of the fragment of the 1-methylpyrene cation by mid-IR spectroscopy.*" Chem Phys Lett, 698: pp 206–210, doi: 10.1016/j.cplett.2018.03.028

Kassel LS (**1928**) "*Studies in Homogeneous Gas Reactions. I.*" J Phys Chem, 32: pp 225–242, doi: 10.1021/j150284a007

Kim S, Kwon E, Jeong KS, et al. (**2014**) "*Global spectral energy distributions of the Large Magellanic Cloud with interstellar dust.*" Astrophy Sp Sci, 349: pp 423–435, doi: 10.1007/s10509-013-1641-9

Kluge HJ (**2013**) "*Penning trap mass spectrometry of radionuclides.*" Int J Mass Spectrom ion Phys, 349–350: pp 26–37, doi: 10.1016/j.ijms.2013.04.017

Koch W, Holthausen MC (**2001**) A Chemist's Guide to Density Functional Theory, 2nd edn. Wiley-VCH Verlag GmbH & Co.

Koskinen P, Mäkinen V (**2009**) "*Density-functional tight-binding for beginners.*" Comput Mater Sci, 47: pp 237–253, doi: 10.1016/j.commatsci.2009.07.013

Langhoff SR (**1996**) "*Theoretical Infrared Spectra for Polycyclic Aromatic Hydrocarbon Neutrals, Cations, and Anions.*" J Phys Chem, 100: pp 2819–

2841, doi: 10.1021/jp952074g

Le Page V, Snow TP, Bierbaum VM (**2009**) "*Molecular hydrogen formation catalyzed by polycyclic aromatic hydrocarbons in the Interstellar Medium.*" ApJ, 704: pp 274–280, doi: 10.1088/0004-637x/704/1/274

Le Page V, Snow TP, Bierbaum VM (**2003**) "*Hydrogenation and charge states of PAHs in Diffuse Clouds. II. Results.*" ApJ, 584: pp 316–330, doi: \url{10.1086/345595}

Lee C, Yang W, Parr RG (**1988**) "*Development of the Colle-Salvetti correlation-energy formula into a functional of the electron density.*" Phys Rev B, 37: pp 785, doi: 10.1103/physrevb.37.785

Leger a., Puget JL (**1984**) "*Identification of the UIR emission Features of Interstellar Dust.*" A&A, 137: pp L5–L8

Léger A, Boissel P, D'Hendecourt L (**1988**) "*Predicted fluorescence mechanism in highly isolated molecules: The Poincaré fluorescence.*" Phys Rev Lett, 60: pp 921–924., doi: 10.1103/physrevlett.60.921

Lewars EG (**2011**) Computational Chemistry. Springer Dordrecht Heidelberg London New York

Lias SG, Levin RD, Kafafi SA (**2003**) "*National Institute of Standards and Technology.*" Gaithersburg, MD

Lifshitz C (**1997**) "*Energetics and dynamics through time-resolved measurements in mass spectrometry: Aromatic hydrocarbons, polycyclic aromatic hydrocarbons and fullerenes.*" Int Rev Phys Chem, 16: pp 113–139, doi: 10.1080/014423597230235

Lifshitz C (**1982**) "*Time-resolved appearance energies, breakdown graphs, and mass spectra: The elusive 'kinetic shift.'*" Mass Spectrom Rev, 1: pp 309–348, doi: 10.1002/mas.1280010402

Lindh R, Bernhardsson A, Schütz M (**1999**) "*Benzyne Thermochemistry: A Benchmark ab Initio Study.*" J Phys Chem A, 103: pp 9913–9920, doi: 10.1021/jp991919b

Ling Y, Gotkis I, Lifshitz C (**1995**) "*Time-dependent mass spectra and breakdown graphs. 18–Pyrene.*" Eur Mass Spectrom, 1: pp 41–49, doi: 10.1255/ejms.158

Ling Y, Lifshitz C (**1998**) "*Time-Dependent mass spectra and breakdown graphs. 21. C14H10 Isomers.*" J Phys Chem A, 102: pp 708–716, doi: 10.1021/jp973167w

Lodders K, Palme H, Gail H (**2009**) Abundances of the elements in the Solar

System, In Landolt. Berlin, Heidelberg, New York: Springer-Verlag,

Malloci G, Joblin C, Mulas G (**2007a**) "*On-line database of the spectral properties of polycyclic aromatic hydrocarbons.*" Chem Phys, 332: pp 353–359, doi: 10.1016/j.chemphys.2007.01.001

Malloci G, Joblin C, Mulas G (**2007b**) "*Theoretical evaluation of PAH dications properties.*" A&A, 635: pp 627–635, doi: 10.1051/0004-6361:20066053

Malloci G, Mulas G, Joblin C (**2004**) "*Electronic absorption spectra of PAHs up to vacuum UV Towards a detailed model of interstellar PAH photophysics.*" A&A, 426: pp 105–117, doi: 10.1051/0004-6361

Malrieu JP, Trinquier G (**2012**) "*A recipe for geometry optimization of diradicalar singlet states from broken-symmetry calculations.*" J Phys Chem A, 116: pp 8226–8237, doi: 10.1021/jp303825x

March RE (**1997**) "*An introduction to Quadrupole Ion Trap Mass Spectrometry.*" J Mass Spectrom, 32: pp 351–369, doi: 10.1002/(sici)1096-9888(199704)32:4<351::aid-jms512>3.0.co;2-y

March RE, Todd JFJ (**2005**) Quadrupole Ion Trap Mass Spectrometry, 2nd edn. John Wiley & sons, Inc.

Marciniak A, Despré V, Barillot T, et al. (**2015**) "*XUV excitation followed by ultrafast non-adiabatic relaxation in PAH molecules as a femto-astrochemistry experiment.*" Nat Comm, 6: pp 7909, doi: 10.1038/ncomms8909

Marcus RA (**1952**) "*Unimolecular dissociations and free radical recombination reactions.*" J Chem, 20: pp 359–364, doi: 10.1063/1.1700424

Marshall AG, Hendrickson CL, Jackson GS (**1998**) "*Fourier transform ion cyclotron resonance mass spectrometry: a primer.*" Mass Spectrom Rev, 17: pp 1–35

Mayer PM, Poon C (**2009**) "*The mechanisms of collisional activation of ions in mass spectrometry.*" Mass Spectrom Rev, 28: pp 608–639, doi: 10.1002/mas.20225

Mcguire BA, Burkhardt AM, Kalenskii S, et al. (**2018**) "*Detection of the aromatic molecule benzonitrile (c-C6H5CN) in the interstellar medium Brett.*" Science (80-), 359: pp 202–205, doi: 10.1126/science.aao4890

Merino P, Svec M, Martinez JI, et al. (**2014**) "*Graphene etching on SiC grains as a path to interstellar polycyclic aromatic hydrocarbons formation.*" Nat Comm, 5: pp 1–9, doi: 10.1038/ncomms4054

Milosavljevic AR, Nicolas C, Gil JF, et al. (**2012**) "*VUV synchrotron radiation: A* *new activation technique for tandem mass spectrometry.*" J Synch Rad, 19: pp 174–178, doi: 10.1107/s0909049512001057

Montillaud J, Joblin C, Toublanc D (**2013**) "*Evolution of polycyclic aromatic hydrocarbons in photodissociation regions. Hydrogenation and charge states.*" A&A, 552: pp 15, doi: 10.1051/0004-6361/201220757;

Mulas G, Malloci G, Joblin C, Toublanc D (**2006**) "*A general model for the identification of specific PAHs in the far-IR.*" A&A, 460: pp 93–104, doi: 10.1051/0004-6361:20054276

Mulliken RS (**1955**) "*Electronic population analysis on LCAO-MO molecular wave functions. I.*" J Chem Phys, 23: pp 1833–1840, doi: 10.1063/1.1740588

Nahon L, De Oliveira N, Garcia GA, et al. (**2012**) "*DESIRS: A state-of-the-art VUV beamline featuring high resolution and variable polarization for spectroscopy and dichroism at SOLEIL.*" J Synch Rad, 19: pp 508–520, doi: 10.1107/s0909049512010588

Oliveira AF, Seifert G, Heine T, Duarte HA (**2009**) "*Density-functional based tight-binding: An approximate DFT method.*" J Braz Chem Soc, 20: pp 1193–1205, doi: 10.1590/s0103-50532009000700002

Omont A (**1986**) "*Physics and chemistry of interstellar polycyclic aromatic molecules.*" A&A, 164: pp 159–178

Oomens J, Sartakov BG, Meijer G, von Helden G (**2006**) "*Gas-phase infrared multiple photon dissociation spectroscopy of mass-selected molecular ions.*" Int J Mass Spectrom, 254: pp 1–19, doi: 10.1016/j.ijms.2006.05.009

Oref I, Rabinovitch BS (**1979**) "*Do Highly Excited Reactive Polyatomic Molecules Behave Ergodically.*" Acc Chem Res, 12: pp 166–175, doi: 10.1021/ar50137a002

Osborn DL, Hayden CC, Hemberger P, et al. (**2016**) "*Breaking through the false coincidence barrier in electron-ion coincidence experiments.*" J Chem Phys, 145, doi: 10.1063/1.4965428

Paris C, Alcamí M, Martín F, Díaz-Tendero S (**2014**) "*Multiple ionization and hydrogen loss from neutral and positively-charged coronene.*" J Chem Phys, 140, doi: 10.1063/1.4875805

Parneix P, Gamboa A, Falvo C, et al. (**2017**) "*Dehydrogenation effects on the stability of aromatic units in polycyclic aromatic hydrocarbons in the interstellar medium: A computational study at finite temperature.*" Mol Astroph, 7: pp 9–18, doi: 10.1016/j.molap.2017.05.001

Paul W (**1990**) "*Electromagnetic traps for charged and neutral particles.*" Rev

Mod Phys, 62: pp 531–540, doi: 10.1103/revmodphys.62.531

Pauzat F, Talbi D, Ellinger Y (**1997**) "*The PAH hypothesis: a computational experiment on combined effects of ionization and dehydrogentaion on the IR signatures.*" A&A, 319: pp 318–330

Pauzat F, Talbi D, Miller MD, et al. (**1992**) "*Theoretical IR spectra of ionized naphthalene.*" J Phys Chem, 96: pp 7882–7889, doi: 10.1021/j100199a011

Peeters E (**2011**) "*Astronomical observations of the PAH emission bands.*" EAS Publ Ser, 46: pp 13–27, doi: 10.1051/eas/1146002

Peeters E, Hony S, Van Kerckhoven C, et al. (**2002**) "*The rich 6 to 9 um spectrum of interstellar PAHs.*" A&A, 390: pp 1089–1113, doi: 10.1051/0004-6361:20020773

Perdew JP (**1991**) "*Generalized gradient approximations for exchange and correlation: A look backward and forward.*" Phys B Phys Condens Matter, 172: pp 1–6, doi: 10.1016/0921-4526(91)90409-8

Perdew JP, Burke K, Ernzerhof M (**1998**) "*Perdew, Burke, and Ernzerhof Reply.*" Phys Rev Lett, 80: pp 891, doi: 10.1103/physrevlett.80.891

Perdew JP, Burke K, Ernzerhof M (**1996**) "*Generalized gradient approximation made simple.*" Phys Rev Lett, 77: pp 3865–3868, doi: 10.1103/physrevlett.77.3865

Perdew JP, Zunger A (**1981**) "*Self-interaction correction to density-functional approximations for many-electron systems.*" Phys Rev B, 23: pp 5048–5079, doi: 10.1103/physrevb.23.5048

Pilleri P, Montillaud J, Berné O, Joblin C (**2012**) "*Evaporating very small grains as tracers of the UV radiation field in photo-dissociation regions.*" A&A, 542: pp A69, doi: 10.1051/0004-6361/201015915

Pino T, Dartois E, Cao A-T, et al. (**2008**) "*The 6.2 um band position in laboratory and astrophysical spectra: a tracer of the aliphatic to aromatic evolution of interstellar carbonaceous dust.*" A&A, 490: pp 665–672, doi: 10.1051/0004-6361:200809927

Porezag D, Frauenheim T, Köhler T (**1995**) "*Construction of thigh-binding-like potentials o the basis of density-funtional theory: Application to carbon.*" Phys Rev B, 51: pp 947–957

Postma J, Bari S, Hoekstra R, et al. (**2009**) "*Ionization and fragmentation of anthracene upon interaction with keV protons and a particles.*" ApJ, 708: pp 435–444, doi: 10.1088/0004-637x/708/1/435

Rapacioli M, Joblin C, Boissel P, et al. (**2005**) "*Spectroscopy of Polycyclic*

Aromatic Hydrocarbons and very small grains in photodissociation regions." Eur Sp Agency, (Special Publ ESA SP, 204: pp 409–410, doi: 10.1051/0004-6361:20041247

Rapacioli M, Simon A, Dontot L, Spiegelman F (**2012**) "*Extensions of DFTB to investigate molecular complexes and clusters.*" Phys Status Solidi (B), 249: pp 245–258, doi: 10.1002/pssb.201100615

Rauls E, Hornekær L (**2008**) "*Catalyzed Routes to Molecular hydrogen formation and hydrogen addition reactions on neutral polycyclic aromatic hydrocarbons under Interstellar conditions.*" ApJ, 679: pp 531–536, doi: 10.1086/587614

Reitsma G, Boschman L, Deuzeman MJ, et al. (**2014**) "*Deexcitation dynamics of superhydrogenated polycyclic aromatic hydrocarbon cations after soft-x-ray absorption.*" Phys Rev Lett, 113: pp 1–5, doi: 10.1103/physrevlett.113.053002

Ricca A, Bauschlicher CW, Boersma C, et al. (**2012**) "*The infrared spectroscopy of compact polycyclic aromatic hydrocarbons containing up to 384 carbons.*" ApJ, 754, doi: 10.1088/0004-637x/754/1/75

Rice OK, Ramsperger HC (**1927**) "*Theories of unimolecular gas reactions at low pressures.*" J Am Chem Soc, 49: pp 1618, doi: 10.1021/ja01390a002

Rice OK, Ramsperger HC (**1928**) "*Theories of unimolecular gas reactions at low pressures II.*" J Am Chem Soc, 50: pp 618

Rodriguez Castillo S, Simon A, Joblin C (**2018**) "*Investigating the importance of edge-structure in the loss of H/H2of PAH cations: The case of dibenzopyrene isomers.*" Int J Mass Spectrom, 429: pp 189–197, doi: 10.1016/j.ijms.2017.09.013

Rosenberg MJF, Berné O, Boersma C (**2014**) "*Random mixtures of polycyclic aromatic hydrocarbon spectra match interstellar infrared emission.*" A&A, 566: pp L4, doi: 10.1051/0004-6361/201423953

Rouillé G, Krasutski SA, Fulvio D, et al. (**2015**) "*Dissociative photoionization of polycyclic aromatic hydrocarbon molecules carrying an ethynyl group.*" ApJ, 810: pp 114–123, doi: 10.1088/0004-637x/810/2/114

Salama F, Joblin C, Allamandola LJ (**1994**) "*Electronic absorption spectroscopy of matrix-isolated polycyclic aromatic hydrocarbon cations. II. The phenanthrene cation (C14H10+) and its 1-methyl derivative.*" J Chem Phys, 101: pp 10252, doi: 10.1063/1.467905

Salama F, Joblin C, Allamandola LJ (**1995**) "*Neutral and ionized PAHs: contribution to the interstellar extinction.*" Planet Space Sci, 43: pp 1165–

1173, doi: 10.1016/0032-0633(95)00051-6

Seifert G, Porezag D, Frauenheim T (**1996**) "*Calculations of molecules, clusters, and solids with a simplified LCAO-DFT-LDA scheme.*" Int J Quantum Chem, 58: pp 185–192

Sellgren K (**1984**) "*The near-infrared continuum emission of visual refelction nebulae.*" ApJ, 277: pp 623–633, doi: 10.1086/161733

Siebenmorgen R, Voshchinnikov N V, Bagnulo S (**2014**) "*Dust in the diffuse interstellar medium Extinction, emission, linear and circular polarisation.*" A&A, 561: pp A82, doi: 10.1051/0004-6361/201321716

Simon A, Champeaux JP, Rapacioli M, et al. (**2018**) "*Dissociation of polycyclic aromatic hydrocarbons at high energy : MD / DFTB simulations vs collision.*" Press

Simon A, Joblin C (**2009**) "*Photodissociation of [Fe_x (C24H12)_y]+ complexes in the PIRENEA setup: Iron-polycyclic aromatic hydrocarbon clusters as candidates for very small interstellar grains.*" J Phys Chem A, 113: pp 4878–4888, doi: 10.1021/jp8099785

Simon A, Rapacioli M (**2018**) "*Energetic processing of PAHs: isomerisation and dissociation.*" In: Chemical Modelling: Volume 14. The Royal Society of Chemistry, pp 195–216

Simon A, Rapacioli M, Lanza M, et al. (**2011**) "*Molecular dynamics simulations on [FePAH]+ π-complexes of astrophysical interest: anharmonic infrared spectroscopy.*" Phys Chem Chem Phys, 13: pp 3359, doi: 10.1039/c0cp00990c

Simon A, Rapacioli M, Rouaut G, et al. (**2017**) "*Dissociation of polycyclic aromatic hydrocarbons: molecular dynamics studies.*" Phil Trans R Soc A, pp 20160195, doi: 10.1098/rsta.2016.0195

Sloan GC, Jura M, Duley WW, et al. (**2007**) "*The unusual hydrocarbon emission from the early carbon star HD 100764: The connection between aromatics and aliphatics.*" ApJ, 664: pp 1144–1153, doi: 10.1086/519236

Sloan GC, Lagadec E, Zijlstra AA, et al. (**2014**) "*Carbon-rich dust past the Asymptotic Giant Branch: Aliphatics, aromatics, and fullerenes in the Magellanic Clouds.*" ApJ, 791: pp 28, doi: 10.1088/0004-637x/791/1/28

Solano EA, Mayer PM (**2015**) "*A complete map of the ion chemistry of the naphthalene radical cation? DFT and RRKM modeling of a complex potential energy surface.*" J Chem Phys, 143, doi: 10.1063/1.4930000

Szabo A, Ostlund NS (**1982**) "*Modern Quantum Chemistry: Introduction to Advanced Electronic Structure Theory.*" Introd. to Adv. Electron. Struct.

Theory

Szczepanski J, Oomens J, Steill JD, Vala M (**2011**) "*H2 ejection from polycyclic aromatic hydrocarbons: Infrared multiphoton dissociation study of protonated acenaphthene and 9,10-dihydrophenanthrene.*" ApJ, 727: pp 12, doi: 10.1088/0004-637x/727/1/12

Szczepanski J, Vala M (**1993**) "*Laboratory evidence for ionized polycyclic aromatic hydrocarbons in the interstellar medium.*" Lett to Nat, 363: pp 699, doi: 10.1038/363699a0

Sztáray B, Baer T (**2003**) "*Suppression of hot electrons in threshold photoelectron photoion coincidence spectroscopy using velocity focusing optics.*" Rev Sci Instr, 74: pp 3763–3768, doi: 10.1063/1.1593788

Sztáray B, Bodi A, Baer T (**2010**) "*Modeling unimolecular reactions in photoelectron photoion coincidence experiments.*" J Mass Spectrom, 45: pp 1233–1245, doi: 10.1002/jms.1813

Tan X, Salama F (**2005**) "*Cavity ring-down spectroscopy and vibronic activity of benzo[ghi]perylene.*" J Chem Phys, 123: pp 1–7, doi: 10.1063/1.1938907

Tan X, Salama F (**2006**) "*Cavity ring-down spectroscopy of jet-cooled 1-pyrenecarboxyaldehyde (C17H10O) and 1-methylpyrene (C17H12) cations.*" Chem Phys, 422: pp 518–521, doi: 10.1016/j.cplett.2006.03.006

Thrower JD, Nilsson L, Jørgensen B, et al. (**2011**) "*Superhydrogenated PAHs: catalytic formation of H2.*" EAS Publ Ser, 46: pp 453–460, doi: 10.1051/eas/1146047

Tielens AGGM (**2008**) "*Interstellar Polycyclic Aromatic Hydrocarbon Molecules*.*" Annu Rev A&A, 46: pp 289–337, doi: 10.1146/annurev.astro.46.060407.145211

Trinquier G, Malrieu JP (**2015**) "*Kekule versus lewis: When aromaticity prevents electron pairing and imposes polyradical character.*" Chem - A Eur J, 21: pp 814–828, doi: 10.1002/chem.201403952

Trinquier G, Simon A, Rapacioli M, Gadéa FX (**2017a**) "*PAH chemistry at eV internal energies. 1. H-shifted isomers.*" Mol Astroph, 7: pp 27–36, doi: 10.1016/j.molap.2017.02.001

Trinquier G, Simon A, Rapacioli M, Gadéa FX (**2017b**) "*PAH chemistry at eV internal energies. 2. Ring alteration and dissociation.*" Mol Astroph, 7: pp 37–59, doi: 10.1016/j.molap.2017.02.002

Useli-Bacchitta F (**2010**) "*Photophysique des molécules polycycliques aromatiques hydrogénées d ' intérêt interstellaire avec l ' expérience*

PIRENEA"

Useli-Bacchitta F, Bonnamy A, Mulas G, et al. (**2010**) "*Visible photodissociation spectroscopy of PAH cations and derivatives in the PIRENEA experiment.*" Chem Phys, 371: pp 16–23, doi: 10.1016/j.chemphys.2010.03.012

Uzer T, Miller WH (**1991**) "*Theories of intramolecular vibrational energy transfer.*" Phys Rep, 199: pp 73–146, doi: 10.1016/0370-1573(91)90140-h

van Diedenhoven B, Peeters E, Van Kerckhoven C, et al. (**2004**) "*The Profiles of the 3-12 micron Polycyclic Aromatic Hydrocarbon Features.*" ApJ, 611: pp 928–939, doi: 10.1086/422404

Verstraete L, Leger A, D'Hendecourt L, et al. (**1990**) "*Ionization cross-section measurements for two PAH molecules - Implications for the heating of diffuse interstellar gas.*" A&A, 237: pp 436–444

Wakelam V, Bron E, Cazaux S, et al. (**2017**) "*H2 formation on interstellar dust grains: the viewpoints of theory, experiments, models and observations.*" Mol Astroph, 9: pp 1–36, doi: 10.1016/j.molap.2017.11.001

Weingartner JC, Draine BT (**2001**) "*Photoelectric Emission from Interstellar Dust: Grain Charging and Gas Heating.*" ApJ Suppl Ser, 134: pp 263–281, doi: 10.1086/320852

West B, Joblin C, Blanchet V, et al. (**2012**) "*On the dissociation of the naphthalene radical cation: New iPEPICO and tandem mass spectrometry results.*" J Phys Chem A, 116: pp 10999–11007, doi: 10.1021/jp3091705

West B, Joblin C, Blanchet V, et al. (**2014a**) "*Dynamics of hydrogen and methyl radical loss from ionized dihydro-polycyclic aromatic hydrocarbons: A tandem mass spectrometry and imaging photoelectron-photoion coincidence (iPEPICO) study of dihydronaphthalene and dihydrophenanthrene.*" J Phys Chem A, 118: pp 1807–1816, doi: 10.1021/jp500430g

West B, Rodriguez Castillo S, Sit A, et al. (**2018**) "*Unimolecular reaction energies for polycyclic aromatic hydrocarbon ions.*" Phys Chem Chem Phys, 20: pp 7195, doi: 10.1039/c7cp07369k

West B, Sit A, Mohamed S, et al. (**2014b**) "*Dissociation of the anthracene radical cation: A comparative look at iPEPICO and collision-induced dissociation mass spectrometry results.*" J Phys Chem A, 118: pp 9870–9878, doi: 10.1021/jp505438f

West B, Useli-Bacchitta F, Sabbah H, et al. (**2014c**) "*Photodissociation of pyrene cations: Structure and energetics from C16H10+ to C14+ and almost everything in between.*" J Phys Chem A, 118: pp 7824–7831, doi: 10.1021/jp506420u

Wolf M, Kiefer H V., Langeland J, et al. (**2016**) “*Photo-stability of super-hydrogenated PAHs determined by action spectroscopy experiments.*” ApJ, 832: pp 24, doi: 10.3847/0004-637x/832/1/24

Yamaguchi Y, Gaw J, Schaefer HF, Binkley JS (**1986**) “*Analytic computation and basis set dependence of Intensities of Infrared Spectra.*” J Chem Phys, 84: pp 2262–2278, doi: 10.1063/1.450389

Zhen J, Castellanos P, Linnartz H, Tielens AGGM (**2016a**) “*Photo-fragmentation behavior of methyl- and methoxy-substituted derivatives of hexa-peri-hexabenzocoronene (HBC) cations.*” Mol Astrophys, 5: pp 1–8, doi: 10.1016/j.molap.2016.08.001

Zhen J, Castellanos P, Paardekooper DM, et al. (**2015**) “*Laboratory photo-chemistry of PAHS: Ionization vs Fragmentation.*” ApJ Lett, 804: pp 1–13, doi: 10.1088/2041-8205/804/1/l7.laboratory

Zhen J, Castellanos P, Paardekooper DM, et al. (**2014**) “*Laboratory Formation of Fullerenes From Pahs: Top-Down Interstellar Chemistry.*” ApJ, 797: pp L30, doi: 10.1088/2041-8205/797/2/l30

Zhen J, Rodriguez Castillo S, Joblin C, et al. (**2016b**) “*VUV photo-processing of PAH cations: Quantitative study on the ionization versus fragmentation processes.*” ApJ, 822: pp 113, doi: 10.3847/0004-637x/822/2/113

Zubko V, Dwek E, Arendt RG (**2004**) “*Interstellar Dust Models Consistent with Extinction, Emission, and Abundance Constraints.*” ApJ Suppl Ser, 152: pp 211, doi: 10.1086/382351